upna

Universidad Pública de Navarra
Nafarroako Unibertsitate Publikoa

THESIS FOR THE DEGREE OF DOCTOR OF PHILOSOPHY

Design of Antennas Based on Metasurfaces at Millimeters and Terahertz Waves

Dayan Pérez Quintana

Director: Miguel Beruete Díaz

Director: Iñigo Ederra Urzainqui

Grupo de Antenas

Departamento Ingeniería Eléctrica, Electrónica y de Comunicación

Universidad Pública de Navarra

Pamplona, España, 2022

Agradecimientos

A lo largo de estos 4 años vividos en Pamplona, son muchas las personas a las que agradecer, no solo por ayudarme en la investigación, sino también por hacerme sentir parte de esta gran familia que es el Grupo de Antenas de la Universidad Pública de Navarra.

Me gustaría empezar por mis compañeros del día a día, esos que están detrás de cada "buenos días" al empezar la jornada (a los que están y a los que siguen estando en la distancia). Muchas gracias a: Carlos Lezaun, Diego, Chocarro, Moshen, Ángel, Cristina, David, Kike, Douglas, Carlos Quemada, María, Iñigo Liberal, Jose, Alicia, Unai, Juanjo, Irati, Carlos Biurrun, Alexia y Osmery. De verdad, muchas gracias por estar ahí en las malas y en las buenas (que no fueron pocas), gracias de corazón. Agradezco también a todos esos amigos en la distancia, las personas que me ayudaron en mi estancia, a los que estuvieron virtualmente y a todos los que me puedo dejar sin mencionar, ya que han sido 4 años muy intensos de mucho trabajo.

De manera muy especial quiero agradecer a mis supervisores, Iñigo y Miguel, por guiarme, ayudarme y confiar en mi en todo momento. Gracias por darme la oportunidad de crecer profesionalmente e incluirme en esta gran familia a la que hoy pertenezco junto a vosotros. Gracias sobre todo por alimentar en mí este sentimiento de amor a la investigación que ha hecho plantearme continuar este camino, por duro que parezca.

En mi mundo más particular quiero agradecer a Yoana, mi prometida y a toda su familia. Estos 4 años no solo me hicieron investigar, sino también conocer el amor y ser correspondido. Gracias por apoyarme, aguantarme y entenderme en todos los buenos y los malos momentos (que no fueron pocos), esta tesis ha salido adelante en gran medida por ti, por tu cariño y amor, muchas gracias. Espero seguir cosechando éxitos y levantándome de fracasos siempre a tu lado.

Por último y no menos importante quiero agradecer a toda mi familia, a los que están y a los que por cosa del destino han tenido que partir, pero sé que están conmigo orgullosos de lo que he logrado hasta ahora. Gracias a mis abuelas, tías, mi tío y mis

primos, muy en especial a mi hermano Robe, porque ni la distancia a podido romper todo el cariño y el amor que nos tenemos. A mi hermana, por estar siempre, quererme, apoyarme y ser esa parte de mi que está al lado de nuestros padres mientras yo estoy a la distancia, no podré nunca agradecer todo lo que has hecho por mí estos años. En especial a mis padres, ustedes que me educaron e inculcaron los valores que hoy me forman, son los principales responsables de que haya llegado hasta aquí. Gracias por creer en mi siempre, por animarme y aconsejarme, por iluminar mi camino con su sabiduría, estoy muy orgulloso de ser su hijo.

En fin, gracias a todos los que han contribuido a que esta tesis de doctorado haya sido posible, cada una de mis vivencias, errores y aciertos estos 4 años con ustedes han influido directa o indirectamente en el trabajo que aquí presento. De corazón, muchas gracias.

A mis padres,
a mi familia y a ti.

Abstract

This thesis presents the evolution of an investigation line guided by the development of metallic structures to improve the radiation properties of devices operating at millimeter wave (mmWaves).

It covers different aspects of high frequency solutions such as Gap Waveguide (GW) technology to guide waves with low loss and high efficiency overcoming the limitations of classical waveguides. Using GW as a common link, three different antennas have been developed to generate circular polarization (CP) in a simple and compact way using a feeding technique based on the length difference of orthogonal arms exciting a slot on the top plate. Each of these antennas follows a natural evolution from the initial design that presents the basic operation fundamentals towards more complicated topologies aiming to increase the directivity.

Metasurfaces (MTS) are another hot topic in electromagnetics research due to the possibilities they offer for the control of the electromagnetic wave radiation. In particular, MTS at mmWaves are key elements in the context of modern communication systems (5G, 6G) as they open new ways to steer the beams in arbitrary directions as well as improve in general the radiation characteristics of wireless devices. In the thesis MTS have been combined with GW to extend the functionality of compact devices in a fully metallic design. A flat Luneburg lens (LL) antenna based on a bed of nails fed by a GW horn antenna has been designed and experimentally demonstrated. The refractive index needed to modulate the Luneburg equation has been implemented using small pins with different heights. This design presents a significant bandwidth and good directivity values in a compact implementation.

Also related with lenses but using a different concept, a compact pillbox reflector based on a geodesic lens has been proposed at 60 GHz. A geodesic lens is based on a parallel plate waveguide which achieves the focusing properties by introducing a curved shape and hence varying effective optical path. The system has been implemented in a dual-layer parallel plate waveguide. In the proposed design the wave stemming from the geodesic lens in a first layer is reflected by a parabolic mirror connecting the rims of the

two layers that directs the wave towards the second layer where it is radiated. To make the system more compact, the lens is designed with a virtual focus so that the actual source can be placed closer to the lens.

An open technological challenge is to achieve high gain antennas at the higher end of the mmWaves band, close to the terahertz range (300 GHz), where a wide bandwidth is available thanks to the increased operation frequency. An initial step to cover this gap has been done in the thesis by proposing an antenna lens system based on a metamaterial flat hyperbolic lens illuminated by an H-plane horn antenna designed at 300 GHz using groove GW technology. Both devices, the metalens, and the GW antenna achieve excellent radiation results when combined. Furthermore, the manufacturing process is analysed in detail and a realistic proposal based on metallized micromachined silicon is presented.

Finally, reconfigurable and active metasurfaces are a disruptive topic with multiple applications in smart wireless systems. Here, a dynamically reconfigurable reflectarray (RA) using liquid crystal (LC) operating above 100 GHz has been numerically and experimentally demonstrated. This is a relevant and challenging result due to the stark difference between the operation wavelength (of the order of millimeters) and the typical thickness of a LC substrate (some micrometers). The good performance of the prototype paves the way towards more ambitious designs aligned with the requirements of modern communication systems at mmWaves.

Resumen

Esta tesis presenta la evolución de una línea de investigación guiada por el desarrollo de estructuras metálicas para mejorar las propiedades de radiación de dispositivos que operan en ondas milimétricas (mmWaves).

Cubre diferentes aspectos de las soluciones de alta frecuencia como la tecnología Gap Waveguide (GW) para guiar ondas con bajas pérdidas y alta eficiencia superando las limitaciones de las guías de onda clásicas. Usando GW como enlace común, se han desarrollado tres antenas diferentes para generar polarización circular (CP) de una manera simple y compacta utilizando una técnica de alimentación basada en la diferencia de longitud de los brazos ortogonales que excitan una ranura en la placa superior. Cada una de estas antenas sigue una evolución natural desde el diseño inicial que presenta los fundamentos básicos de funcionamiento hacia topologías más complicadas con el objetivo de aumentar la directividad.

Las metasuperficies (MTS) son otro tema candente en la investigación electromagnética debido a las posibilidades que ofrecen para el control de la radiación de ondas electromagnéticas. En particular, los MTS en ondas milimétricas son elementos clave en el contexto de los sistemas de comunicación modernos (5G, 6G), ya que abren nuevas formas de dirigir los haces en direcciones arbitrarias y, en general, mejoran las características de radiación de los dispositivos inalámbricos. En la tesis, las MTS se han combinado con la tecnología GW para ampliar la funcionalidad de los dispositivos compactos en un diseño totalmente metálico. Se ha diseñado y demostrado experimentalmente una antena de lente Luneburg plana (LL) basada en un lecho de clavos alimentado por una antena de bocina GW. El índice de refracción necesario para modular la ecuación de Luneburg se ha implementado utilizando pequeños pines con diferentes alturas. Este diseño presenta un ancho de banda significativo y buenos valores de directividad en una implementación compacta.

También relacionado con las lentes, pero utilizando un concepto diferente, se ha propuesto un reflector doble capa compacto basado en una lente geodésica a 60 GHz. Una lente geodésica se basa en una guía de ondas de placas paralelas que logra las

propiedades de enfoque introduciendo una forma curva y, por lo tanto, variando la trayectoria óptica efectiva. El sistema se ha implementado en una guía de ondas de placas paralelas de doble capa. En el diseño propuesto la onda proveniente de la lente geodésica en una primera capa es reflejada por un espejo parabólico que conecta los bordes de las dos capas que dirige la onda hacia la segunda capa donde es radiada. Para hacer que el sistema sea más compacto, la lente está diseñada con un foco virtual para que la fuente real pueda colocarse más cerca de la lente.

Un desafío tecnológico abierto es lograr antenas de alta ganancia en el extremo superior de la banda de ondas milimétricas, cerca del rango de los terahercios (300 GHz), donde se dispone de un amplio ancho de banda gracias a la mayor frecuencia de operación. En la tesis se ha dado un paso inicial para cubrir este vacío proponiendo un sistema de antena-lentes basado en una lente hiperbólica plana de metamaterial iluminada por una antena de bocina en plano H diseñada a 300 GHz utilizando tecnología GW. Ambos dispositivos, la metalente y la antena GW logran excelentes resultados de radiación cuando se combinan. Además, se analiza en detalle el proceso de fabricación y se presenta una propuesta realista basada en silicio metalizado micromecanizado.

Finalmente, las metasuperficies reconfigurables y activas son un tema disruptivo con múltiples aplicaciones en sistemas inalámbricos inteligentes. Aquí, se ha demostrado numérica y experimentalmente un reflectarray (RA) dinámicamente reconfigurable que utiliza cristal líquido (LC) y que opera por encima de 100 GHz. Este es un resultado relevante y desafiante debido a la marcada diferencia entre la longitud de onda de operación (del orden de milímetros) y el grosor típico de un sustrato LC (algunos micrómetros). El buen desempeño del prototipo allana el camino hacia diseños más ambiciosos alineados con los requerimientos de los modernos sistemas de comunicación en ondas milimétricas.

Contents

List of Figures

List of Tables

Acronyms

5G. Fifth Generation
6G. Sixth Generation
AC. Alternating Current
AMC. Artificial Magnetic Conductor
AR. Axial Ratio
AUT. Antenna Under Test
BE. Bull's-Eye
BW. Bandwidth
CNC. Computer Numerical Control
CP. Circular Polarization
D. Diamond
DH. Diamond Horn
DHG. Diamond Horn Groove
GGW. Groove Gap Waveguide
GLL. Geodesic Luneburg Lens
GO. Geometrical Optics
GP. Ground Plane
GRIN. Graded Index
GW. Gap Waveguide
HIS. High Impedance Surface
HL. Hyperbolic metalens
LCs. Liquid Crystals
LL. Luneburg Lens
LWA. Leaky Wave Antennas
MGW. Microstrip Gap Waveguide
mmWave:. Millimeter-wave
MTS. Metasurfaces
OPL. Optical Path Length
PCB. Printed Circuit Board
PEC. Perfect Electrical Conductor
PMC. Perfectly Magnetic Conducting
PPW. Parallel Plate Waveguide
RAs. Reflectarrays
RGW. Ridge Gap Waveguide
RHCP. Right-Handed Circular Polarization
SLL. Sidelobe Level
TEM. Transverse Electromagnetic
TM. Transverse Magnetic

WLANs. Wireless Local Area Networks

η_{eff}. Aperture Efficiency

Chapter 1: Introduction and State of the Art

1.1 Motivation

This thesis presents antenna designs and other devices operating in the millimeter-wave (mmWave) spectrum to address some of the problematics that are emerging due to the rapid development of digital communications in modern society. Amongst the pending challenges for the next generation wireless communication systems are: achieving complete transceivers with low area and low loss, including integration between passive and active components, developing high performance antenna arrays, as well as the use of advanced packaging techniques, all of this keeping at the same time cost-effective systems. In addition, with the constant evolution of each new wireless standard, higher data rates are required to satisfy the demands of a hyperconnected society in the context of the Internet of Things paradigm.

The gradual saturation of the lower part of the radio spectrum and the broader bandwidth needed has spurred research towards efficient antennas and feeding methods at higher frequency bands, mainly millimeter and terahertz waves. Nevertheless, fundamental obstacles must be circumvented to fully develop high-frequency technology. One of them is the problem of guiding waves with low loss. In general, conventional dielectric materials have increasing losses as the frequency approaches the millimeter-wave band, ruling out planar solutions such as microstrip and coplanar waveguides [1], [2]. The loss of conductors also rises with frequency mainly due to the roughness introduced by conventional manufacturing techniques, which is no longer negligible in the mmWave band. In addition, standard metallic waveguides require precise screwing or welding techniques when they are fabricated in two blocks.

The new fifth-generation (5G) and the incoming sixth-generation (6G) mobile standards demand wide channelization bandwidths, high transmission speed, and low latency [3]. These requirements can be satisfactorily addressed in the mmWave band. However, some challenges must be considered to fully develop all the potential of mmWave in wireless communication technologies. For example, highly directive antennas are needed to compensate for the increased free-space propagation loss compared to microwaves (due to the higher carrier frequencies) as well as additional losses due to the attenuation of atmospheric gases; in addition, wide-angle scanning is also required in satellite applications [4].

The research carried out in this thesis is aimed towards giving satisfactory answers to these open questions, focusing principally on antennas and metasurface devices in the mmWave band. To this end, novel methods and concepts especially developed for these challenges are employed, covering gap waveguide (GW) technology, metasurfaces (MTS), both static and reconfigurable, metalenses and geodesic lenses. All these solutions can lead to radiating systems with different characteristics, including high efficiency, high directive beams, and a wide scanning range.

1.2   Millimeter Waves in the context of high capacity wireless systems

Millimeter-wave frequencies, located between the microwaves and the infrared waves, have the potential to provide a solution to the growing demand for bandwidth and high-data rates required by modern communication systems. The mmWave range goes from 30 to 300 GHz, with wavelengths between 10 mm and 1 mm [5], [6].

Over the last few decades, affordable technologies have enabled a widespread use of mmWave. This has resulted in the expansion of wireless communications with high data rates overcoming the limits imposed by the saturation of the spectrum at lower frequencies. However, the signal suffers attenuation at these frequencies due to the

presence of atmospheric absorption peaks and the increased propagation losses in free space compared to microwaves due to the smaller wavelength. Therefore, these frequencies are not suited for long-distance communications [7].
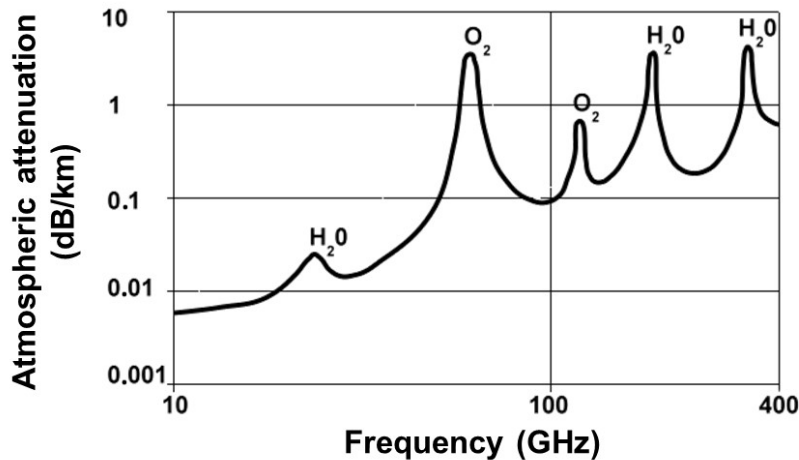
Fig. 1.1 Atmospheric attenuation in dB/km as a function of frequency over the mmWave band. Absorption peaks at specific frequencies arise due to molecular resonances of atmosphere constituents such as water vapor (H2O) and oxygen (O2). The scale is exponential.

Beyond that, mmWave are suitable for short-distance high-speed wireless applications, but are limited to short distances due to relatively high free-space loss (due to high frequency), atmospheric absorption and multipath (Fig 1.1). However, in the context of the new communication standards such as 5G, the incoming 6G, and the IoT, this is no longer a limitation since short-distance links with high capacity are proposed. Moreover, to increase the range high gain antennas can be employed. Finally, in some cases where secure communications are mandatory, the rapid decay of these waves along with their reduced wall penetration make them an optimal solution. Therefore, mmWaves is a promising technological for future wireless communication systems. In the following, the main benefits of the use mmWave range are presented:

Large bandwidth: A large bandwidth means higher data transfer rates, attaining speeds of about 10 Gbps or more. In any case, more than the 1 Gbit/s limit when using microwave

frequencies. This makes high-quality video streaming, real-time gaming, and other bandwidth intensive wireless applications a reality [8].

High gain antenna and components are physically smaller: The antennas and components at mmWave are usually small compared to those for lower frequencies. This makes it possible to design physically smaller circuitry and equipment. For instance, a half-wave dipole operating at a 900 MHz cellular frequency is more than 150 mm long, but this size is reduced to 2.5 mm at 60 GHz in free space or less if a dielectric substrate is employed. It is therefore possible to encapsulate miniaturized and lightweight complete radio systems or build phased arrays with multiple elements on a chip [9].

Low interference and increased security: The narrow beam and short-range can be a benefit since there is less interference from nearby systems. In addition, it is much harder to intercept the signals leading to increased security communications since the signal is restricted to a small area [10].

Unlicensed bands: Most applications have been designed to operate up to 30 GHz frequencies. This range is currently congested, hence limiting the development of newer technologies. On the other hand, the mmWave spectrum, which was previously reserved for military and scientific applications, is slowly becoming available for consumer and commercial applications.

Multi Gbit/s short-range wireless communications: With data rates reaching 10 Gbps, some possible applications include high-speed point-to-point as wireless local area networks (WLANs) and broadband access, mobile and wireless networks, streaming high-resolution video, automotive radar solutions, and more [11].

These advantages imply the use of mmWave systems to satisfy several demands, e.g., high-definition video [12], satellite communications, security systems [10], automotive radar [13], [14], human body scanner [15], and more.

The following sections are analyzed the state of the art of some relevant technologies used for mmWave communication systems. The technological solutions summarized

there are some of the most promising alternatives to tackle the main problems behind the development of wireless mmWave systems. The main aim is to combine them to propose wireless solutions operating at mmWave and give new alternatives to the engineering community for the complete development of this band.

1.3   Gap Waveguide Technology Fundamentals

As mentioned in the previous sections, losses at mmWave systems are critical. The classical methods to design feeding networks based on dielectric materials are not effective due to the presence of absorption peaks. Likewise, classical metallic solutions such as hollow waveguides fabricated with standard manufacturing techniques present a roughness comparable to the wavelength, leading to high ohmic losses. In addition, they require precise and expensive screwing or welding techniques when fabricated in two blocks.

In order to circumvent this problem, alternatives such as GW technology, introduced by Prof. Per-Simon Kildal [16], [17], have been specifically developed to give a satisfactory answer to the problem of guiding waves in the mmWave band. Compared to microstrip transmission lines, coplanar waveguides and substrate integrated waveguides, GW can keep a planar profile and still have a low loss since it can guide waves in the air without the need for dielectric materials. In addition, this technology does not need good metal contacts between the parallel metal plates, making the fabrication process robust to tolerances and cost-effective. For these reasons, GW is a solid alternative for hollow waveguides and microstrip lines for high-frequency applications [18], [19].

The main characteristic of this technology (Fig. 1.2) is the use of two parallel plates, a perfect electrical conductor (PEC) and an artificial magnetic conductor (AMC), creating a high impedance condition forcing a cut-off of all parallel-plate modes [20], [21]. Wave propagation is forbidden in the gap between a PEC and an AMC if the gap height is below $\lambda/4$, due to the boundary conditions and therefore the wave is confined to propagate in

the region determined enclosed by the AMC plates. As perfect magnetic conductor does not exist in nature, the AMC is usually implemented using a periodic metallic pin structure tuned to provide a high impedance surface.

Fig. 1.2(a) represents the dispersion diagram of a metallic pin array of side of a_p, height of h_p, periodicity p_p and distance to the upper metallic layer (gap) of 0.25 mm. With these dimensions, a bandgap arises centered at 60 GHz and extending from 40 to 80 GHz. The bandgap appears as long as the distance between the upper metallic layer and the pin array is less than $\lambda_0/4$, with λ_0 the central bandgap wavelength.
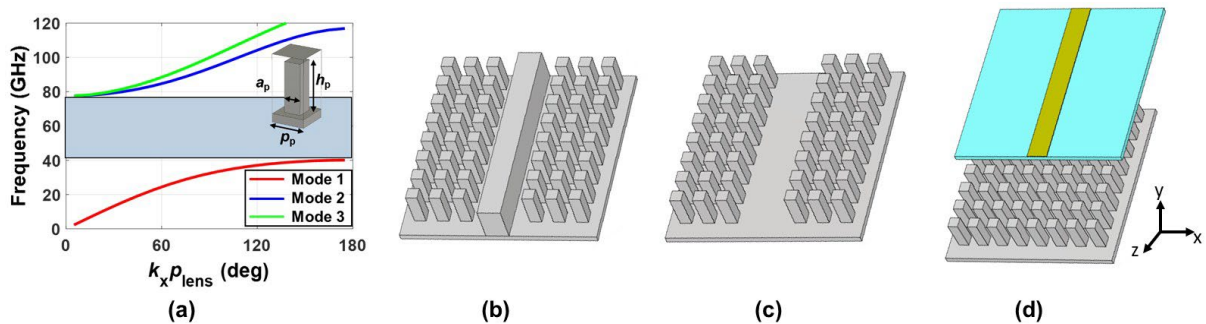
Fig. 1.2 (a) Dispersion diagram of a periodic metallic pin array structure (unit cell shown in the inset) where a_p is the side, h_p the height and p_p the periodicity. Schematic of bottom layers of the three main variants of GW technology. (b) Ridge gap waveguide (RGW). (c) Groove gap waveguide (GGW) and (d) Microstrip gap waveguide.

There are different versions of GW technology depending on the shape of the guiding region and desired propagation characteristics. The most popular ones are ridge and groove gap waveguides (RGW and GGW) and are shown in Figs. 1.2(b) and (c). In them, the electromagnetic wave propagates respectively along the metal ridge of the central groove flanked by the metallic pin array that emulates an AMC [22], [23]. The third version in Fig. 1.2(d) is called inverted microstrip gap waveguide (MGW) because it is similar to inverted/suspended microstrip lines. In this case, the wave propagates in the air gap between the metallic strip and the upper metal plate, forced by the AMC placed below the substrate of the microstrip line [24]. The two first designs do not need any dielectric substrate so they avoid additional dielectric losses and hence have lower propagation

loss compared to the third case [18], [25]. On the other hand, MGW can be integrated easily with active components, making it a good alternative for monolithic microwave integrated circuits applications.

1.3.1 Circular Polarization Gap Waveguide Antennas

Polarization of a radiated wave is defined as "that property of an electromagnetic wave describing the time-varying direction and relative magnitude of the electric-field vector; specifically, the figure traced as a function of time by the extremity of the vector at a fixed location in space, and the sense in which it is traced, as observed along the direction of propagation." Polarization is then the curve traced by the end point of the arrow (vector) representing the instantaneous electric field. By convention, the field must always be observed along the direction of propagation [26].

Polarization may be classified as linear, circular, or elliptical. The latter is the most general case and hence linear and circular polarizations are just special cases of elliptical polarization but with important technological relevance as most communications systems are designed to operate either with linear or circular polarization.

Circular polarization (CP) in wireless communications systems has several advantages over linear polarization: CP does not require polarization alignment between the transmitter and the receiver, is more robust against multipath effects and against polarization rotation [27]. These are key characteristics in mmWaves wireless communication systems which under the IoT paradigm will operating massively in indoor scenarios (prone to multipath and especially harsh at mmWaves) or in modern high-altitude platform systems deployed to give coverage to relatively large areas and that can suffer from Faraday rotation due to the atmosphere. Hence, antennas with CP operating at mmWaves are of high interest for the technological development of these applications. Here this need is addressed using GW as a low loss alternative to guide waves compared to standard metallic waveguides. In addition to this, thanks to its topology based on metallic pin arrays, GW technology allows introducing bends and curvatures in a simple way, overcoming the strict limitations of standard metallic waveguides.

In [28], a CP antenna operating in the 75–80 GHz band was demonstrated using rotated rectangular slot arrays laying over a bed of nails. An RGW scheme was implemented to feed an array of 1×4 elements. Following a similar procedure, an RGW antenna based on slot arrays operating at the Ka-band was presented in [29], [30]. In [31], a single layer dual CP antenna array operating at 77 GHz was proposed based on RGW technology. The antenna consisted of eight U-shaped slots, fed by two feeding networks for the generation of dual CP, see Fig. 1.3(a). An exciting evolution of GW was presented in [30]–[33] by combining RGW and GGW in an antenna array of 4×4 chamfered cylindrical radiating apertures fed by a corporate GW network, see Fig. 1.3(b). Another way to design CP antennas using MGW was demonstrated in [34] and [35]. In [34], the antenna was composed of two substrates with a ring slot etched on the upper substrate to generate CP. This resulted in a compact structure in MGW technology. Finally, a new design for a wideband CP spiral antenna array fed by a differential aperture coupling at 30 GHz was fabricated [35]. The excitation was done by two vias located at the lateral sides of a transverse slot etched on the lower substrate. An array of 2×2 spiral antennas with two-arms was implemented to generate CP. The sequential feeding network was based on low-loss MGW technology, Fig. 1.3(c).
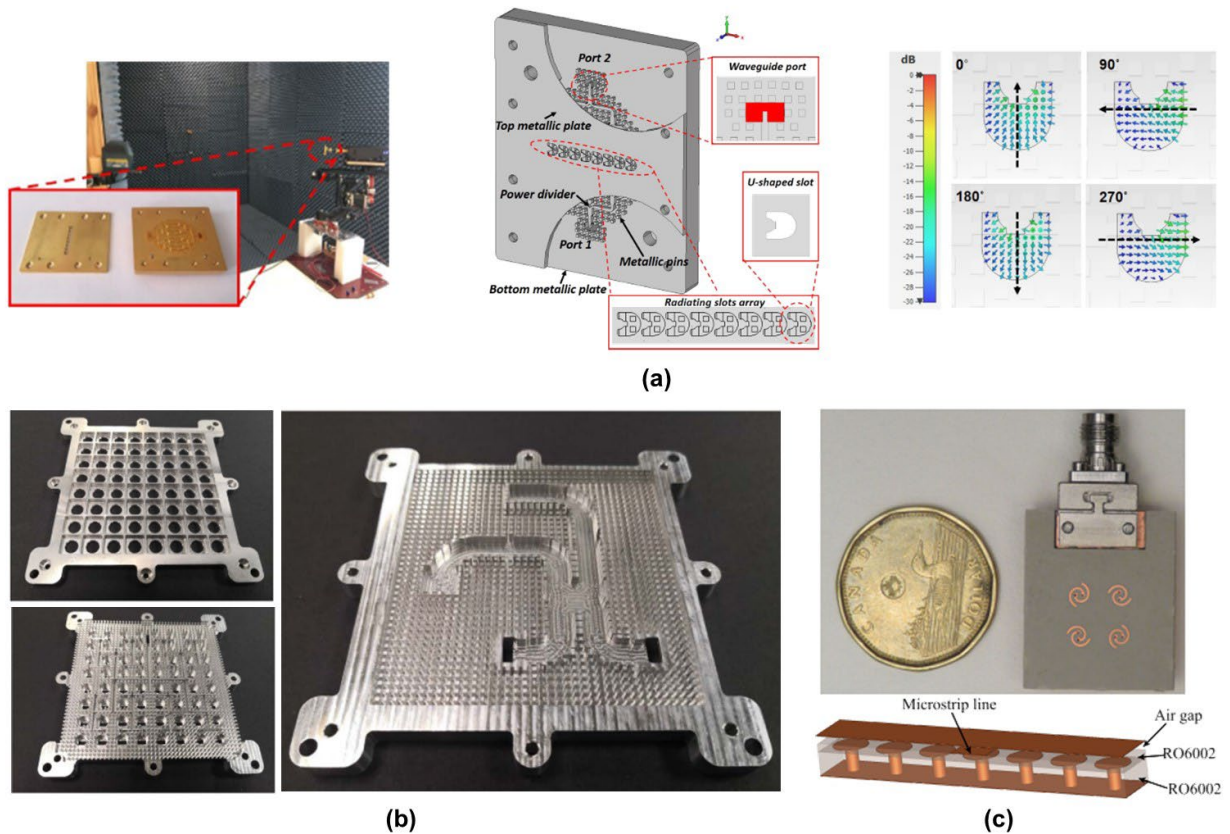
Fig. 1.3 Three examples of GW technology arrays. (a) RGW array antenna at 77 GHz, [36]. (b) GGW dual CP aperture array antenna at *K*a-band, [33]. (c) MGW spiral antenna at 30 GHz, [35]

Up to this point, it is clear that GW is a technology suitable to solve some of the challenges that arise at mmWave, improving the performance compared with standard microstrip transmission lines and waveguides.

1.4 Corrugated Leaky Wave Antennas

Leaky waves have been among the most active research areas in microwave engineering over the second half of the 20th century [37], [38]. Leaky wave antennas (LWA) are a particular member of the traveling-wave antennas family and consist of a guiding structure on which a traveling wave leaks our radiation as it propagates. The radiation region usually extends over several wavelengths and it happens that the longer

the aperture, the narrower the radiation beam is. As a result, LWA have several advantages that include simplicity of design since no feeding network is needed. Also, they have the property of frequency scanning of the radiation pattern, which is helpful in many applications, as in point-to-point or point-to-multipoint wireless and satellite systems. However, their application in such systems has been limited due to the beam squint which leads to gain losses at the desired radiation direction.

The first investigated LWA was proposed by Hansen in the late 1930s [39]. He proposed a radiating structure by opening a longitudinal slit in the side of a rectangular waveguide, see Fig. 1.4. Radiation happens because the mode inside a waveguide is a fast wave with a phase velocity greater than the speed of light so there is an extra momentum that allows radiation through the aperture. In general, the mechanism of radiation of any LWA is linked with the excitation of a fast wave. This can also be obtained by introducing periodic perturbations in an otherwise slow wave structure and tuning the parameters so that a high order space harmonic (usually n = -1) enters the radiation cone.

LWAs radiate continuously along its length, and hence the propagation wavenumber k_z is complex, consisting of both a phase and an attenuation constant. The phase constant (β) of the wave controls the beam angle (which can be varied changing the frequency), while the attenuation constant (α) controls the beamwidth [40]. The direction of the main radiation beam can be calculated with the next equation:

$$\theta = \sin^{-1}\left(\frac{\beta}{k_0}\right) \tag{1.1}$$

where θ is measured from broadside and k_0 is the free-space wavenumber. As mentioned above, due to radiation loss, β is associated with an attenuation constant α. The beamwidth becomes narrower as α is reduced and the structure is not truncated so that the leaky-wave propagates a longer distance before attenuating and hence, the effective area is maximized. The most important properties of leaky waves was given by Tamir and Oliner [41].

9
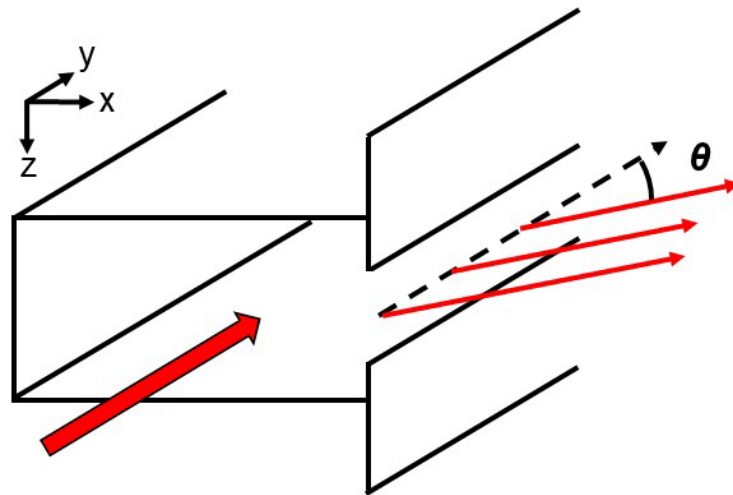
Fig. 1.4 Representation of a slotted guide (patented by W. W. Hansen in 1940)

Bull's-Eye (BE) antennas [42] are a particular case of the larger family of periodic leaky wave antenna [37]; most of them consist of a metallic plate with a central slot surrounded by concentric corrugations. BE antennas have an interesting characteristic: they usually radiate at broadside with a significant gain, removing one of the classical limitations of LWA which is the open-stop band effect that precludes radiation at broadside [43]. This performance is achieved by designing the periodic corrugations in such a way that each half of the BE antenna radiates at opposite directions but in angles very close to broadside, giving rise to a single lobe by merging the radiation of both halves.

BE antennas have been considered a simple alternative to horns and parabolic antennas [44], [45]. Moreover, they fit perfectly at mmWave applications because they are fully metallic designs without additional dielectric losses. BE antennas follow the classical implementation of a periodic ring structure around a central slot fed by a standard waveguide attached to the backplate [42], see Fig. 1.5(a). Fig. 1.5(b) shows a high gain BE antenna was designed in [46], using an aluminum plate carved with a sinusoidal profile working at 77 GHz and achieving 28.9 dB of gain. Following the classical procedure, a large number of corrugations was implemented and, as a consequence, a large area and low aperture efficiency was achieved. In [47] (Fig. 1.5(c)), these limitations were removed, optimizing the resonant modes inside the grooves in such a way that a

gain of around 20 dB was obtained with just two corrugations. In this case, the aperture efficiency increased to 32% in a prototype operating at 60 GHz.

A variant using a low-cost 3-D printing stereolithography technique was designed in [46] . As an alternative to the traditional manufacturing techniques, this BE antenna operating at 96 GHz was experimentally studied; even with those limitations, a significant gain of around 17 dB was achieved. In addition, elliptical corrugations were implemented in this design in order to radiate at an angle different from the broadside direction.

(a)

(b)

(c)
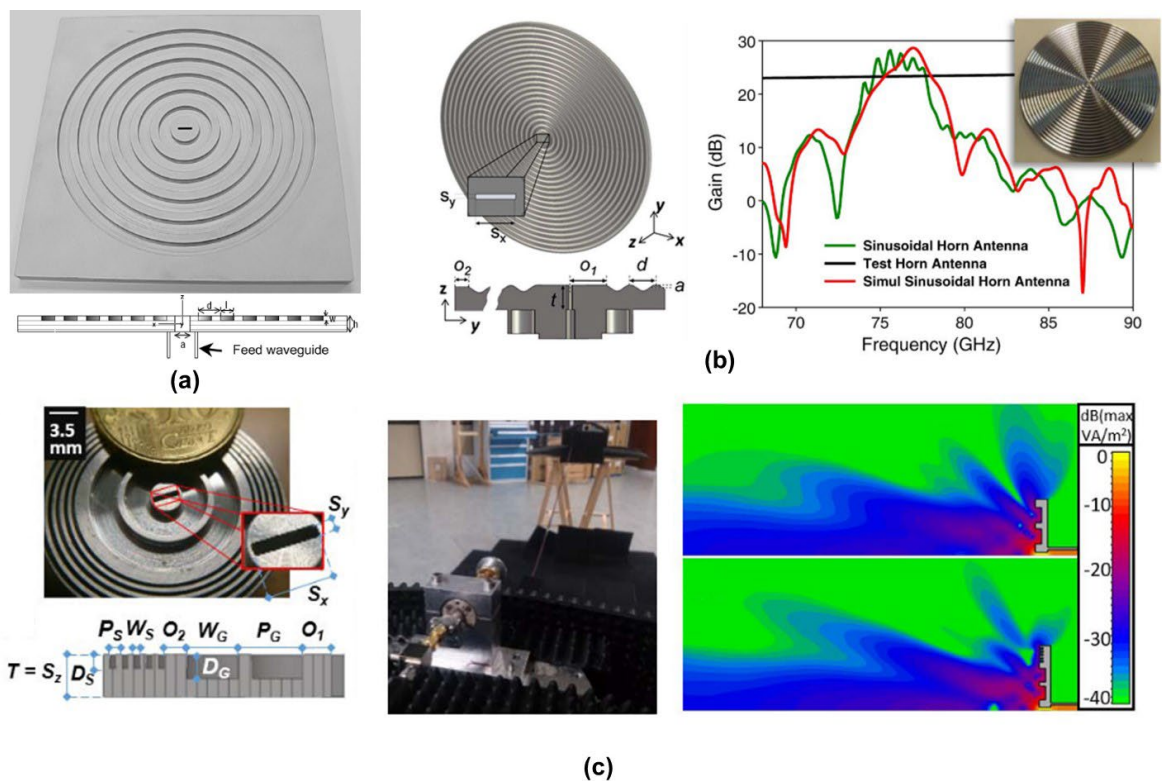
Fig. 1.5 Bull's Eye antennas with, (a) Metallic concentric corrugations uniformly separated, [42]. (b) Metallic concentric corrugations with a sinusoidal profile, [46]. (c) High aperture efficiency achieved by widening the corrugation width [47].

1.5 Metasurfaces for Surface Wave Manipulation

Metasurfaces are thin bi-dimensional metamaterial screens which can control the characteristics of electromagnetic waves (polarization, reflectance, transmittance, etc.). Hence compared with volumetric metamaterials which are typically bulky, MTSs offer considerable benefits in flat solutions. In this sense, they can be considered as the two-dimensional alternative to metamaterials with the additional advantage that they are flat. Their range of applications is very broad, from microwaves to optics [48]. The main advantage of these structures is the electrically small size of their unit cells in such a way that the interacting electromagnetic fields see the textured surface as a homogeneous unit and behave as flat artificial materials. Nowadays, several implementation methods have been investigated and validated. The most popular ones are based on metallic elements printed on dielectric substrates [49]–[52]. Nevertheless, metal-only [53]–[57] and dielectric-only [58], [59] structures can also be found in the literature.

Metasurfaces have been employed in a vast variety of applications, such as antennas, lenses, polarizers, absorbers, and waveguide systems [17], [55], [60]. The design of flat metalenses (i.e. lenses based on metasurfaces) has received particular attention in recent years as an alternative to conventional volumetric lenses due to the high directivity and scanning resolution they offer with a very small profile. At low frequencies such as microwaves, lens antennas can be bulky due to the increasing wavelength, but are an exciting solution at high frequencies [61], [62]. Essentially, two types of flat metalenses can be identified: lenses able to collimate a wave in the direction normal to the aperture, and lenses that deal with waves propagating along a MTS enclosed inside an open [63], [64] or a parallel plate waveguide (PPW) [49], [65], [66] (see some examples of metalenses in Figs. 1.6-1.9). In the following section, a metalenses of the second type will be presented using hyperbolic shape

There are methods to improve and achieve more compact lens systems based principally on the concepts of transformation optics proposed by Pendry [67] and Leonhardt [68] in 2006 which opened new avenues for applications like waveguide coupling [69], [70], lens compression [71], [72], lens fattening [73], [74], and directivity enhancement [75], [76]. Based on the form-invariance of Maxwell's equations,

transformation optics implies that a transformation medium where the permittivity is gradually varied can mimic space deformation [77], see Fig. 1.6(d). It has a direct application to lenses with a gradual index variation that allows control on the wave propagation. In the next section, a particular case will be explained in more detail following the Luneburg solution in considering again a metalens of the second type using a parallel plate waveguide.

Hence, it is clear that in most metalens designs found in the literature, the variations of the refractive index are obtained using layered dielectrics [78], photonic crystals [79], [80], or periodic structures [49], [55]. In all these methods the refractive index is modulated discretely. There is an interesting alternative called geodesic lenses that can modulate continuously the refractive index by introducing a shape variation, as will be explained in detail below.

1.5.1   Hyperbolic Lenses

Homogeneous lenses have been historically employed in microwaves principally to improve the directivity of horn antennas making their profile more compact. They usually consist of a single dielectric material whose profile is controlled to introduce an arbitrary phase delay in different directions to achieve conversion from a spherical to a plane wave at the output. The design is usually done using geometrical optics (GO). The most employed lens profiles in antenna applications are elliptical and hyperbolic shapes.

In recent years, and with the increasing applications at mmWave, new antenna designs have been proposed using homogeneous lens for the engineering community, such as horn antennas, slotted waveguide arrays, or even mmWave open-ended waveguides whose radiation is made more directive by adding a lens at the output [81]–[86]. For example , in [81] and [82] a hyperbolic lens was used to improve the directivity and reduce the sidelobes of horn antennas working at 60 GHz, Fig. 1.6(a). In [84], a hemispherical lens fabricated using additive manufacturing was directly matched to a WR-3 waveguide (220-320 GHz), Fig. 1.6(b). Lenses can also be inserted in systems with angle scanning

capabilities such as slotted waveguide arrays, such as the design presented in [85], see Fig. 1.6(c).
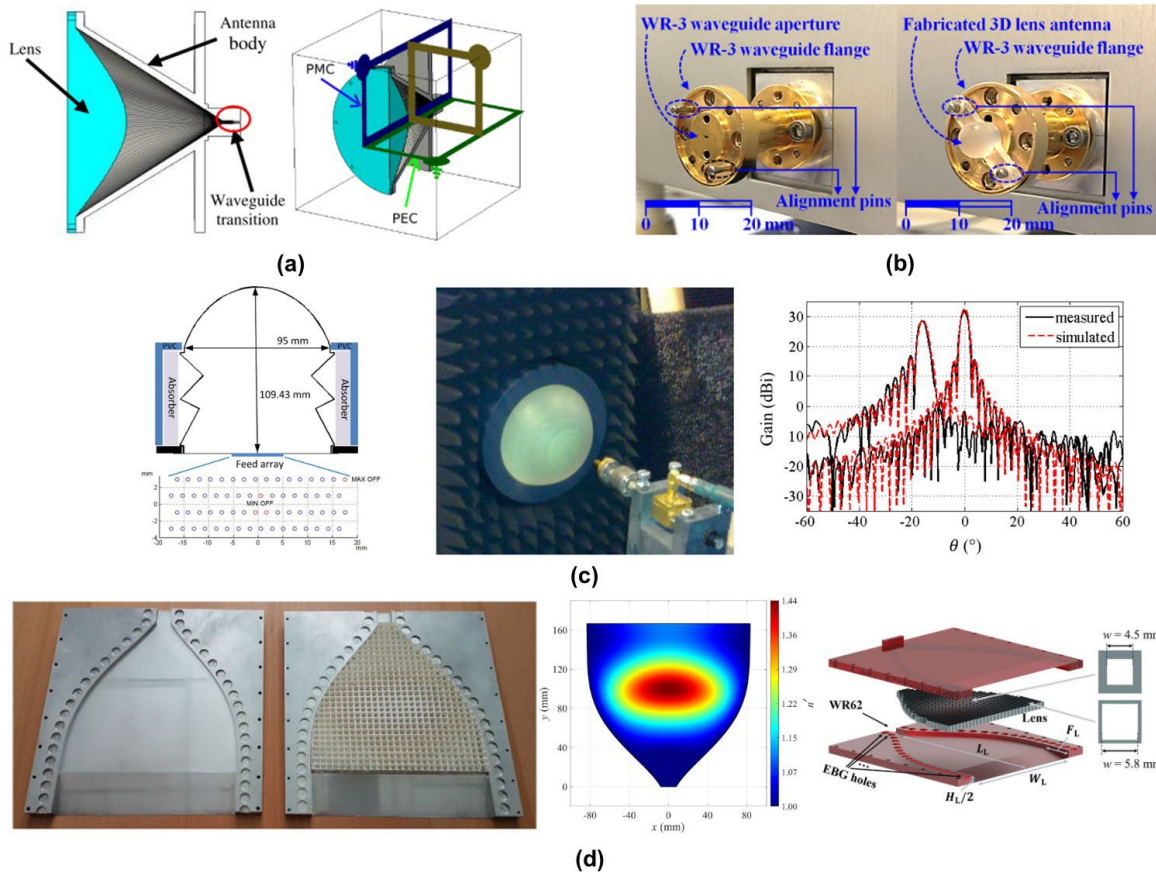
Fig. 1.6 Examples of, (a) Hyperbolic lens horn antenna at 60 GHz, [82]. (b) Hemispherical lens antennas with a homogeneous photopolymer, [84] (c) A mmWave integrated lens antenna for E-band beam steering, [85]. (d) H-plane horn antenna using conformal transformation optics, [77].

1.5.2   Luneburg Lens

One of the most classical lenses designs with a gradual index variation is the so-called Luneburg Graded Index (GRIN) lens. More than five decades ago, Luneburg found an analytical solution for the radial index profile of a sphere able to collimate the rays launched by a point source placed on its boundary [87]. The Luneburg lens (LL) has a rotationally symmetric GRIN profile, transforming a spherical/cylindrical wave into a

planar wave with perfect matching to free space. An interesting property of this type of lenses is that they can generate directive beams independently of the frequency if they are made of a non-dispersive medium, leading to a broad operation band. In addition, due to the rotationally symmetric structure it is possible to achieve high directive beams at different directions by simply changing the position of the source at the lens boundary. Closely related with this, multiple feeds can be used to design omni-directional or wide-scanning angle structures.

The spherical shape of LL is bulky and difficult to integrate with planar circuits. Thus, a flat cylindrical LL is often preferred, also referred as two-dimensional (2D) Luneburg lens Fig.1.7(a). To date, there are several ways to implement the required refractive index using metasurface and metamaterial concepts with dielectric [49]–[52] and fully metallic configurations [53]–[57]. In [49] and [51], dielectric LLs were designed by modulating the surface impedance inside a parallel-plate waveguide. Fully metallic LL designs such as the ones presented in Fig. 1.7(b) and (c) are preferable at mmWave to avoid dielectric loss. In [54] and [55] multibeam LL antennas were designed using a bed of nails to modulate the refractive index, with a good performance in both cases. To simplify the manufacturing process, in [53] a bed of nails with homogenous pin height was proposed, implementing the refractive index modulation by varying the height of the metallic plate opposite to the bed of nails.
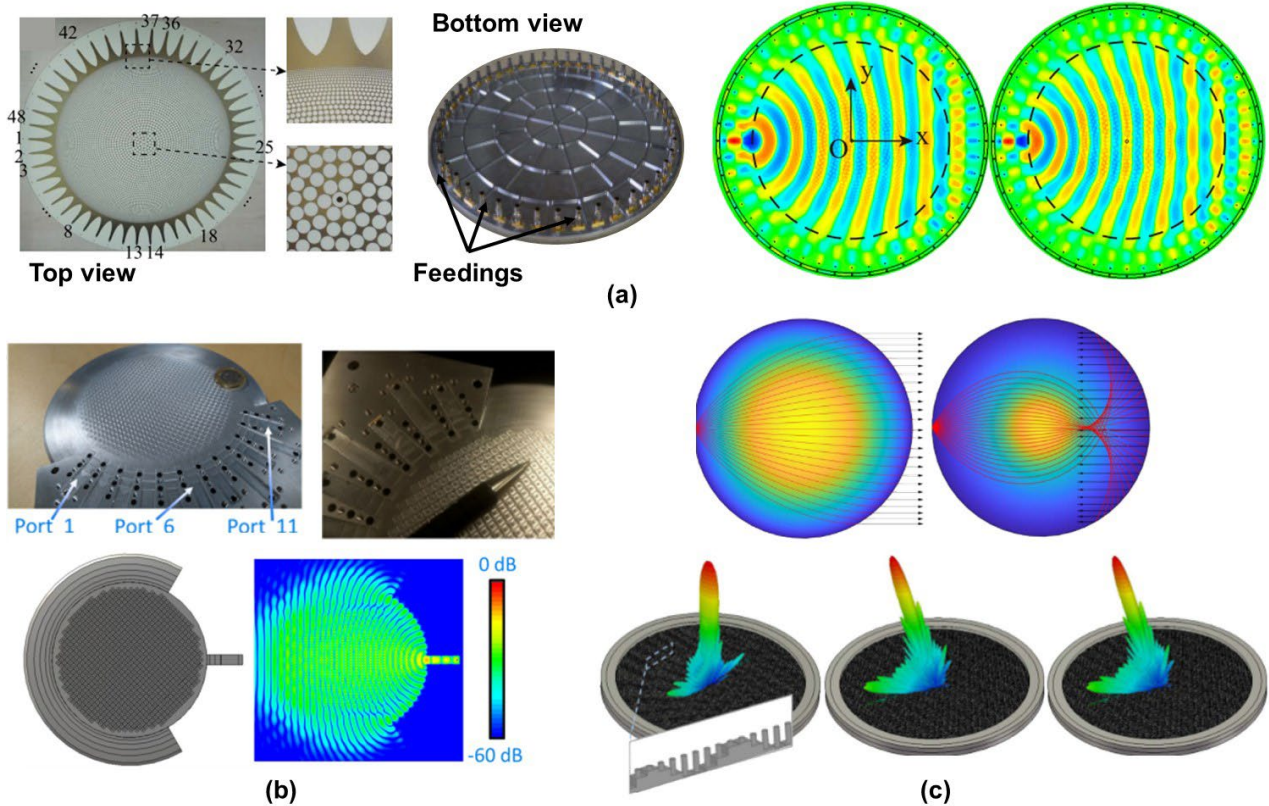
Fig. 1.7 Several examples of Luneburg lens antennas. (a) Effective refractive index synthesized using dielectric discs of different sizes, [51]. (b) Fully metallic Luneburg lens at Ka-band, [55]. (c) Pillbox metalens-antenna based on a bed of nails, [56].

1.5.3   Geodesic Lenses

The concept of geodesic lenses was introduced by Rinehart in the 40s [88]. He proposed to modulate the refractive index by varying the height and from here the OP to achieve the required phase at the output. This can be applied to emulate the behavior of the LL (Fig. 1.8). The rays described by the traveling electromagnetic wave are geodesics, following the shortest path on the surface between two points to achieve a prescribed phase delay. Structurally, geodesic lenses consist of curved surfaces which mimic an arbitrary refractive index distribution [89]–[91].
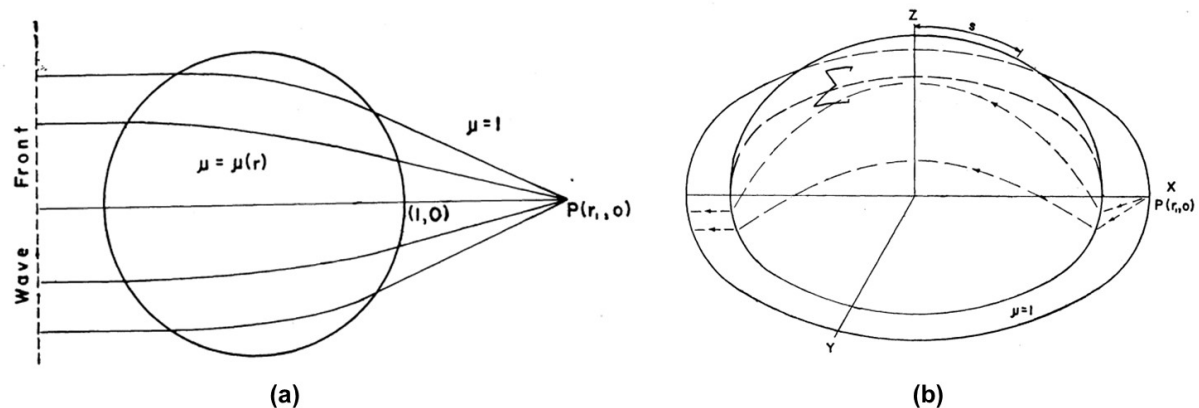
Fig. 1.8 (a) The Luneburg collimating lens (plane case) The index of refraction is unity outside the unit circle and is an appropriately chosen function $\mu(r)$ inside the unit circle for a given choice of point source *P*. (b) The Rinehart-Luneburg geodesic lens. The curved surface lens analogue of the Luneburg lens. With a constant refractive index of one, this surface has the same optical properties as the corresponding Luneburg planar lens. A parallel conducting plate waveguide with this surface as mean surface theoretically possesses the same focussing characteristics [92].

The most relevant concept in the geodesic lenses is that the refractive index in the surface can be constant, reducing the complexity and the manufacturing issues associated to GRIN metalenses. In order to confine electromagnetic waves and make them propagate along the geodesic shape, recent investigations have proposed two conducting surfaces. This solution is similar to a PPW filled with a homogeneous material, normally air. The gap between the two conducting surfaces should be small enough to allow only TEM mode propagation, typically below $\lambda_0/4$.

The evolution of wireless communications at high frequencies drives those solutions and hence the geodesic lens has gained interest in the engineering community. Due to their advantages, the geodesic shape, which is considered bulky at low frequencies, becomes an interesting choice at millimeter waves. Amongst their advantages are that the spherical symmetry allows multiple feeds to achieve wide-scanning designs, a fully metallic structure ensures high radiation efficiency, and the simple shape reduces manufacturing complexity and cost. However, the main drawback of this solution is its height, which can reach 0.6 times its radius and may be impractical for applications with

stringent integration constraints. The first solution to this problem was given by Kunz in the 50s [93]. He proposed to fold the lens, but this leads to a geodesic lens profile with a discontinuous derivative, introducing undesired reflections. In recent papers, this solution has been refined by proposing "waterdrop" profiles [94], [95] with the addition of chamfers to mitigate the losses caused by the mentioned discontinuous derivative.

In the last years, many investigations have used the geodesic LL antenna at mmWave to exploit their advantages. Interestingly, communication and radar systems require a wide scanning range with a reliable performance that fits perfectly with the geodesic design because it provides directive beams, scanning capability and robustness due to the fully metallic setup. A great diversity of designs has been published for different applications. In [94] ray-tracing design of geodesic lenses was proposed and a specific lens design at 30 GHz was further demonstrated with the ability to produce 21 beams to cover an angular range of ±75°. In order to obtain a compact structure, piecewise spline functions were optimized and implemented. A similar procedure was used in [96], but the geodesic shape was compressed using arcs of circumference instead of chamfers, a technique called the "waterdrop" method. In [97] a half-Luneburg geodesic lens working in the Ka-band was designed with a reduced angular range compared to others designs (±30°), but keeping radiation characteristics with a compact setup. These antennas present narrow pencil beams with a crossover point between two adjacent beams, typically 6 dB below the beam peak due to the physical separation between feeding points. A multibeam antenna to maximize coverage was designed in [98] to solve the wide scanning problem. In that case, a multiple beam coverage within ±67° was achieved.
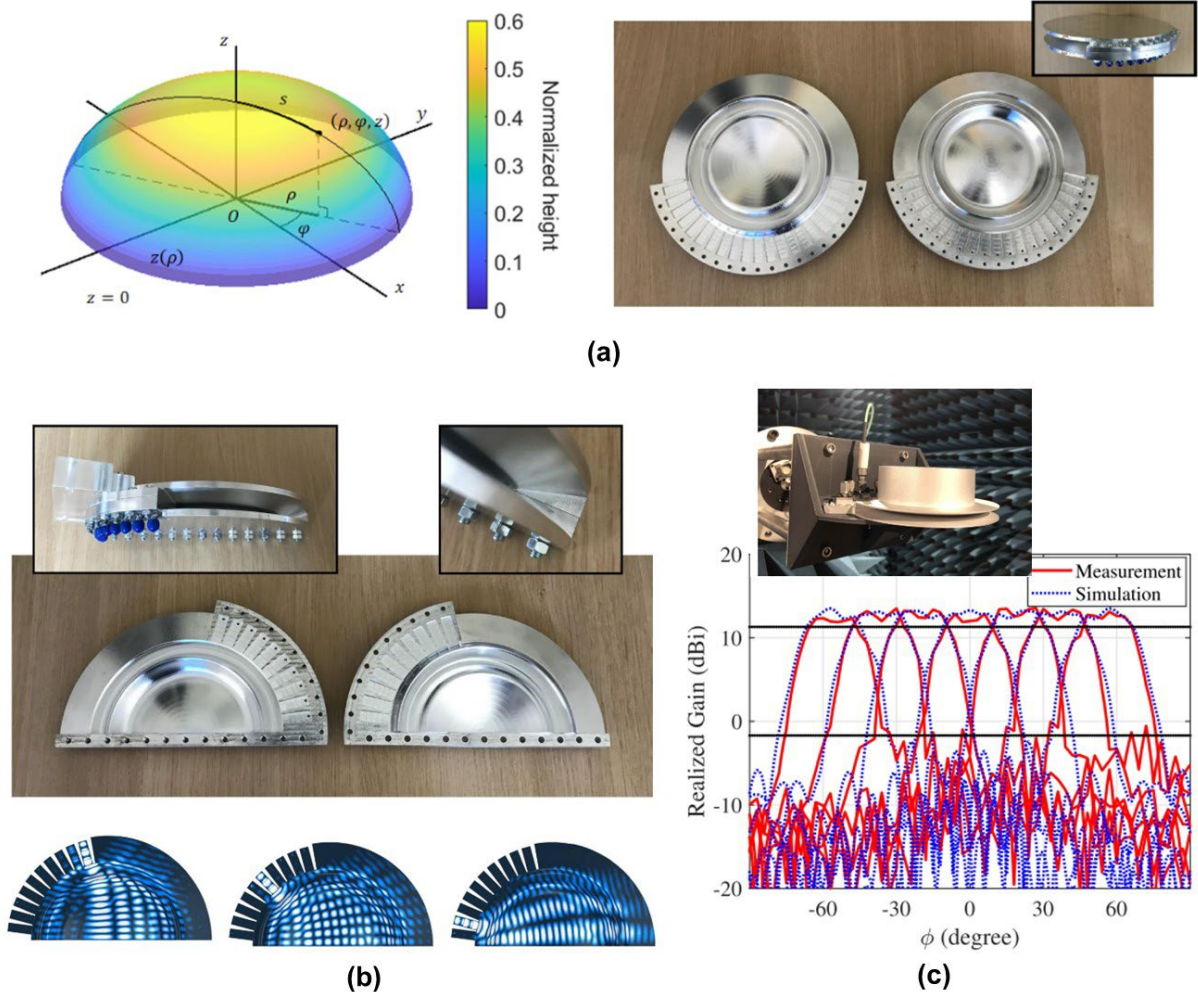
Fig. 1.9 Examples of geodesic lenses: (a) Using non-Euclidean TO at *Ka*-band, [94]. (b) Compact parallel-plate waveguide half-Luneburg geodesic lens, [97]. (c) Near-Field focusing geodesic lens antenna, [98].

1.6 Electronically Reconfigurable Metasurfaces

Up to this point, we have analyzed passive structures that generate high directivity and wide beam steering, which are crucial aspects in applications such as satellite communications, 5G, or the upcoming 6G datalinks. Mechanical solutions have been presented as alternative solutions to improve the beam scanning and avoid the crossover

level [99]–[101]. However, they usually rely on complex platforms and the weight is considerable compared to fully designs with electronic control.

Reconfigurable or tunable array antennas have attracted a significant interest in the last years due to their advantages over conventional phased arrays. Active devices have been an interesting option to modify the radiation properties of designs operating at mmWave. Incorporating active elements like positive-intrinsic-negative diodes and micro-electronic mechanical systems [102]–[105] leads to a reduction of the physical size with low cost and ease of integration. Nevertheless, the difficulty in manufacturing, the losses, and the parasitic effects on these devices at submillimetre waves discourage their use in frequency bands above 50 GHz [106]. Additionally, complex networks are required to feed these devices and integrate them in the final structure, taking care not to disturb the radiation performance and assuring compactness. Moreover, the bandwidth limitations due to the possible interactions of the fields with the feeding network or just for the operation band of the active element can hinder a satisfactory the final result. In the next section, a specific electronically reconfigurable MTS based on liquid crystal medium will be presented as an introduction to the work explained in detail in Chapter 6.

1.6.1 Liquid Crystal

Liquid crystals (LCs) are a promising alternative in the technology of electronically reconfigurable/switchable reflectarrays (RAs) operating in the mmWave and terahertz band. LC is a particular aggregate state of matter which has characteristics of both solids and liquids [107]–[109]. Two essential characteristics of LC molecules are that they are uniaxial and can be rotated/aligned by applying an external biasing voltage (amongst other techniques), allowing for tuning of the effective dielectric permittivity, see Fig. 1.10. Since their introduction [110], the main applications of LCs have been related to high-resolution displays [108] and spatial light modulators operating at optical frequencies [111]. A recent work [112] has demonstrated an active system integrated with an LC plasmonic metasurface, specifically used to develop electrically switchable plasmonic-metasurface-based color tags. This work demonstrated that the dynamic wavelength shift

in the devices is more significant than 100 nm at a low driving voltage varying from 0 to 5 V, showing the strong potential of active LC-plasmonic metasurface to realize the next-generation dynamic optical devices.
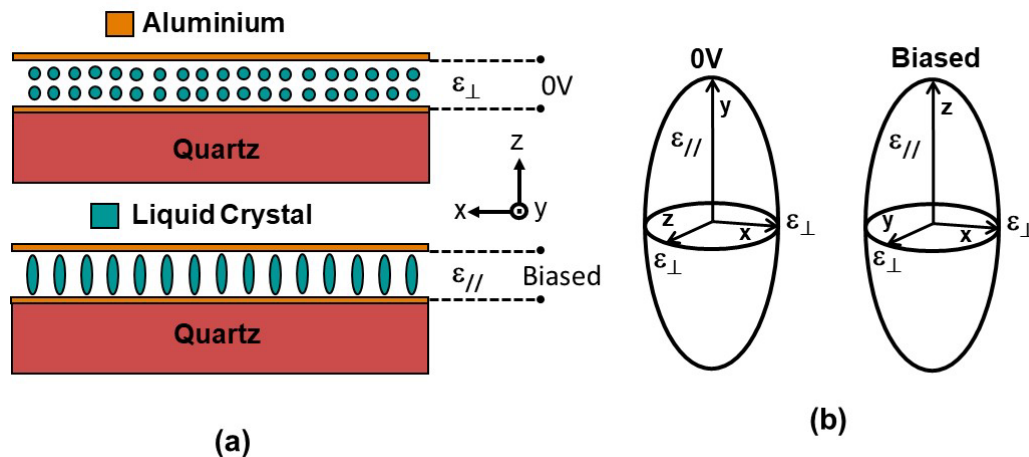
Fig. 1.10 (a) Schematic representation of the LC molecules in the 0 V and biased states. (b) LC permittivity tensor orientation in both states.

It is worth highlighting that a fundamental obstacle to translating LC-based tunable devices to lower frequencies such as microwaves and mmWave is the stark contrast between the LC-layer thickness (typically 2-10 µm) compared to the wavelength (in the centimeter and millimeter-scale). When the radiation propagates perpendicular to the LC layer, this results in weak wave-LC interaction, leading to the negligible tuning of the response when the LC is modulated. Moreover, the values of the LC permittivity along the ordinary and extraordinary axes are not drastically different; hence, a large LC thickness is necessary to obtain significant phase differences at the output. However, a large thickness of the LC would imply high external voltages to bias it properly, resulting in damage to the LC due to dielectric breakdown.

To overcome these limitations, resonant structures can be devised to obtain LC-based tunable devices at microwaves and millimeter waves [106], [113]. The underlying mechanism is based on the property that the phase (for the moment, it could be in transmission or reflection) near a resonance undergoes a fast variation, leading to a steep

slope in the frequency response. Intuitively, this fast variation can be interpreted as if the structure was made effectively larger. Hence, in the vicinity of the resonance, modulation of the LC permittivity by rotating the LC molecules from the ordinary to the extraordinary axis or vice versa can lead to a significant phase difference at the output. In [109], LC unit cells operating in the X-band were analyzed. A tunable dynamic phase range of 221° was achieved over a band of 220 MHz (fractional bandwidth of 2.2%) using a K15 nematic LC. A similar strategy was exploited in [114], where a printed RA antenna was simulated and manufactured in the X-band. There, a reconfigurable monopulse-shaped radiation pattern was demonstrated using a metallic microstrip patch sitting on a 500 μm cavity filled with a LC substrate by dynamically switching the permittivity of the LC substrate in the two halves of a RA aperture. In [115], a RA consisting of 52×54 identical cells composed of three parallel dipoles of different lengths placed on an LC substrate and operating in the F-band was proposed. This design exhibited an 8% fractional bandwidth with moderate losses (~7 dB), using a low-cost manufacturing process to produce antennas in frequencies from 60 to 500 GHz. In [116] a particular unit cell configuration composed of a microstrip patch was analyzed. Applying low-frequency AC bias voltages of 10 V, a 165° phase shift with a loss between 4.5 and 6.4 dB at 102 GHz and 130° with similar losses at 130 GHz was demonstrated.
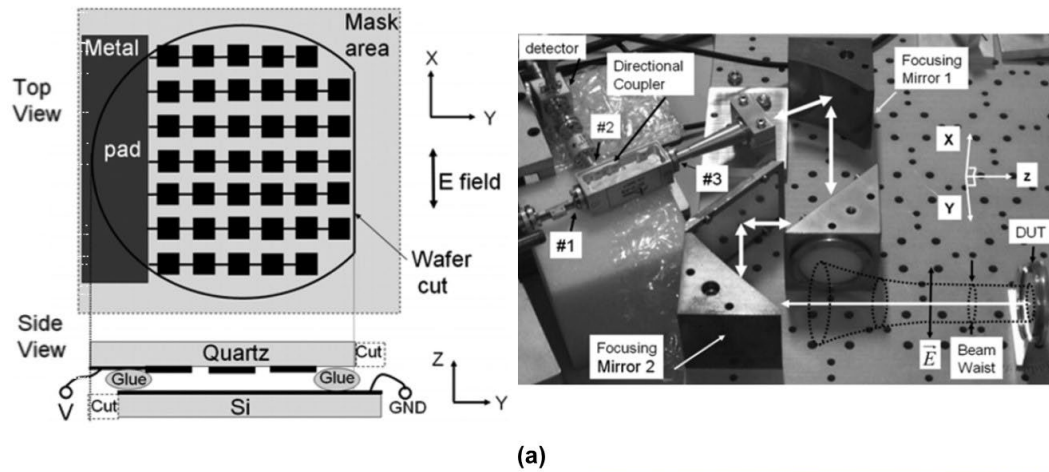
(a)
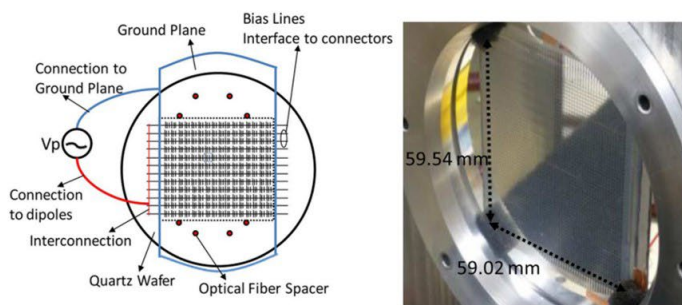
(b)
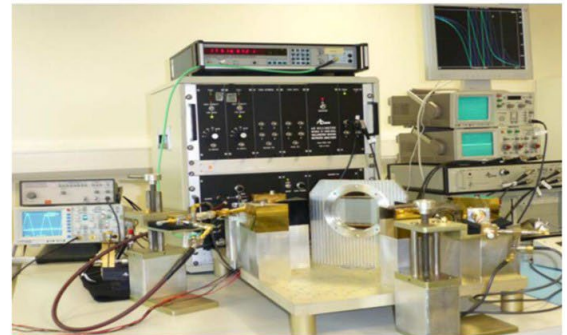
Fig. 1.11 (a) Reconfigurable mmWave RA cells with nematic LC, [116]. (b) LC reconfigurable RA at F-Band, [115].

1.7   Thesis outline and objectives

Based on all the previously exposed, the main goal in this thesis is the design and implementation of antennas based on the millimeter and sub-millimeter band, looking for compact configurations that can replace the bulky systems used today. To this end, technologies known as GW, metasurfaces, and metalenses (passive and active) are used to achieve the standards of the selected frequency bands.

23

In order to achieve these objectives, the thesis will be divided into two main blocks, due to the evolution in the handling of the aforementioned technologies:

- Compact antennas with circular polarization based on GW technology.
- Fully metallic inhomogeneous metalens antennas in GW technology.

The manuscript is organized as follows. In Chapter 2, three compact CP antennas using RGW technology are designed and analyzed. First, a new way to generate CP in GW technology based on two orthogonal feeder arms that excite a CP with a diamond-shaped slot on top is discussed. The basic design is then evolved gradually by introducing first a taper in the diamond-shaped slot and then inserting it in a circular groove, achieving a notable increase in the gain without deteriorating the other radiation parameters. The prototypes devised show that it is possible to design and manufacture CP antennas with large operation bandwidth (BW) and a moderate gain in GW technology in a novel, simple, and very compact technique, without implementing arrays and complex feeding networks. Following this line, an extension of the previous work is done, but now the main objective was to increase the gain. Specifically, a BE antenna with CP in RGW technology is designed and experimentally demonstrated.

Chapter 3 deals with an antenna operating at 60 GHz that combines the benefits of LL and GW technology. The metamaterial LL is synthesized using metallic pins that modulate the refractive index and produce a planar wavefront at the output direction. A carefully designed GGW horn antenna is used as excitation source by aligning its phase center with the focus of the metamaterial LL. A smooth transition to free space is implemented to improve the radiation pattern by introducing a flare at the output with a linear shape.

Chapter 4 proposes a dual-layer reflector geodesic lens antenna. In this case, a complementary LL with a virtual source is designed to illuminate a planar reflector. Thanks to the use of virtual source a compact footprint can be achieved. The antenna is realized with a dual-layer parallel plate, using the so-called pillbox setup [101], [117], [118]. The design procedure follows two steps. First, the feeding contour for the reflector is found using a ray-tracing analysis that evaluates the directivity, sidelobe level (SLL),

and scanning range. Then the lens is designed to fit this feeding contour. Finally, a full-wave simulation of the whole system is carried out for final verification.

Chapter 5 proposes an antenna lens system based on GGW technology and operating at 300 GHz. A flat hyperbolic lens with homogeneous index is proposed and an implementation based on metallic pins is performed. A GGW horn antenna is used to feed the lens placed in a PPW. The combination of both devices, the metalens, and the GGW antenna, leads to a good radiation performance opening new technological possibilities in the higher limit of mmWave.

Chapter 6 presents an active reflectarray based on LC. In this work, a reconfigurable RA with low losses and moderate bandwidth is implemented using a novel nematic LC composition. With an LC thickness of 40 µm, a metasurface is designed to operate in the 105-120 GHz frequency band. This investigation pursues two main goals: 1) to experimentally check prospects for using the developed LC composition in meta-devices; 2) to find an optimal RA configuration that combines fabrication simplicity and the ability to achieve the maximum phase shift while keeping the reflectance as high as possible.

Finally, Chapter 7 contains the general conclusions and future lines of the work. Some of these future lines are related to collateral aspects of the research lines presented in this thesis, and others are a continuation of them. Three appendices are included at the end of the manuscript to support and clarify the content of each chapter.

Chapter 2: Metallic Antennas at Millimeter Waves in Gap Waveguide Technology

2.1 Introduction

The communications systems at mmWave will provide globally available broadband service by converging mobile and satellite networks. High data-rate wireless links supporting such systems require high-gain antennas to compensate for the severe propagation losses at these frequency bands. CP is also a common specification to avoid an undesirable polarization mismatch in on-the-move communications, indoor systems with severe multipath effects as well as satellite systems prone to depolarization due to Faraday rotation in the ionosphere.

The main goal in this first part of the chapter is to lay the groundwork for developing and designing a feeding method for circular polarization antennas based on GW technology. Using this technology, the manufacturing complexity can be reduced compared to standard waveguides and the performance can be improved compared to devices made by additive manufacturing.

GW technology was conceptualized and developed by Prof. Per-Simon Kildal [119].It is founded on the concept of metamaterials and hard and soft surfaces. These are an evolution of corrugated metallic surfaces that had previously been used in the design of horn antennas to feed large reflectors [120], [121].

The working principle of GW technology is based on the use of two parallel plates, a PEC and a PMC, as well as a central ridge, strip, or a groove depending on the application. The PMC provides a high impedance surface opening a forbidden band around the frequency of resonance that prevents the propagation of the electromagnetic waves confining them within a predefined region. The wave is then effectively guided between the strip, or a groove and the PEC plate.

A PEC medium can be approximated by good electrical conductors. However, obtaining a PMC is not that simple, as this type of material does not exist naturally. Therefore, it must be emulated by AMCs [122] such as mushroom-like surfaces or a metallic bed of nails, which is the solution implemented in this thesis. In the same way as the traditional waveguide, the waves can be guided in the GW technology using a central metal ridge, strip, or simply a groove delimited by the AMC, as explained in section 1.3.

With regards to CP, the prototypes that will be shown in this chapter are based on the work presented in [123], where a novel way to generate CP in a single microstrip layer at 2.4 GHz was developed. CP was obtained by simply adjusting the feed system dimensions without modifying the microstrip radiator. This work developed mainly at the Department of Telecommunications and Telematics, ISPJAE, Havana, Cuba, can be applied to any regular polygon.

In this chapter, a similar design methodology is used to feed three different antenna slots at 60 GHz instead the microstrip patch presented in [123]. Three different upper plates are implemented, each one of them corresponding to different evolution stages of the antenna and with different radiation characteristics but sharing all of them the same feeding network.

2.2   Ridge Gap Waveguide Feeding Method

RGW is one of the main variants of GW technology. As explained before, two parallel plates, an upper smooth metal lid and a lower plate, consisting of a central metallic ridge

surrounded by PMC, are needed to guide the wave correctly. To this end, a bed of nails that provides a wide stopband is designed. Afterwards, a smooth transition to connect the input standard waveguide with the central ridge and from here guide the wave into the system is implemented. Finally, the method to generate CP is explained. It consists in introducing two orthogonal arms of different size at the end of the ridge (section 2.2.3).

2.2.1   Bed of nails design

The first step in the design of the antennas consist in finding an efficient WR-15 to RGW transition. This is a necessary step for the experimental characterization since the standard instrumentation at mmWave is based on metallic waveguides.
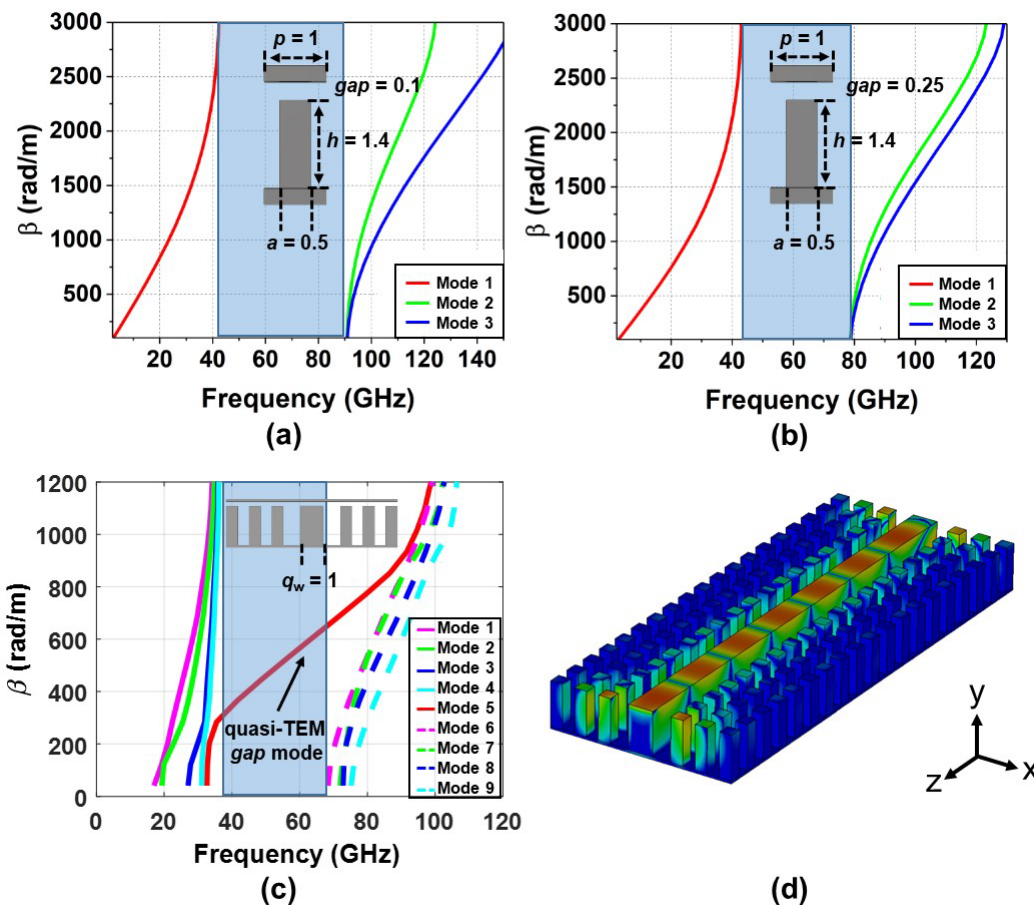
Fig. 2.1 Dispersion diagrams: (a) Periodic metallic pin media (p = 1, gap = 0.1, h = 1.4 and a = 0.5 mm). (b) Periodic metallic pin media (p = 1, gap = 0.25, h = 1.4 and a = 0.5 mm) (c) Finite structure consisting of row of pins with a central ridge of q_w = 1 mm (p = 1, gap = 0.25, h = 1.4 and a = 0.5 mm). (d) 3D plot of the vertical component of the E-field for the ridge gap waveguide, resonance at f_0 = 60 GHz.

The first step consists in designing the AMC structure, implemented using a periodic metallic pin medium. The theoretical explanation is widely developed in [16]-[18]. In this section, a similar procedure has been followed at higher frequencies. This artificial medium must be designed so that it presents a bandgap at the operation frequency. The eigenmode solver of CST Studio Suite® was employed to obtain the pin dimensions. The material employed in all the structures is aluminum due to its good conductivity in the operation band (σ_{Al} = 3.72×10^6 S/m), mechanical robustness, and compatibility with standard manufacturing techniques. After the optimization the dimensions of the pin array were: period p = 1 mm, high h = 1.5 mm and wide a = 0.5 mm, as shown in Fig. 2.1(a) inset. The gap between the upper plate and the pin controls the BW, as can be seen by comparing Fig. 2.1(a) and (b) where the gap has been slightly varied from 0.1 to 0.25 mm keeping the other parameters unchanged. A slight reduction of the BW is noticed when the gap is changed from 0.1 to 0.25 mm. Finally, a gap of 0.25 mm was selected because it matches with the operation bandwidth and is easier to obtain in the manufactured structure, keeping the constraint of having a gap below $\lambda_0/4$, as explained in section 1.3. Fig. 2.1(c) inset shows the dispersion diagram of a waveguide formed by three rows of pins with a central ridge of width q_w = 1 mm, separated from the upper lid by the air gap and infinitely periodic along the z-direction. A quasi- transverse electromagnetic (TEM) mode (solid red curve) is excited and propagates within the stopband, whereas all other higher-order modes are forced to cut-off by the boundary conditions imposed by the bed of nails, as shown in Fig. 2.1(d).

2.2.2 Transition from WR-15 to RGW

The next step is to design a transition between the standard waveguide (WR-15) and the RGW feeding network which will be used in the experimental analysis. In this case, inspiration was taken from [124] to implement it, wherein a similar transition was used in

the *Ku*-band. This design was carefully adapted to operate in the V-band, and the final result is shown in Fig. 2.2(a).
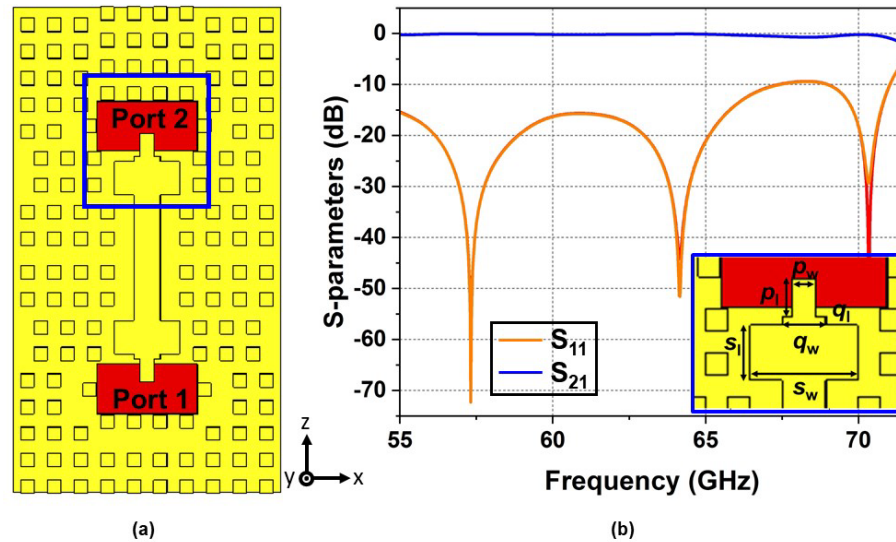
Fig. 2.2 (a) Schematic of back-to-back evaluation setup (b) Simulated reflection and transmission coefficients of the feeding system using a back-to-back evaluation. Inset, transition steps.

It is a stepped impedance matching network composed of three subsections (see more details in Fig 2.2(b) inset): the first part is the narrowest, with width labeled as p_w, and provides coupling from the fundamental WR-15 waveguide mode and the fundamental RGW mode. The second step is the shortest of all, with dimensions $q_w \times q_l$, and acts as a smooth stepped transition. The third stage is a wide and long block of dimensions $s_w \times s_l$ responsible for the final coupling of the wave to the ridge, which feeds the upper aperture. All the dimensions of the designed transition are presented in Table 2.1. Fig. 2.2(a) shows a back-to-back setup (i.e. two identical transitions connected back-to-back) to check the impedance matching of the transition. Two identical ports connected to the input/output WR 15 waveguides to feed the structure from the bottom side (Port 1 and 2) and from them the S-parameters are obtained. As shown in Fig. 2.2(b) the transition has a good impedance matching within the considered band, with a reflection coefficient below −10 dB and negligible insertion loss.

Table 2.1: Dimensions of the WR 15 to RGW transition

Parameter	Description	Values (mm/λ_0^*)
p_w	First step width	0.54/0.11
p_l	First step length	0.83/0.18
q_w	Second step width	0.23/0.05
q_l	Second step length	0.2/0.04
s_w	Third step width	2.45/0.52
s_l	Third step length	1.05/0.22

$^*\lambda_0$ = 4.72 mm at 63.5 GHz

2.2.3 Circular polarization generation using asymmetric arms

The next step is to design the stage for the generation of CP polarization. In this thesis the strategy followed is based on the feeding technique proposed in [123] which is adapted to operate at mmWave with RGW technology. Fig. 2.3(a) shows the configuration designed, that combined two orthogonal arms of different lengths and a diamond square slot on the top layer. First, the central ridge is split into two arms with a length difference of 1.13 mm, which corresponds approximately to $\lambda_0/4$, where λ_0 = 4.72 mm is the wavelength at the operation frequency, f_0 = 63.5 GHz. This guarantees that the phase difference between both arms is close to 90°, as demonstrated in Fig. 2.3(b), which shows that the electric field distribution in both arms is nearly in quadrature: the maximum value in one arm corresponds to a minimum (in magnitude) in the other. A diamond-shape slot aperture is carved out in the upper lid and is placed above the arms, with sides parallel to said arms. This is the basic D-Antenna that will be studied in previous sections. At the

31

operation frequency, the surface current excited on the upper plate has a clear spiral pattern, as shown in Fig. 2.3(c), corresponding to a CP. As the phase increases, the currents rotate clockwise (attending to the typical definition of handedness which establishes the viewpoint of the emitter), indicating that the antenna supports right-handed circular polarization (RHCP). It is noteworthy that with such a simple feeding system, it is possible to generate CP in a compact footprint, in contrast with the typical approach based on an array of antennas, which increases the complexity as well as the footprint area [35], [36], [125].
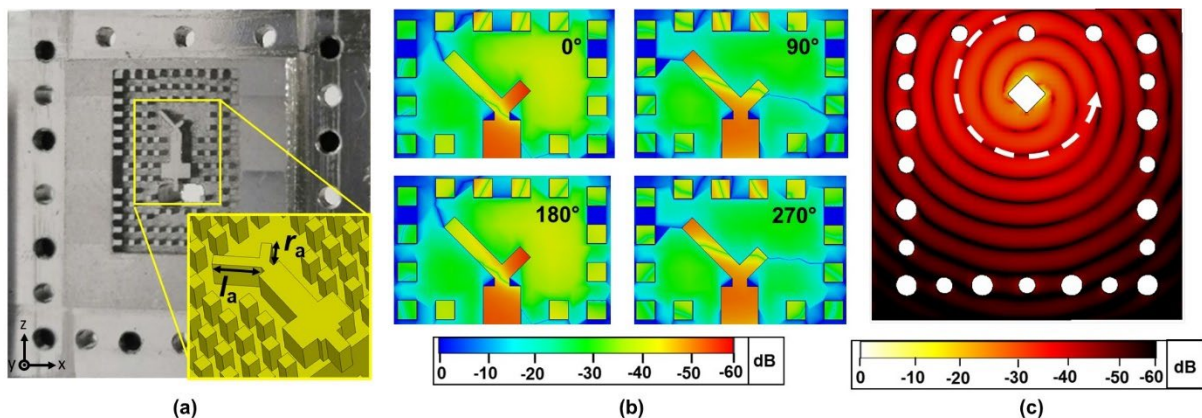
Fig. 2.3 (a) Photographs of the Diamond Antenna feeding configuration showing both arms with different lengths (left arm (l_a = 1.77mm) and right arm (r_a = 0.64 mm)) at the end of the ridge. (b) Electric field magnitude normalized at 63.5 GHz at four different snapshots, showing that the arms are operating in quadrature. (c) Top view of the surface current magnitude on the top plate (D antenna) at 63.5 GHz.

2.3 Simulation and Experimental Results

The previous structure is the basic setup to generate CP. In the following different realizations of antennas are studied in detail, all of them based on a similar setup and modifying only the shape of the upper slot with the aim to increase the directivity.

2.3.1   Diamond Antenna Evolution

The basic design is a diamond-shaped (D) slot antenna on top of the feeding network, see Fig. 2.4(a). The first evolution from this initial prototype involves introducing a taper in the upper face, following a strategy similar to horn antennas but in a much more compact profile, leading to the diamond-horn (DH) antenna depicted in Fig. 2.4(b). In the last evolution step, a circular groove concentric to the DH slot is carved on the top plate to increase the gain. This last design, shown in Fig. 2.4(c), is called a diamond-horn groove (DHG) antenna. The structures are fed from the bottom employing a WR-15 standard waveguide to make it compatible with standard measurement systems based on vector network analyzers; this will be analyzed in next sections.

(a)   (b)   (c)
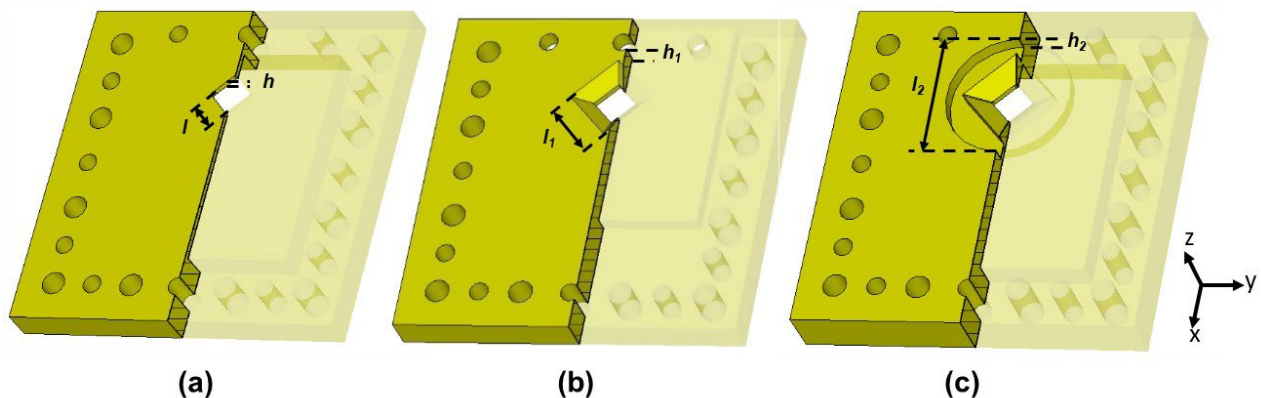
Fig. 2.4 Schematic of (a) D antenna top view with a slot length of l = 2.65 mm and thickness h = 0.5 mm. (b) DH antenna top view where l_1 = 5.08 mm and h_1 = 1.45 mm and the rest of dimensions are as before. (c) DHG antenna top view have a groove diameter l_2 = 10.93 mm and thickness h_2 = 1.28, and the rest of dimensions as the DH antenna.

The basic design (D antenna) is used to assess the performance of the CP generation and is the starting point towards evolved antenna designs engineered to increase the gain without degrading other radiation characteristics. This section explains the evolution from the primary D antenna to the more complex diamond Horn Groove antenna (DHG

antenna) design. The antenna performances are evaluated in terms of the reflection coefficient, AR, broadside gain, and polarization purity.

Fig. 2.5 shows the simulation results for the three structures considered, considered to entire setup including the transition from WR-15 to RGW showing in section 2.2.1. First, it is noted that all the antennas are matched from 59 to 69 GHz approximately, with the criterion of having a reflection coefficient magnitude below −10 dB, see Fig. 2.5(a). The best case happens for the DHG antenna (blue curve), where a broad matching BW of 9.6 GHz (15.1%) from 59.3 to 68.9 GHz is achieved. The other antennas have a similar performance with a BW of 9.22 GHz (14.5%) from 58.9 to 68.2 GHz in the case of the D antenna and 9.28 GHz (14.6%) from 59.1 to 68.4 GHz for the DH antenna. In the reflection coefficient spectrum, one can notice two main resonances, one at 63.5 and another one at 65.5 GHz (D antenna, red curve). These resonance frequencies cannot be ascribed to any isolated arm, demonstrating clearly that the mechanism is based on a close interaction between them. Interestingly, what one can identify are two orthogonal resonances in the slot, each one of them corresponding to the aforementioned frequencies. Although a further analysis should be done to grasp all the details behind the CP generation in the setup implemented, the interpretation based on a length difference between arms of $\lambda_0/4$ seems sufficient to explain the basic principles. Note that the minimum axial ratio (AR) happens exactly in the middle of both resonance frequencies. Although these results correspond to the D antenna (which is the simplest one), a similar analysis holds for the other designs.

(a)   (b)   (c)
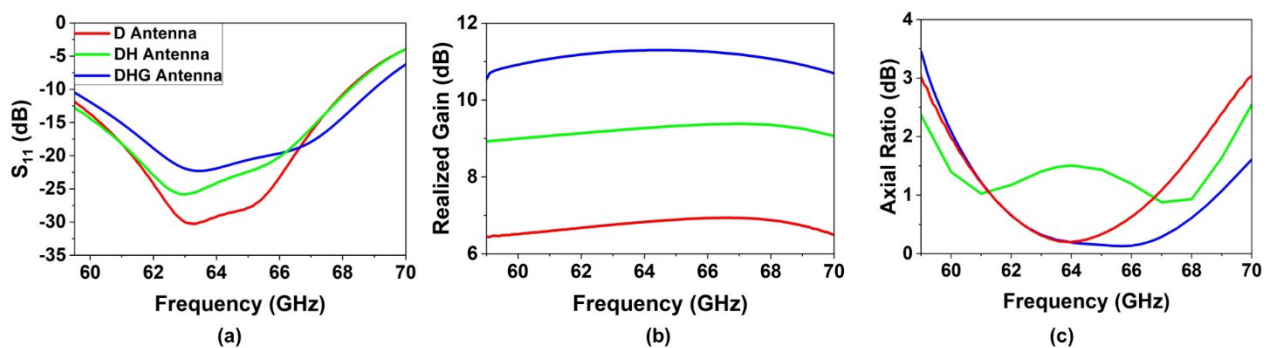
Fig. 2.5 Simulated results of the three designed antennas. (a) Reflection coefficient magnitude. (b) Realized gain at broadside (ϕ = 0° and θ = 0°). (c) AR.

The evolution from the basic D antenna to the more complex DHG antenna was done in order to increase the gain of the design, keeping the same footprint to ensure a compact structure. The D prototype [Fig. 2.4(a)] has a relatively low gain with a maximum around 7 dB, as corresponds to a small slot antenna, see red curve in Fig. 2.5(b). By introducing a taper in the diamond-shaped slot the gain can be increased to 9 dB, see the green curve in Fig. 2.5(b). This tapering is inspired by the operation principle of horn antennas, but in this case with a very low profile, see Fig. 2.4(b). To further increase the gain, a concentric circular groove was introduced around the DH slot, see Fig. 2.4(c). The groove operation can be interpreted as a cavity that boosts the radiation in the broadside direction. In addition, the difference between the groove radius and the edge of the inner diamond slot is approximately λ_0 so it interferes in phase with the slot at broadside, enhancing the gain in that direction. This latter design (blue curve) has a peak gain of more than 11 dB at 64.5 GHz and in the whole operation band is above 10 dB.

Another important figure of merit to evaluate the performance and delimit properly the operation BW of CP antennas is the AR. Fig. 2.5(c) shows the simulated AR curves for all the antennas considered. By analyzing the results, it can be concluded that all the designed antennas generate CP of high purity with low values of AR in the considered frequency span, especially the basic D antenna and the most evolved DHG antenna. The CP BW of the antennas is obtained by applying the criterion of having AR < 3 dB. From the curves it is seen that the DH antenna achieves a BW of 9.9 GHz (from 59 to 68.9 GHz), which means a fractional BW of 15.7%. The D and DHG antennas have a BW of 10.7 GHz (from 59.3 to 70 GHz), or equivalently a fractional BW of 16.6%. The excellent performance of the DHG antenna is remarkable, with AR < 1.5 dB within a broad BW from 60.7 to 70 GHz. It is seen in that figure that the DHG antenna generates CP even beyond 70 GHz. However, the impedance matching is only good up to 68.9 GHz, restricting the practical operation BW to this frequency.

2.3.2   Diamond antenna experimental results

To corroborate experimentally the previous simulation results, both the D and DHG antennas were manufactured by means of a computer numerical control (CNC) milling machine. The DH antenna was not considered because, as was found in the previous analysis, it has the worst polarization purity of all the antennas. Additionally, it is an intermediate step between both the D and DHG designs and therefore it is less interesting from a practical point of view.

The first analysis corresponds to the D antenna, a basic radiant slot placed on the top metallic plate, see Fig. 2.6. In the following, simulation and experimental results are analyzed together for the sake of clarity. The far-field measurements were performed in the anechoic chamber of the Antennas Group of the Public University of Navarra. Measurements using an E8361C (Agilent Technologies) PNA network analyzer in the frequency range from 59 to 70 GHz with a step of 50 MHz. The radiation patterns were measured by placing a standard horn antenna with linear polarization (Mi-Wave 261) at a distance of 1500 mm (the far-field distance at the operation frequency is at 720 mm) from the antenna under test (AUT). In each of these positions, the AUT was swept in elevation from −90° to 90° with a step of 0.5°. As the test antenna (Mi-Wave 261) has linear polarization, in each measurement it was rotated in plane at orthogonal positions and from the recorded curves, the CP characteristics of the AUT were obtained.
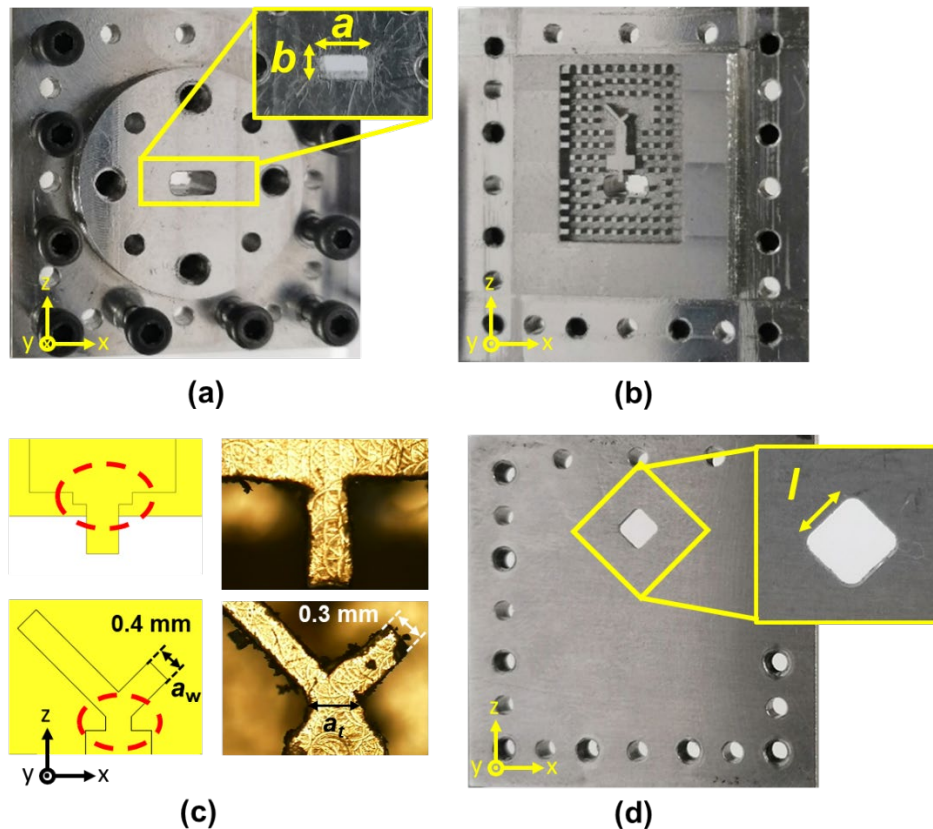
Fig. 2.6 Photographs showing a view of (a) bottom WR-15 waveguide flange where a = 3.18 mm and b = 1.90 mm (b) Feeding system. (c) Design (left) and manufactured prototype (right) where fabrication is highlighted (the images are not in the same scale) (d) D antenna top view showing the length of the slot (l = 2.65 mm).

The entire structure was checked in detail to analyze the possible manufacturing issues. Fig. 2.6(a) and inset show a bottom view the feeding network, it can be appreciated that the corners have been rounded due to the drilling process (as this is typical in CNC machining, rounded corners were considered in the simulation study). A top view feeding network is presented in Fig 2.6(b). In general, there is a good agreement between the designed and manufactured structure, but some imperfections are detected upon close inspection. Fig 2.6(c) shows the two more evident manufacturing errors (design on the left and manufactured structure on the right):

- Elimination the short transition to couple the wave from WR-15 to metal ridge.

- Elimination of the narrow transition between the ridge and the arms.
- In addition, the arms width differs considerably, from 0.4 mm (design) to 0.3 mm (manufactured prototype).

Finally, Fig. 2.6(d) presents the top plate, where the slot, the alignment and screw holes have good agreement with the simulation design.

The antenna performance is evaluated in terms of the reflection coefficient, AR, broadside gain, and polarization purity, see results in Fig. 2.7. A new simulation was done considering the manufactured errors. The reflection coefficient has good impedance matching, with magnitude below −10 dB from 60.5 to 69.3 GHz leading to a BW of 8.8 GHz (13.9%), see Fig. 2.7(a). Although these results correspond to the D antenna (which is the simplest one), a similar analysis holds for the other designs. The experimental results (solid red curve) show a clear disagreement with the initial simulation results (solid blue curve), mainly a frequency shift and a reduction of the resonance depth. When manufacturing errors are considered (dashed red curve) the agreement is much better. Table 2.2 shows the parameters with the highest deviation in the manufactured device.

Table 2.2: Manufacturing errors

Parameters	Design (mm)	Manufactured device (mm)	Error (%)
q_w	0.23	0	100
q_l	0.2	0	100
a_w (arm width)	0.4	0.3	75
a_t (arms transition)	0.4	0.6	33.3
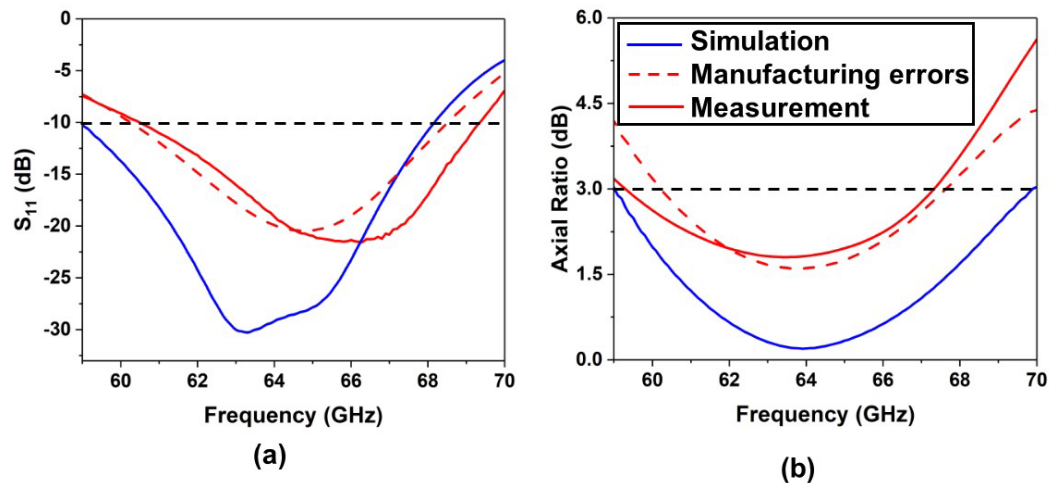
Fig. 2.7 Simulated (solid blue curves), manufacturing errors (dashed red curve), and measurements (solid red curves) results of the D antenna. (a) Reflection coefficient magnitude (b) Axial ratio.

An important figure of merit to evaluate the performance and delimit properly the operation BW of CP antennas is the AR. Fig. 2.7(b) shows the simulated AR curves for all simulation and measurement results. The designed antenna generates CP with low values of AR in the considered frequency span. The CP BW of the antennas is obtained by applying the criterion of having AR < 3 dB. D antenna has a BW of 8.3 GHz (from 59.2 to 67.4 GHz) or, equivalently, a fractional BW of 13.1% in experimental results. Note that the minimum AR happens exactly in the middle of both resonance frequencies. Again, both curves (simulated and measured) have a disagreement due to the manufacture errors in the feeding network (Fig. 2.6(c)) and the agreement is improved when these are considered in the simulation.

The broadband gain was obtained by applying the gain transfer (or gain comparison) method with arbitrary polarization [126], [127]. First, two identical calibrated standard horn antennas (Mi-Wave 261) of known gain were carefully aligned and the received power within the frequencies of interest was recorded. Then, one of the standard horn antennas was replaced by the AUT. In this way, the gain is easily obtained, as shown in the solid line of Fig. 2.8(a). The D antenna reaches a maximum of 5.49 dB at 66.8 GHz in the experiment. There is a strong deviation with the simulation results which could have

several explanations: misalignment between receiver and transmitter, high difference gain in the antennas used to the comparison method and AUT, and losses attributed to roughness of the aluminum. In addition, the comparison method gives a tolerance in the measurements around ±0.5 dB.
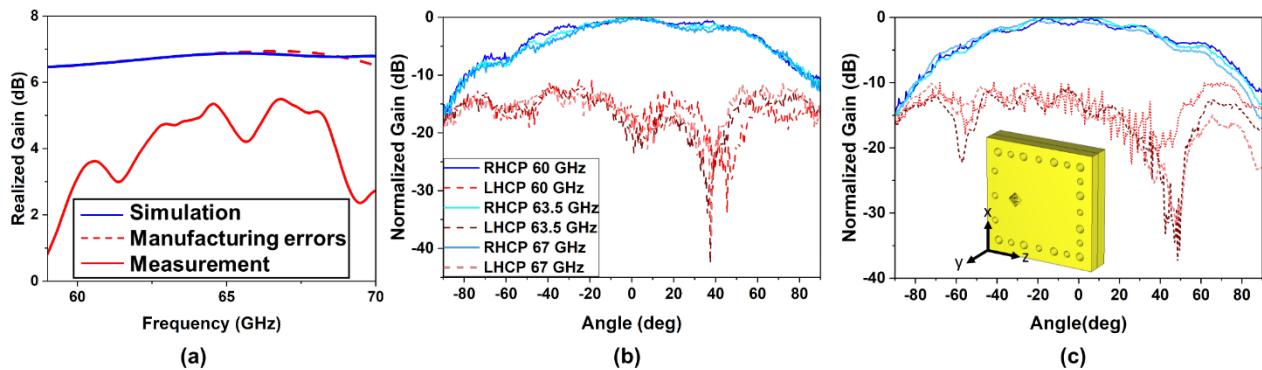
Fig. 2.8 (a) Simulated (solid blue curves), manufacturing errors (dashed red curve), and measurements (solid red curves) results of realized gain at broadside ($\varphi = 0°$ and $\theta = 0°$). Co-polarized and cross-polarized measured radiation patterns at several selected frequencies. (b) $\varphi = 0°$, *xy* plane and (b) $\varphi = 90°$, at *yz* plane. Inset of (c): scheme of the antenna with the coordinate axes. The angle swept in all cases is the elevation, θ.

Finally, the experimental radiation patterns are presented. The elevation angle, θ, was varied from −90° to 90° with a step of 0.5° and the frequency was swept from 55 to 70 GHz with a step of 50 MHz. From all the evaluated frequency points, several representative frequencies were selected and represented. The D antenna presents more than 15 dB of cross-polarization isolation in both planes, as shown in Fig. 2.8(b) and (c). In addition, the polarization rejection corroborates that the antenna has a good RHCP polarization purity.

2.3.3   Diamond Horn Groove Antenna Experimental Results

As was explained detail in section 2.3.1, the basic design (D antenna) is used to evaluate the strategy followed to generate CP and is the starting point towards antennas with higher gain without degrading other radiation characteristics.

To corroborate the improvements of the new designs experimentally, the DHG antenna was manufactured using the same method. Photographs of the fabricated prototype are shown in Fig. 2.9(a). The measurement setup is the same as the previous D antenna, since the operation band is the same. Manufacturing errors are also considered here in a new simulation study (red dashed curve). A BW of 9 GHz is determined from the reflection coefficient magnitude shown in Fig. 2.9(b), which represents 14.2% of the center frequency, in good agreement with the simulation results. The broadband gain reaches a maximum of 11.1 dB at 67.3 GHz, Fig. 2.9(c). Note that the gain is almost doubled with respect to the initial D antenna.

Applying the same criterion of AR < 3 dB, the BW in this parameter was improved as well. In this case, the CP BW extends beyond the considered frequency range (note that the AR is below 2 dB in the plot Fig. 2.9(d)) but the antenna is matched only from 60.3 to 69.6 GHz as mentioned above. Thus, the practical operation BW is restricted by impedance matching and reaches a value of 14.5%. These results are in good agreement with the numerical calculations. The experimental radiation patterns are represented at three different frequencies 60, 65 and 70 GHz, Fig. 2.9(e) and (f). The cross-polarization isolation in all frequencies reaches values of more than 15 dB improving the results of the D antenna.
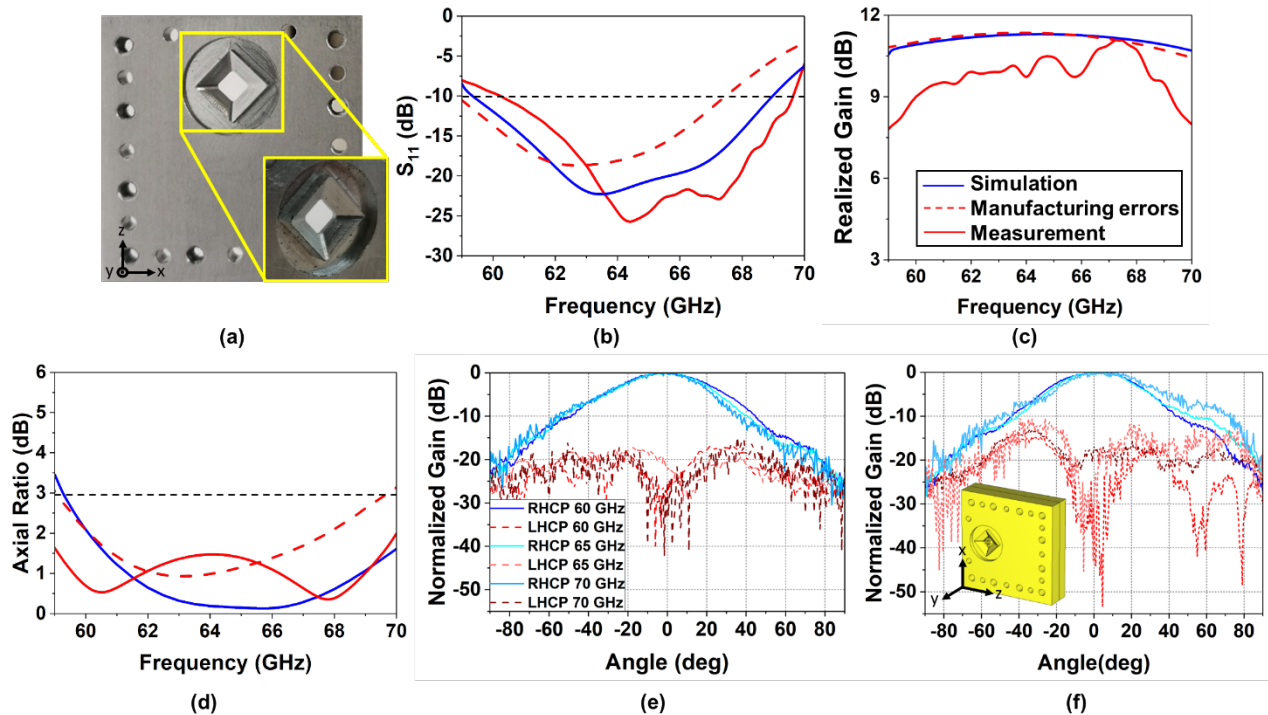
Fig. 2.9 (a) Photographs showing the fabricated DHG antenna top view. (b) Simulated (dashed curves) and experimental (solid curves) results. (c) Realized gain at broadside ($\varphi = 0°$ and $\theta = 0°$). (d) Axial Ratio. (e) Co-polar (solid) and cross-polar (dashed measured radiation patterns at several selected frequencies and $\varphi = 0°$ (*xy* plane). (f) Idem at $\varphi = 90°$ (*yz* plane). (Inset): scheme of the antenna with the coordinate axes. The angle swept in all cases is the elevation, θ.

Finally, a comparison between the D antenna and the DHG antenna is presented to evaluate the improvements achieved with this final prototype, see Fig. 2.10. First, the insertion of a taper in the diamond-shaped slot and the concentric groove to provide a smooth transition to free space increases the gain (from 5.5 dB to 11.1 dB). Furthermore, combining the horn profile with groove increases the gain, AR, BW, and purity considerably (from 7.3 GHz to 11 GHz of BW). Finally, with the same total size (30×30 mm) in both manufacturing structures, the practical operation BW in the best case (DHG antenna) is around 14.5% which represents a large improvement compared to the initial D antenna design.

42
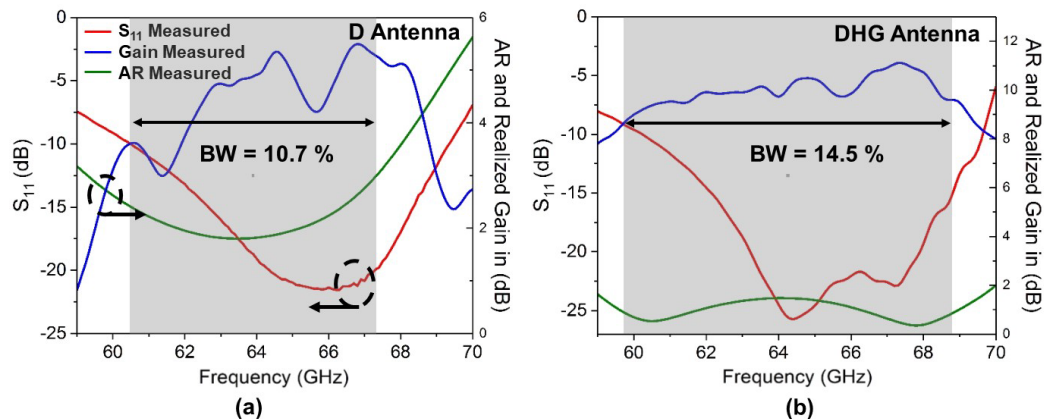
Fig. 2.10 Experimental results including reflection coefficient magnitude (red curve), realized gain at broadside φ = 0° and θ = 0° (blue curve) and axial ratio (green curve). (a) D antenna (b) DHG antenna.

2.4 Bull's Eye antenna

Up to this point several GW antennas using a simple and novel feeding network to obtain CP with high purity have been presented. In addition, the area around the diamond slot was modified to increase the directivity in the system without deteriorating other radiation characteristics. Nevertheless, there is a large area on the top plate that is not used in any of the designs, and hardly contributes in the radiation of the system. Therefore, in this section an alternative prototype is studied to optimize the top surface and improve the directivity of the system. To solve it, a good alternative are the BE antennas, a special part of the larger family of periodic leaky wave antennas.

2.4.1 Narrowband Feeding Network Design

A final evolution of the D antenna is proposed in this section by exploiting LWA concepts with the aim to make an optimal use of the upper surface. Beyond that, it is evident that the BE geometry (discussed in section 1.4) is compatible with CP, as the grooves usually have revolution symmetry. However, most BE antennas reported to date have linear polarization due to the limitation imposed by the primary source, which is usually a rectangular central slot. Therefore, using the method developed in previous

43

designs (D and DHG antennas) it is possible to get CP using a BE structure. Therefore, in this section a high-gain antenna with CP is demonstrated by combining the ideas of the diamond slot antenna with a BE pattern covering the top metallic plane maximally. In this way, three essential concepts are merged: generating CP in a simple way, using GW technology, and demonstrating a high gain in a single antenna without using antenna arrays, which require a complex feeding network.

Table 2.3 Design Parameters

Parameter	Description	Values (mm/λ_0^*)
a	WR-15 width	3.18 / 0.62
b	WR-15 height	1.90 / 0.37
s	Step height	0.38 / 0.07
p	Step length	1.05 / 0.20
w	Step width	1.00 / 0.20
q	Ridge length	2.4/0.47
l_a	Left arm length	1.28 / 0.25
r_a	Right arm length	0.78 / 0.15

$^*\lambda_0$ = 5.1 mm at 58.5 GHz.

Applying the knowledge obtained in the previous antennas, the first step is to design a WR-15 to RGW transition necessary for compatibility with our standard experimental setup. Intuitively, the same transition proposed in D and DHG antennas could be used because the frequency band is the same. However, BE antennas are narrow band and the feeding network presented was wideband. In addition, a new alternative was

44

considered to avoid manufacturing errors. Therefore, a narrow band matching section is proposed because it is simpler, easier to fabricate, and fits well with the requirements of BE antennas. Fig. 2.11(a) shows the WR-15 waveguide connection from the bottom plate with a slot of dimension $a \times b$. The transition consists of a simple step of height s and length p, as shown in the top view of the feeding network in Fig. 2.11(b), with the dimensions outlined in Table 2.3. As demonstrated in the back-to-back simulation results of Fig. 2.11(c), its performance is satisfactory. Furthermore, within the considered BW, the transition has an excellent matching with a reflection coefficient below −10 dB and low insertion loss.

(a) **(b)** **(c)**
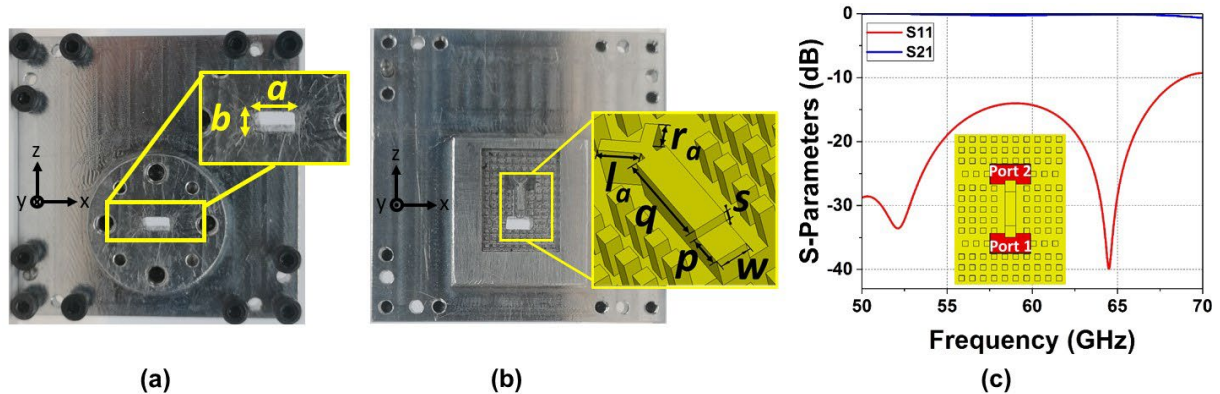
Fig. 2.11 (a) Photographs and schematics showing the fabricated BE antenna. (a) Bottom view of WR-15 waveguide connection. (b) Feeding system. (c) Simulated reflection and transmission coefficients of the feeding system using a back-to-back evaluation.

2.4.2   Bull's Eye Antenna Performances

As explained in detail in section 2.2.1, the CP is generated by the length difference between the two orthogonal arms at the end of the ridge, r_a and l_a. In the previous antennas, the difference between the left and right arms was nearly $\lambda_0/4$, giving rise to a phase difference of 90º and therefore to a CP at the output. However, in the present case the length difference between both arms is 0.5 mm which is only $\lambda_0/10$ (l_a = 1.28 mm and r_a = 0.78 mm). To ascertain the reason behind this disagreement, it is observed that in the present antenna the thickness of the upper plate and hence the thickness of the

diamond slot must be increased to carve the periodic grooves, with a non-negligible impact on the final result. To analyze it, a parametric study varying the plate thickness *h* was done while keeping a constant difference between arms of $\lambda_0/4$, checking the influence on the AR (note that, without loss of generality, in this study the grooves were removed for simplicity). It is evident in Fig. 2.12(a) that for small values of *h* (< 0.9 mm) the structure behaves satisfactorily with low AR (AR < 3 dB) in good agreement with the results of the D antenna, but when *h* increases beyond 0.9 mm the AR degrades rapidly. A similar study was done fixing the arm's length difference to $\lambda_0/10$; see Fig. 2.12(b). Now the best AR is achieved with *h* = 1.5 mm (0.3 λ_0). These results suggest that the slot thickness has some non-trivial effect on the phase difference achieved between orthogonal linear components.
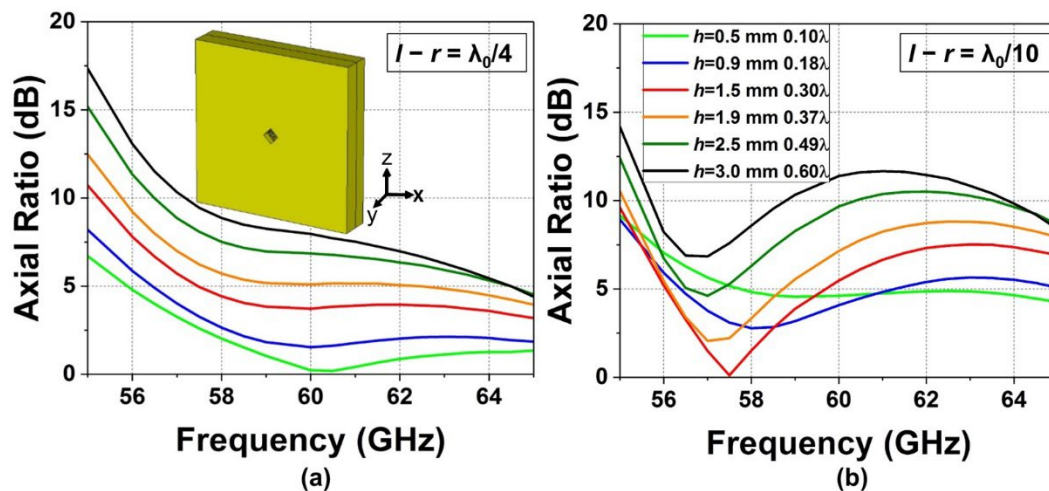
Fig. 2.12 Numerical study of the AR magnitude as the height of the top metallic plate *h* is varied between 0.5 and 3 mm (corrugations have been removed for simplicity). (a) Arm's length difference equal to $\lambda_0/4$. (b) Arm's length difference equal to $\lambda_0/10$.

Once the wave is coupled through the slot [of side $c \approx \lambda_0/2$ to guarantee good radiation at the operation frequency, Fig. 2.13(a)], it reaches the top plate and excites the BE structure, as shown in the surface current representation of Fig. 2.13(b). The physical mechanism of BE antennas is based on LW excitation and has been extensively described in the past [128]. In the present case, wide grooves were implemented, as they

lead to higher gain values as explained in detail in [47], [129]. The grooves support a resonance at the operation frequency [Fig. 2.13(b) and inset)], contributing to the enhancement of gain at broadside. It is also clear that the currents follow a circular shape describing a RHCP pattern.

The previously discussed BE antenna was manufactured and measured, using CNC milling machining and aluminum as in the previous designs, see Fig. 2.13(a). The experimental characterization was done again in the anechoic chamber of Public University of Navarra. This time the frequency span extended from 55 to 65 GHz discretized in steps of 50 MHz due to the narrowband behavior of the BE. As shown in the solid red curve of Fig. 2.13(c), good matching is obtained in all the considered BW with $S_{11} < -10$ dB from 54.3 to 63.7 GHz, which represents a fractional BW of 16.2%, in good agreement with the simulation results (dashed red curve).

(a)   (b)   (c)
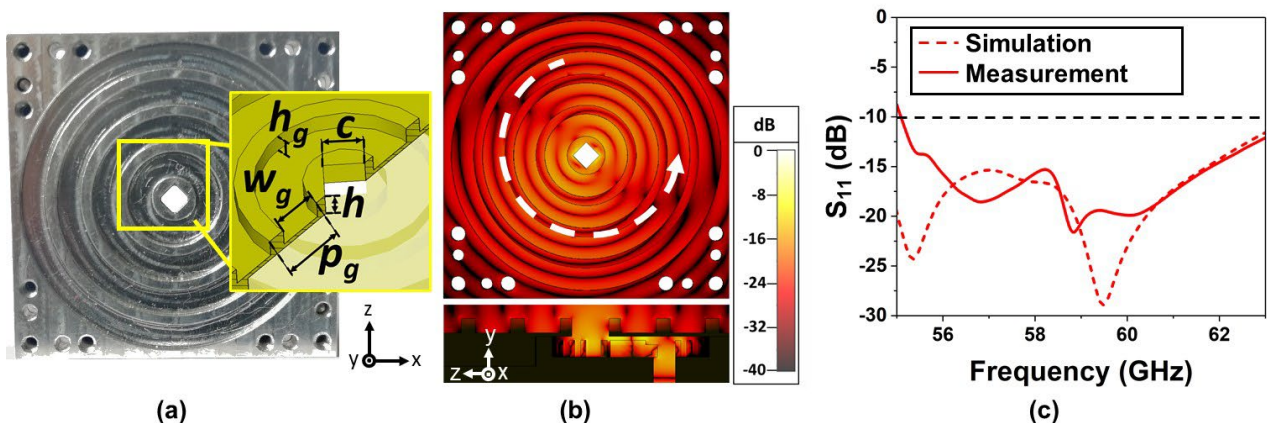
Fig. 2.13 (a) Top view of concentric periodic corrugations around the diamond-shaped slot. (Insets) Detailed views of each case h_g = 1.28, p_g = 4.36, w_g = 3.13, c = 2.65 and h = 1.62 mm. (b) Upper view of the surface current magnitude on the BE antenna at 58.5 GHz. (Inset) Contribution of each corrugation. (c) Simulated (dashed curves) and experimental (solid curves) results of the BE antenna.

The gain, AR and radiation patterns of the antenna were measured by following the method presented in section 2.3.2. Two different measurements were taken at each point by rotating the horn antenna (Mi-Wave 261) in two orthogonal positions. This is required because the test antenna has linear polarization and both orthogonal components are

needed to retrieve the CP response in the post-processing, which is based on the method described in [127]. The experimental AR is plotted in the solid blue curve of Fig. 2.14(a). Taking as a criterion that the wave has CP when the AR is below 3 dB, is found that the CP BW goes from 57.7 to 61.4 GHz, which represents a fractional BW of 6.3%. The minimum value (0.59 dB) is around 60 GHz. In the simulation, the CP BW goes from 56.7 to 58.8 GHz with a fractional BW of 3.6%, see dashed blue curve in Fig. 2.14(a), and a minimum AR of 1 dB is obtained at 58 GHz.

The measured gain (Fig. 2.14(a) red solid curve) was obtained applying the gain transfer (or gain comparison) method particularized to antennas with arbitrary polarization [126], [127]. In fair agreement with the simulation results (dashed red curve) the measured gain (solid red curve) reaches a maximum value of 18.4 dB at 58.5 GHz (which is the frequency of minimum AR) and decays away from the operation frequency, as typically happens in BE antennas. The aperture efficiency is approximately 9%, above the typical value of BE antennas.
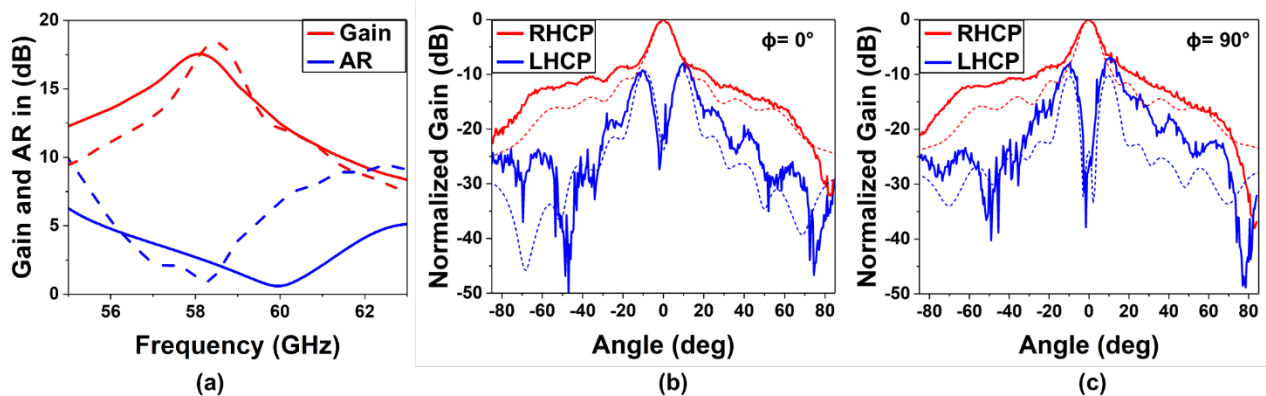
Fig. 2.14 Simulated (dashed curves) and experimental (solid curves) results of the BE antenna.
(a) Realized gain at broadside - $\varphi = 0°$ and $\theta = 0°$ - (red curve) and AR (blue curve). Co-polarized and cross-polarized radiation pattern at 58.1 GHz, (b) $\varphi = 0°$, (x-y plane) (c) $\varphi = 90°$, (y-z plane). The coordinate axes are the same in all figures and are shown in the Fig. 2.12(a)

Finally, Fig. 2.14(b) and (c) show the co-polarized and cross-polarized radiation patterns at 58.1 GHz, analyzed in two different planes: Fig. 2.14(b) *φ* = 0° (*x-y* plane); and Fig. 2.14(c) *φ* = 90° (*y-z* plane). The experimental results show an excellent polarization isolation of more than 30 dB at broadside, a main lobe of beamwidth equal to 11º and a small side lobe level of −9.7 dB in both cutting planes, in good agreement with the simulation results. These results improve those of the previous DHG antenna thanks to the addition of the BE structure, which optimizes the radiation on the top plane.

2.5   Comparison Between Different Gap Waveguide Antennas

In order to validate the behavior of the antennas manufactured in this chapter, a table comparing the main parameters of these and other designs found in the literature is presented. Note that most of the designs included in the table correspond to antenna arrays, which are comparatively more complex than our antennas based on a single radiating element and a simple feeding network.

Table 2.4: Comparison Between Different mmWave Antennas

Ref	Number of Elements	Fractional BW (Total BW)*	Fractional BW (Total BW)+	Peak Gain (GBW)#
[125]	16 × 16	14% (57 - 66)	5.0% (59-62)	32.3 (96.9)
[130]	4 × 4	14.1 % (56 – 65)	21.1% (55-68)	19.5 (253.5)
[131]	2 × 2	18% (56 - 67)	16.7% (56–66.2)	14.6 148.9
D	1 × 1	14.2 % (60.5-69.3)	11.5% (59.9-67.2)	5.49 (102.8)
DHG	1 × 1	14.7 % (60.3-69.6)	17.3% (60-71)	11.12 (122.3)
BE	1 × 1	16.2 % (54.3 – 63.7)	6.3% (57.7 - 61.4)	18.4 (68.0)

*Defined as S11 < −10 dB. Total BW is in GHz

+Defined as AR < 3 dB. Total BW is in GHz

#Peak Gain is in dB. For the gain-bandwidth product (GBW) calculation, the BW is defined as AR < 3 dB

Compared with previous designs, the antennas proposed in this thesis have a better impedance and CP BW. The designs have a unique radiating element; hence, they are compact and easy to design, in contrast with other approaches based on arrays. Although the gain is below some of the designs found in the literature, their small dimensions and high BW make the D and DHG antennas good candidates to be used in V-band. In addition, the BE antenna has, in general, good radiation characteristics. It has a moderate gain value (18.4 dB), similar to antenna arrays. As typically happens in BE antennas, the operation bandwidth (6%, the AR BW taken here as it is the interesting one for applications) is narrow, impacting the gain-bandwidth product, although there are other examples in the Table 2.4 in which it is even narrower. Thus, from this comparison, it can be said that the designed BE antenna can be a good choice for moderate gain and narrowband applications at millimeter-waves. Compared with similar antennas, the designed devices are good alternatives in a fully metallic setup that can have different uses, covering applications form narrow to broad bandwidths at V-band.

2.6 Conclusions

In this chapter, several antennas with CP operating in the V-band of millimeter waves were designed based on RGW technology. It was demonstrated that the use of two arms of different lengths in the feeding system allows the generation of CP in a simple way, without the need to implement an array along with a complex feeding network. Two feeding systems (wide and narrowband) based on RGW technology have been implemented to couple the wave to the radiating diamond slot.

The resulting antennas are small and very compact with excellent radiation characteristics. The simulated results and the measurements of the manufactured antennas are in good agreement. D antenna validates the novel way to generate CP. Then, to improve the gain in the system a DHG antenna was implemented. A broad

operation BW of 14.5% (60.3–69.6 GHz) with an AR < 3 dB is obtained by the DHG antenna. It achieves a maximum gain of 11.1 dB with a small footprint (30 mm × 30 mm), and RHCP with more than 15 dB of cross-polarization isolation.

Taking advantage of the top plate area in the D antenna, a BE structure consisting of four concentric periodic corrugations around the slot was implemented. The simulated and experimental results are in good agreement, demonstrating good radiation characteristics with a compact and low-profile structure. A high gain of around 18.4 dB at 58.5 GHz, with an aperture efficiency of 9% [small footprint (40 mm × 40 mm)] is obtained. A good CP purity with an AR of 0.59 dB at 60 GHz is demonstrated. More than 30 dB of cross-polarization isolation is observed in the measured radiation pattern, with a beamwidth equal to 11° and a side lobe level of −9.7 dB. This is the first ever BE antenna based on RGW technology and able to generate CP by itself, with excellent performance and relatively cheap manufacturing requirements. Compared with similar antennas, these designs are competitive variants that can have different uses, either in the 5G implementation or in any application operating in the 60–70 GHz band. Furthermore, thanks to their fully metallic structure, they can be scaled to operate at other frequency bands such as terahertz.

Chapter 3: Metasurface Lens Antennas in Groove Gap Waveguide Technology

3.1. Introduction

As mentioned in the previous chapters, GW technology allows a reduction of the manufacturing complexity compared to standard waveguides. In addition, fully metallic designs can be implemented, therefore avoiding the loss of typical dielectric substrates in the mmWave range, as well as to making the antenna robust to withstand harsh environmental conditions. Fully metallic lens antennas have emerged in recent years as an alternative for wireless devices at high frequencies exploiting the high directivity and scanning resolution they offer with relatively simple structures. One of the most versatile solutions is the Luneburg lens (LL) [87] antenna, whose rotationally symmetric Graded Index (GRIN) profile transforms a spherical wave into a planar wavefront with (ideally) perfect impedance matching to free space.

The geometry of the generalized LL problem with two external foci is illustrated in Fig. 3.1(a) in polar coordinates (r, θ). The LL is characterized by a spatially varying refractive index distribution with a rotational symmetry, see Fig. 3.1(a) and (b). The main characteristic of the LL is that when fed by a source placed exactly on the lens circumference, the LL collimates the rays at the output producing a plane wave at the opposite side, as illustrated in Fig. 3.1(b). In general, as shown in Fig. 3.1(a) when the source is placed far from the lens (at P_1) a focus is produced on the opposite side (P_2).
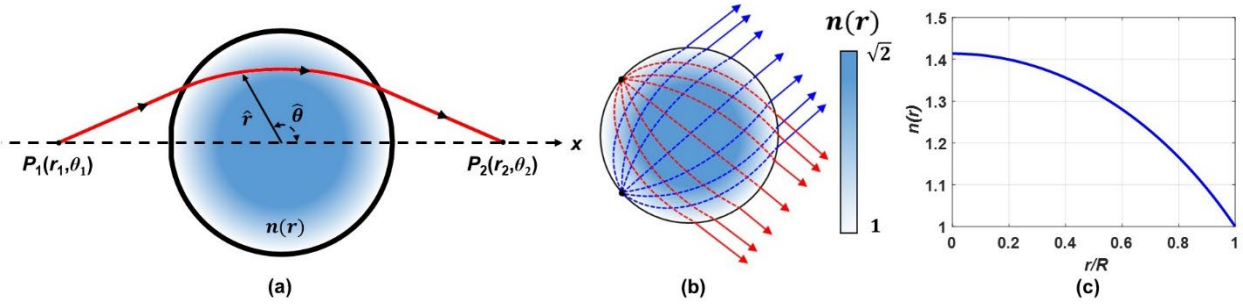
Fig. 3.1 Schematic of the (a) generalized Luneburg lens problem with two external foci P_1 and P_2; and (b) standard Luneburg lens with a focus on the contour and another focus at infinite (planar wavefront). (c) Equivalent refractive index of a 2D Luneburg lens as a function of the normalized radius r/R, where R is the outer lens radius.

The refractive index profile of a LL is inhomogeneous with radial dependence and obeys the following equation:

$$n(r) = \sqrt{2 - \left(\frac{r}{R}\right)^2} \qquad (3.1)$$

where r is the radial distance between a point inside the lens and its center, and R is the external radius of the lens. In the design proposed a planar LL with a fan beam radiation pattern is considered. The focusing properties of a LL are only defined by the refractive index distribution $n(r)$ (Fig. 3.1(c)), which means that the lens is capable of generating directive beams independently of the frequency provided the material has low dispersion.

3.2   Luneburg Lens Modulated in a Bed of Nails

As explained in [49], it is possible to modulate the effective refractive index for a transverse magnetic (TM) surface wave by loading a PPW with a fakir's bed of nails consisting of metallic posts of different heights. Since the height variation between neighboring pins inside the lens is smooth, each pin can be considered as immersed in a locally periodic environment. Such local periodicity entitles one to treat each pin as a unit-

cell in a periodic problem. Therefore, the dispersion characteristics for each unit-cell can be obtained in a straightforward manner by employing CST's eigenmode solver [132].

For instance, Fig. 3.2(a) shows the dispersion curves obtained for a PEC metallic pin structure of period p_{lens} = 1.1 mm, pin side a_{lens}= 0.5 mm and 3 different pin heights, h_{lens} = 0.3; 0.6; and 0.8 mm Using these curves, maps that link, for a specific frequency, the pin height to the wavenumber k_x of the fundamental TM mode inside the loaded PPW can be constructed. The effective refractive index n_{eff} can thus be retrieved using $k_x=n_{eff}k_0$, as shown in Fig. 3.2(b) and (c).
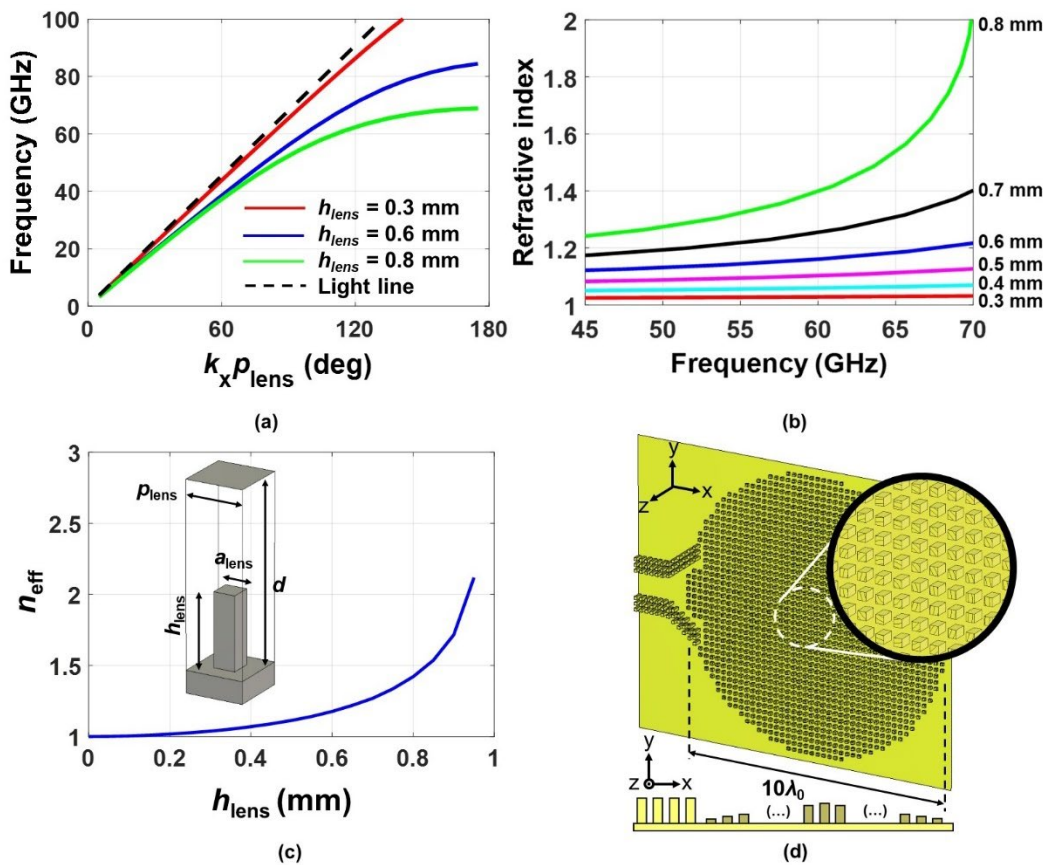
Fig. 3.2 (a) Dispersion diagram of a periodic metallic pin structure [shown in the inset of panel (c)] with the following dimensions: p_{lens} = 1.1 mm, a_{lens}= 0.5 mm and h_{lens} varying from 0.3 to 0.8 mm. (b) Equivalent refractive index as a function of frequency for different pin heights (from 0.3 to 0.8 mm). (c) Equivalent refractive index as a function of the pin height at f_0 = 60 GHz. (c) Schematic showing the Luneburg lens and the GGW horn antenna; (top inset) zoom into the pins of the metalens in the central region; (bottom inset) sketch showing the metalens side view.

The GRIN LL is synthesized by dividing the circular area according to a Cartesian lattice that matches the selected periodicity of the unit cell, p_{lens}. Then, (3.1) is applied to compute the ideal refractive index in each square of the lattice. Such values can be mapped to a pin height (h_{lens}) using the curve depicted in Fig. 3.2(b). Fig. 3.2(c) shows the structure resulting of this synthesis process. The lens has an external diameter of 50 mm ($10\lambda_0$, where λ_0 is the free space wavelength at the design frequency f_0 = 60 GHz) and the metallic pin height varies between 0.3 and 0.8 mm.

3.3   Horn Antenna using Groove Gap Waveguide Technology

The next step is to design the GGW horn antenna feeding the LL. It must be ensured that the wave is confined within the groove of width 4.2 mm and height 1.75 mm by the metallic pins and the top and bottom metallic plates. Again, the eigenmode solver of CST Studio Suite® was employed to obtain the pin dimensions that fix a bandgap around the operation frequency. As shown in Fig. 3.3(a), with a width of a_{horn} = 0.5 mm, a height of h_{horn} = 1.5 mm, periodicity p_{horn} = 1 mm and distance to the upper metallic layer of 0.25 mm, a bandgap arises centered at 60 GHz and spanning from 40 to 80 GHz. The inset of Fig. 3.3(b) shows the dispersion diagram of three rows of pins with a central groove of width 4.2 mm, separated from the upper lid by the air gap, infinite along the x-direction. The field distribution in the cross section for a frequency within the desired "monomode" band (60 GHz) is shown in Fig. 3.3(c). In The field distribution is similar to the TE_{10} mode of a standard waveguide, with the electric field vertically polarized with respect to the plates [133].
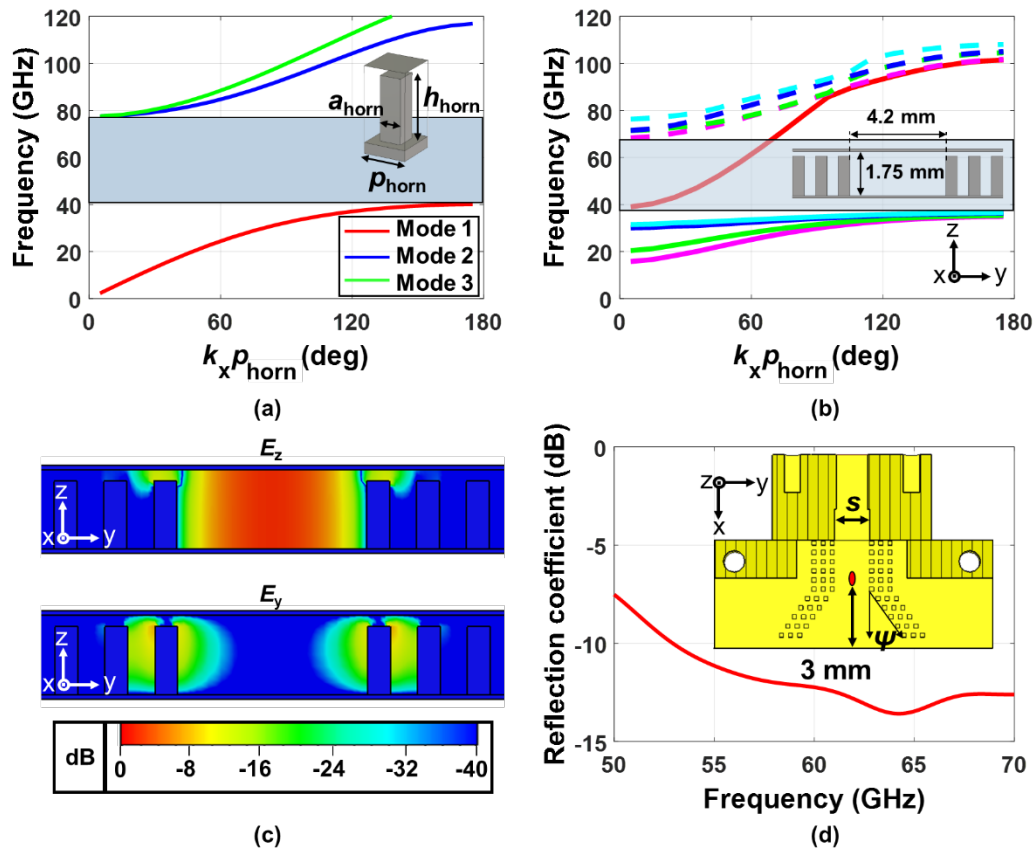
Fig. 3.3 (a) Dispersion diagram of a periodic metallic pins structure (shown in the inset) with dimensions: p_{horn} = 1 mm, a_{horn} = 0.5 mm and h_{horn} = 1.5 mm. (b) Dispersion diagram of three row of pins with a central groove of 4.2 mm and height 1.75 mm. (c) 2D contour plot of the transverse electric field components (E_z and E_y) at 60 GHz, where the GGW has monomode operation. (d) Simulated input reflection coefficient of the GGW horn antenna in dB; (Inset) top view showing the width of the step (s = 4.2 mm) the horn flare angle (Ψ = 35°) and an estimation of the phase center location (red ellipse).

Using these dimensions for the GGW pins, and after an optimization process, the H- plane horn is designed by gradually opening the waveguide with a linear variation and an angle of ψ = 35° for operation at 60 GHz. In the experimental setup the GGW must be connected to a standard WR-15 waveguide. As the WR-15 waveguide and the GGW have different widths, a step transition was designed to avoid impedance mismatch. Fig 3.3(d) shows that the input reflection coefficient is below −10 dB from 54 GHz up to the upper

limit of *V*-band (70 GHz). The inset in Fig. 3.3(d) shows a top cross section view of the antenna highlighting the designed step of *s* = 4.2 mm and length 3.7 mm.

To optimize the performance of the lens-antenna system, the focus of the lens (which in an ideal LL should be exactly at the circumference) must be carefully aligned with the phase center of the GGW horn antenna. The phase center is determined from the simulation results of the H-plane at 60 GHz. First, we determine the angular aperture where the directivity decreases around −12 dB from its maximum value and find that it is ±42°, see Fig. 3.4(a). This value ensures a correct illumination of the lens without excessive spillover. Next, the phase center is found by searching a phase curve between these angles as flat as possible, Fig 3.4(b). After this process, it is concluded that the phase center is inside the GGW horn at 3 mm from the aperture, depicted as a red ellipse in the inset of Fig. 3.3(d). As shown in Fig 3.4(b), a small variation lower than 10° is achieved between ±42°.
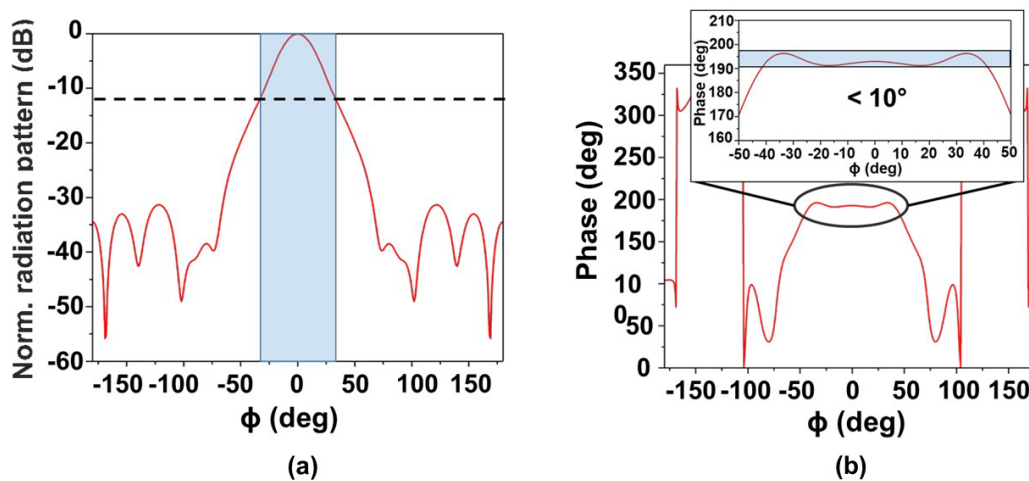
Fig. 3.4 (a) Normalized magnitude of the H-plane radiation pattern at 60 GHz (simulation result); the shaded region is the angular aperture where the directivity is above −12 dB from the maximum. (b) Phase of the H-plane radiation pattern at 60 GHz (simulation result); (inset) detail showing the phase variation in the ±50° range; the region where the phase variation is below 10° has been highlighted.

The GGW horn antenna is therefore slightly inserted into the LL, as shown in Fig 3.5(a), to match the LL focal circumference with the horn's phase center. This is corroborated by

a parametric analysis using an auxiliary parameter m_x, which represents how much the antenna is inserted inside the lens (m_x = 0 means that the antenna aperture coincides with the LL focal circumference and a positive m_x means that the horn is inserted into the lens). Fig. 3.5(b) shows the reflection coefficient and directivity for several values of m_x varying from 0 to 4 mm. When the GGW horn aperture is exactly at the rim of the lens (m_x = 0 mm), the directivity drops at the upper frequency limit. The maximum directivity over the bandwidth is achieved when m_x = 3 mm, in good agreement with the phase center position previously calculated.

(a)

(b)

(c)

(d)
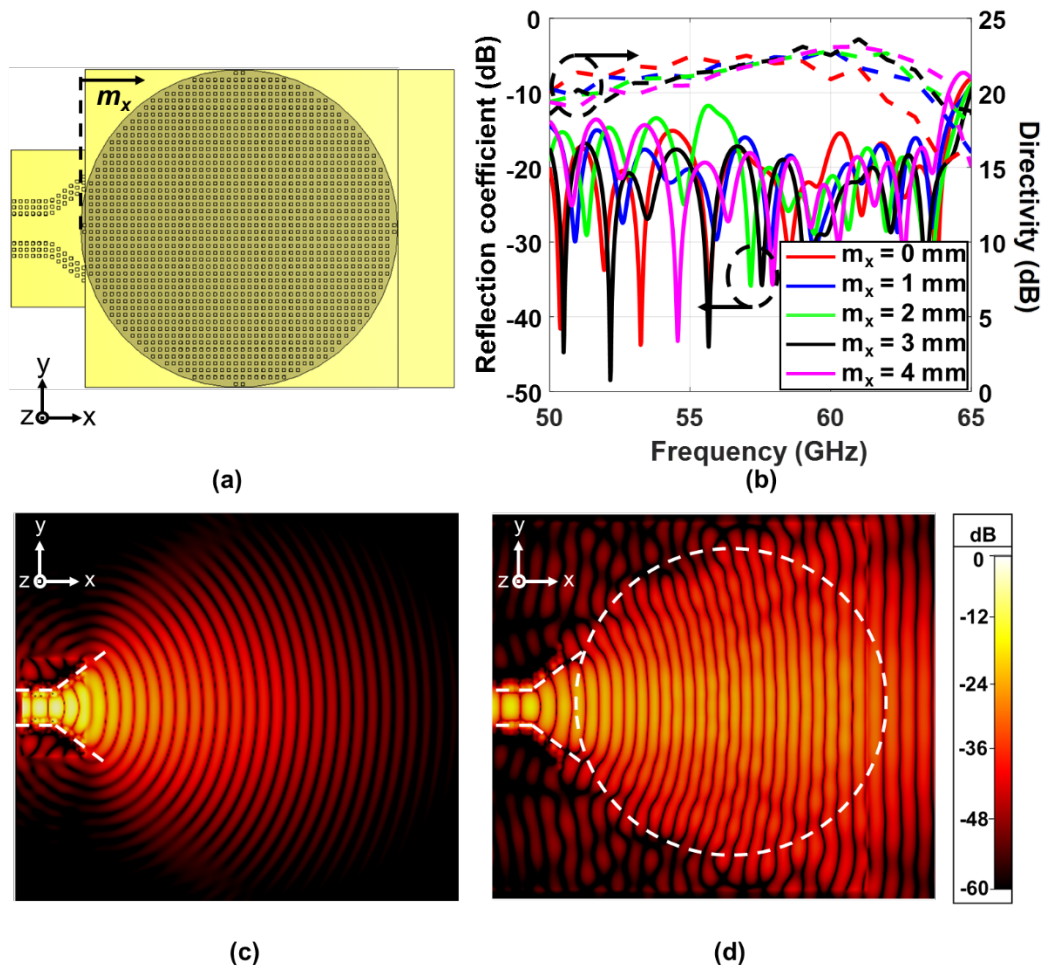
Fig. 3.4 (a) Schematic of Luneburg lens, GGW horn antenna and flare (top view) highlighting the parameter m_x that controls the relative position of the lens and the horn antenna (b) Parametric simulation results of reflection coefficient and directivity varying m_x from 0 to 4 mm. (c) Normalized $|E_z|$ without metalens at 60 GHz in decibel scale. (d) Normalized $|E_z|$ at 60 GHz with metalens (m_x=3) in logarithmic scale.

Finally, Fig. 3.5(c) and (d) show the top view of the normalized vertical component of the simulated electric field at 60 GHz with and without the lens. It is clear that the lens shapes the cylindrical wavefront radiated by the GGW horn into a planar wavefront.

3.4   Simulation and Experimental Results

The previously discussed LL GGW antenna was manufactured and measured. A standard CNC milling machining with a tolerance of +/- 20 μm was selected to manufacture the two blocks presented in Fig. 3.5. Aluminum was considered for all of the constituent pieces, and was modeled as a lossy metal with a conductivity of 1.72×10^7 S/m [101]. Photographs of the manufactured prototype are shown in Fig. 3.5(a)-(c). A flare section was implemented to improve the radiation pattern and the matching to free space, as shown in Fig. 3.5(d) and its inset. The flare dimensions were obtained by launching an optimization of the radiation characteristics, giving as a result an angle of 21° and a length of 20.8 mm. The final system has a total volume of 88.5×62.6×19.05 mm, Fig. 3.5(a) and (b).
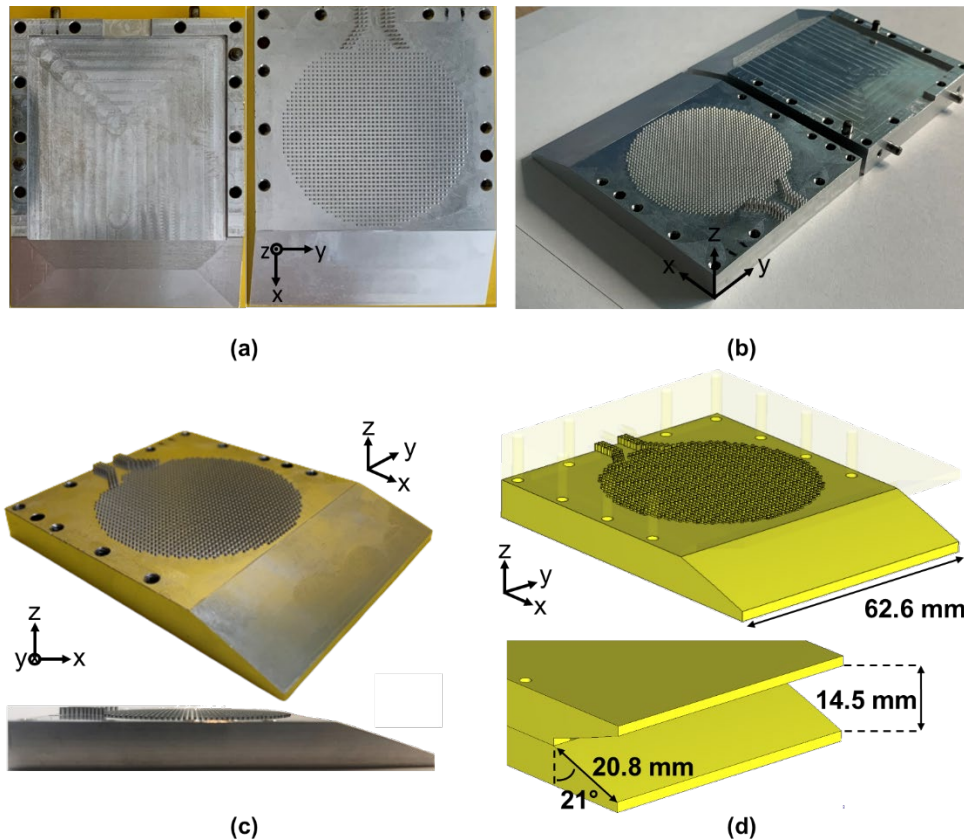
Fig. 3.5 Picture of the fabricated antenna showing: (a) a top view of the upper block (left) and bottom block (right) with the metalens horn antenna, (b) perspective view of the upper block (right) and bottom block (left) with the metalens horn antenna. (c) Photograph of the bottom piece in perspective view (top) and profile view (bottom) to show clearly both the lens and GGW antenna pins. (d) Perspective view of the bottom plate (top panel) and a zoom into the flared section (bottom panel).

The far-field measurements were performed using two different setups. Radiation pattern planes, peak directivity and aperture efficiency (η_{eff}) were obtained using the planar near field setup shown in Fig. 3.6(a). In this setup, the lens antenna (Antenna Under Test, AUT) was aligned with its H-plane parallel to the z-axis and the E-plane parallel to the y-axis, see Fig. 3.6(a). An open-ended waveguide probe with sharp edges (surrounded with TK-RAM absorbing material to reduce undesired reflections [134]) was used to scan the electric field at a distance d_m = 70 mm from the AUT, far enough to prevent reactive coupling between the AUT and the probe and close enough to avoid

measuring a very large plane. The measurements were taken by moving the probe position along the *yz*-plane in a rectangle of 560×240 mm^2 with a step of 2 mm (less than λ_0/2) and sweeping the frequency at each point. A precise alignment process was done to ensure that the AUT and the probe were parallel prior to recording the co-polar and cross-polar planar near fields. A PNA network analyzer E8361C (Agilent Technologies) was used to measure the antenna in the frequency range from 45 to 70 GHz, with the frequency span discretized in steps of 50 MHz. A single-port calibration was performed to measure the reflection coefficient of the lens antenna system. The far field radiation patterns and, from them, the directivity and aperture efficiency were finally obtained by applying a near to far field transformation and probe correction.
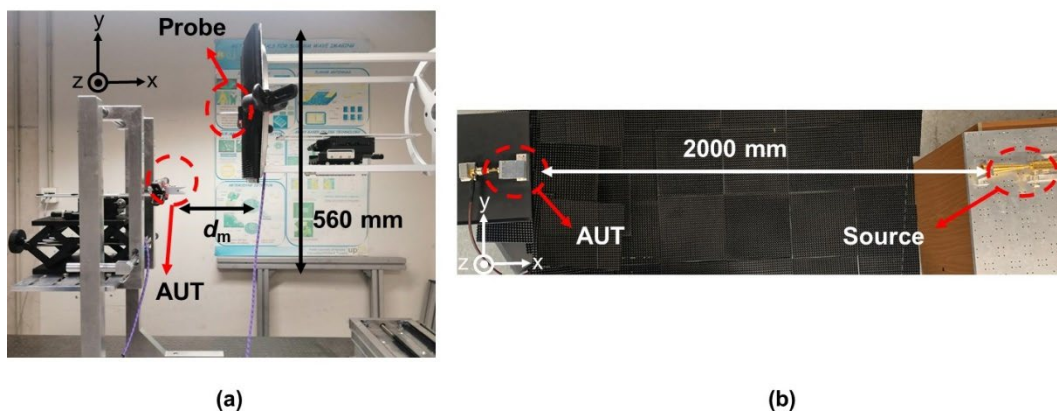
Fig. 3.6 Experimental: (a) near field setup highlighting the distance between the AUT and the probe (d_m = 70 mm); red circles mark the LL antenna (AUT) and the probe positions. (b) top view of the far field setup highlighting the distance between the AUT and the probe of 2000 mm.

In addition, a far field setup was implemented to measure the gain by applying the gain comparison (or gain transfer) method, see Fig. 3.6(b). Two identical calibrated standard horn antennas (source and detector) of known gain and linear polarization were carefully aligned and placed at a distance of 2000 mm, farther than the minimum far field distance determined by the AUT dimensions, which is around 1930 mm at the maximum frequency of the band (70 GHz). To avoid undesired reflections on the ground between the antennas, the floor was covered with RAM. Nevertheless, the setup does not use an

anechoic chamber and hence is prone to reflections with the objects in the laboratory, introducing some ripple and uncertainty in the measurements, at it will be shown below. The measurements were performed using an AB Millimeter Vector Network Analyzer MVNA-8-350 operating from 45 to 70 GHz with a frequency step of 0.5 GHz
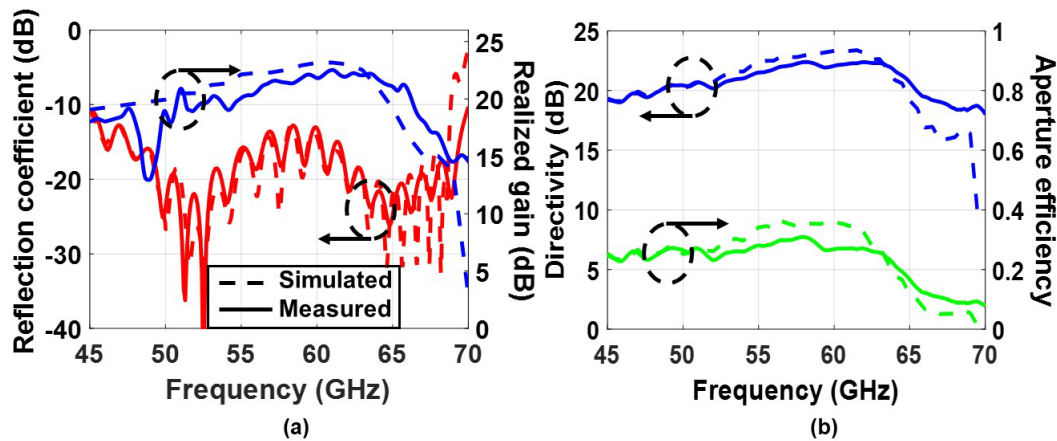
Fig. 3.7 (a) Simulated (dashed lines) and measured (solid lines) reflection coefficient (red) and realized gain (blue) in dB. (b) Directivity (blue curve) in dB. Inset, aperture efficiency (η_{eff}) from 50 to 65 GHz (green curve).

Fig. 3.7(a) shows the simulated (dashed) and experimental (solid) results corresponding to the magnitude of the input reflection coefficient (red) and the realized gain (blue) of the lens antenna. The antenna has a good impedance matching in all the considered band (from 45 to 70 GHz), with an input reflection coefficient below −10 dB and an excellent agreement between simulation and experimental results. The experimental realized gain reaches a maximum value of 22.5 dB at 61 GHz and is above 20 dB in almost the entire band, with a fair agreement with the simulation results. Furthermore, the realized gain bandwidth (defined as the frequency range where the gain is above −3 dB with respect to the maximum) is close to 15.7 GHz (from 50.7 GHz to 66.4 GHz). Hence, the fractional bandwidth is around 26.2%. Note that these results must be taken with some caution because measurements were not performed in an anechoic chamber and there are measurement uncertainties caused by undesired reflections in the setup which add to the uncertainties intrinsic to the gain comparison method.

Nevertheless, at the operation frequency, these reflections are not so detrimental as they are at lower frequencies due to the rapid decay of the fields at mmWaves.

Fig. 3.7(b) shows the directivity measurement (blue curve) and the aperture efficiency (green curve) extracted from the near field setup measurements. Notice that the realized gain and directivity have similar behavior, demonstrating the excellent radiation efficiency of the structure and the low losses due to the fully metallic design. However, the aperture efficiency illustrated in Fig. 3.7(b) inset is low (between 0.2-0.3 from 50 to 65 GHz). This parameter could be improved with a different flare implementation, following a different shape such as an exponential curve. Nevertheless, given that antennas with a fan-beam pattern like the one considered here usually have moderate values of aperture efficiency (as a result of the wide beamwidth in one of the radiation planes) a linear flare was chosen in the design to simplify the manufacturing process.

The copolar and cross polar radiation patterns are shown in Fig. 3.8(a)-(d). Radiation patterns are only represented from $-60° \leq \theta \leq 60°$. This limitation comes from the size of the sampled plane along with the AUT size and the distance between the AUT and the probe, which does not allow to obtain larger angles with the applied method (near field setup). Several representative frequencies were selected and plotted (from 50 to 65 GHz with steps of 5 GHz). The E-plane (co-polar in red and cross-polar in cyan) and H-plane (co-polar in blue and cross-polar in green) normalized radiation patterns are included in all cases. Again, an excellent agreement between simulation and experimental results is observed.
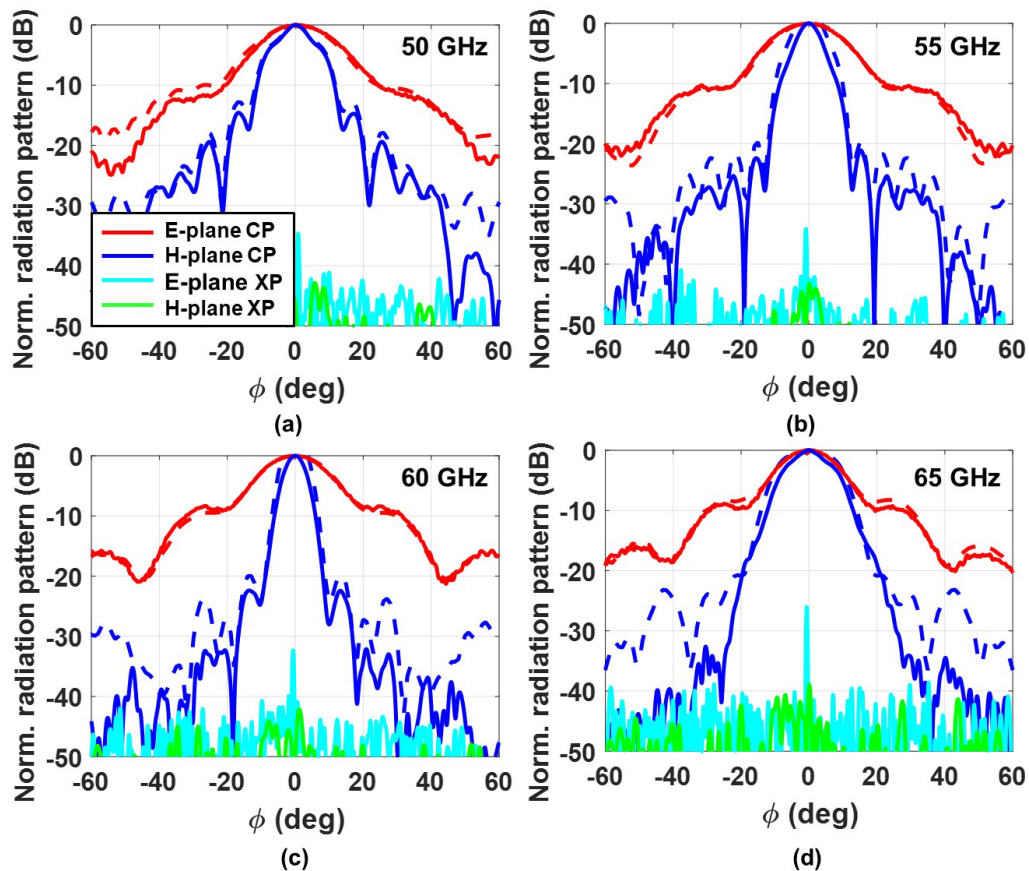
Fig. 3.8 Simulated (dashed lines) and measured (solid lines) normalized far field radiation patterns at: (a) 50 GHz, (b) 55 GHz, (c) 60 GHz and (d) 65 GHz.

The SLL at 60 GHz is around −22 dB and in the worst case is 50 GHz where the SLL is −15 dB. An excellent cross-polar discrimination, higher than 25 dB, is noticed in all cases. Obviously, the antenna presents a narrower beamwidth in H-plane than in E-plane (at 60 GHz H_{HPBW} = 6.8° and E_{HPBW} = 21°), since the former one is the plane where the LL collimates the beam. Fig. 3.9(a) shows the −3dB beamwidth versus frequency, where it is clear that the beam is narrower in the H-plane. Fig. 3.9(b) shows the electric field copolar magnitude in the measured plane at 70 mm from the antenna and Fig. 3.9(c) the far-field 2D radiation pattern at 60 GHz. The fan beam pattern, narrower in the H-plane, is evident in both plots.
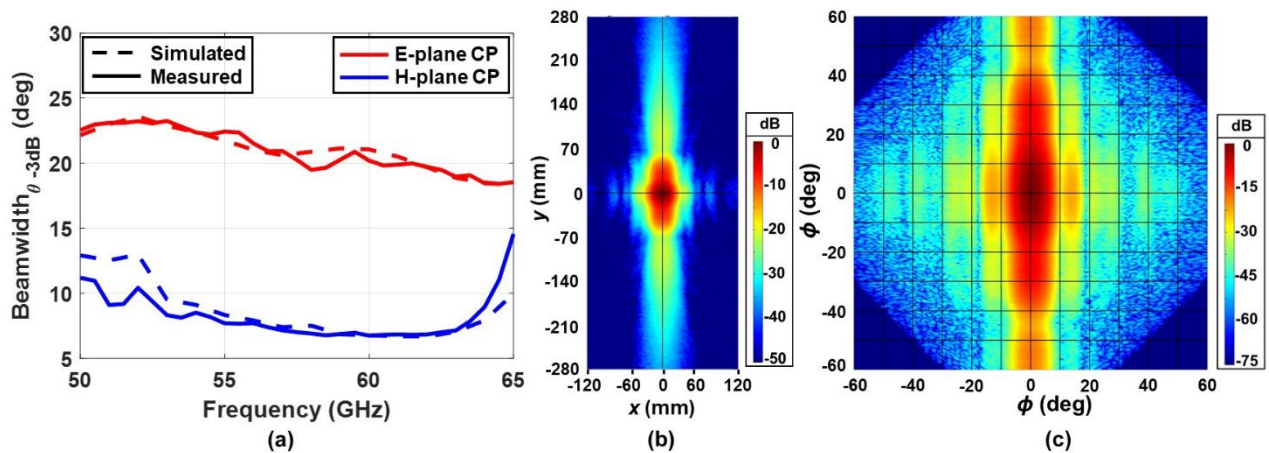
Fig. 3.9 (a) −3dB beamwidth in the E-plane (red curves) and H-plane (blue curves) as a function of frequency. Simulation (dashed lines) and measurement (solid lines) results. Field pattern at 60 GHz: (b) near field measurement (c) far field transformation.

There are nevertheless some results that need further clarification. First, there is a dip in the measured directivity between 55 and 60 GHz that does not appear in the simulation results [Fig. 3.7(b)]. Furthermore, this dip is in apparent contradiction with the behavior observed in the radiation patterns, where the beamwidth in the measured H-plane is narrower than in the simulation [Fig. 3.8(d), (e)]. However, looking closely, it can be observed that the measured E-plane is wider and has higher side lobes, counterweighting the beamwidth reduction in the H-plane and leading to a decrease of the measured directivity in that frequency range. This phenomenon can be attributed to very small errors in the manufactured prototype.

In addition to this, there is an important directivity drop at 65 GHz that appears both in the simulation and experimental results. This is a consequence of the dispersion of the metallic pin array used to modulate the refractive index by varying the pin height as presented in Fig. 3.2(b). From that figure and also from Fig. 3.2(a), it is clear that the refractive index is dispersive and has an abrupt variation from 65 GHz onwards, especially for pin heights between 0.7 and 0.8 mm. To fully understand the underlying physics, the discretization applied to modulate the LL must also be considered. A contour

plot of the ideal refractive index distribution applying (3.1) is presented in Fig. 3.10(a), where a small discretization step of 0.1 mm has been employed. However, the implemented lens has a coarser period (p_{lens} = 1.1 mm) leading to the discretized index profile shown in Fig. 3.10(b). Gray circles superimposed in that figure delimit the boundaries of regions of pins with the same height (up to 22 different pin heights were used in the lens). Looking closely, it is found that most of the lens area (up to 48.1%) contains pins with heights above 0.7 mm, which have strong dispersion above 65 GHz. Therefore, it can be concluded that the drop-in directivity beyond that frequency is a consequence of the pin dispersion, which leads to refractive index values far from the Luneburg equation. This is corroborated in Figs. 3.10(c) and (d) that show the electric field distribution at 65 and 70 GHz. It is appreciated that the field inside the lens greatly differs from the electric field when the refractive index matches the Luneburg equation [Fig. 3.4(d)]. Hence, the output wavefront is no longer planar and this effect leads to the observed directivity drop.

Fig. 3.10. (a) Planar LL and its radially symmetric refractive index n(r) with a discretization of 0.1 mm. (b) Mapping representation of the LL refractive index implemented with discretization of p_{lens} = 1.1 mm, where the gray dashed circles delimit the regions with pins of the same height (black dashed circles are some selected labels). (c) Top view of the normalized $|E_z|$ metalens in decibel scale at 65 GHz. (d) Idem at 70 GHz.

There are excellent works in the literature that propose metamaterial unit cells with low dispersion [7], [12], [26]. For instance, some implementations such as glide symmetric unit cell designs are less dispersive, giving rise to wide bandwidth and good directivity performances. However, this technology is difficult to implement as frequency increases due to the small gap between lower and upper pins needed to obtain wide bandwidth.

Table 3.1 presents comparison of simulated and experimental results including the previous parameters along with the matching bandwidth, peak directivity and fractional directivity BW.

Table 3.1: Comparison Between Simulated and Measured Results

Parameter	Simulated	Measured
S11 (dB) BW*	50 – 65 GHz	50 – 65 GHz
Directivity Peak	23.1 dB at 60 GHz	22.4 dB at 58.1 GHz
Realized Gain Peak	23 dB at 61 GHz	22.5 dB at 61 GHz
Fractional Gain BW+	22.7%	26.2%
SLL (at 60 GHz)	20 dB	22.4 dB
HPBW (at 60 GHz)	E-plane = 21° H-plane = 7°	E-plane = 21° H-plane = 6.8°

3.5   Conclusions

To conclude, a fully metallic LL antenna system excited by a GGW horn operating at *V*-band has been demonstrated. The LL has been synthesized using metallic pins to obtain the desired refractive index profile, which provides a planar wavefront in the direction of propagation. A GGW horn antenna has been also designed and combined with the LL to get a fully metallic design compatible with the requirements of wireless communication systems at mmWave. Owing to the fully metallic design, this system is more robust and presents lower losses than solutions involving typical dielectric substrates. Moreover, the final design is quite flat, making it easy to adapt to planar surfaces. The simulated and experimental results are in good agreement demonstrating that CNC micromachining is a viable alternative even at high frequencies where tolerances are critical and designs based on small constituents such as metallic pins are challenging.

A high directivity of around 22.4 dB is achieved at 58.1 GHz, and a realized gain of 22.5 at 61 GHz (the gain is above directivity due to small measurement uncertainty in the gain method). The realized gain bandwidth is of around 26.2%. A cross-polarization discrimination higher than 25 dB is observed in the measured bandwidth. This antenna based on GGW technology is able to generate excellent radiation characteristics and could be used in applications at mmWave.

Chapter 4: Dual Layer Reflector Geodesic Lens Antenna

4.1   Introduction

The designs of 2D LL mentioned in section 3.1 are achieved mostly by varying the refractive index using layered dielectrics or periodic structures, such as the metallic pin array described in previous chapter. A limitation of this method is that the continuous refractive index proposed in eq. (3.1) must be discretized due to the finite size of the unit cell introducing deviations from the analytical equation, as explained in section 3.2. Alternatively, a geodesic Luneburg lens (GLL) can achieve a continuous refractive index distribution avoiding discretization.

Geodesic lenses are lenses based on curved surfaces which mimic an arbitrary refractive index distribution [91], are rotationally symmetrical and independent of the frequency. Rinehart [88] proposed an equivalent to the LL with a homogeneous medium within the PPW by introducing the arc length of a geodesic as a function of the lens radius, $s(\rho)$, where ρ is also a normalized radius, defined in a cylindrical coordinate system with its origin at the center of the lens. The working principle of a GLL is based on increasing the physical path to emulate the refractive index extracted from the Luneburg equation by guiding the wave along the height of the lens. GLLs are then a solution of LL that avoid the use of a gradient index and achieve the required phase difference by varying the optical path.

Although not mentioned in the previous chapter, there are two mains solutions for LL which can also be obtained by applying geodesic concepts: the conventional one, where the source and the focus are at opposite spaces, represented in Fig. 4.1(a); and the complementary solution, where the focus is virtual and is obtained in the same semi-space as the source, as shown in Fig. 4.1(b).

(a)

(b)
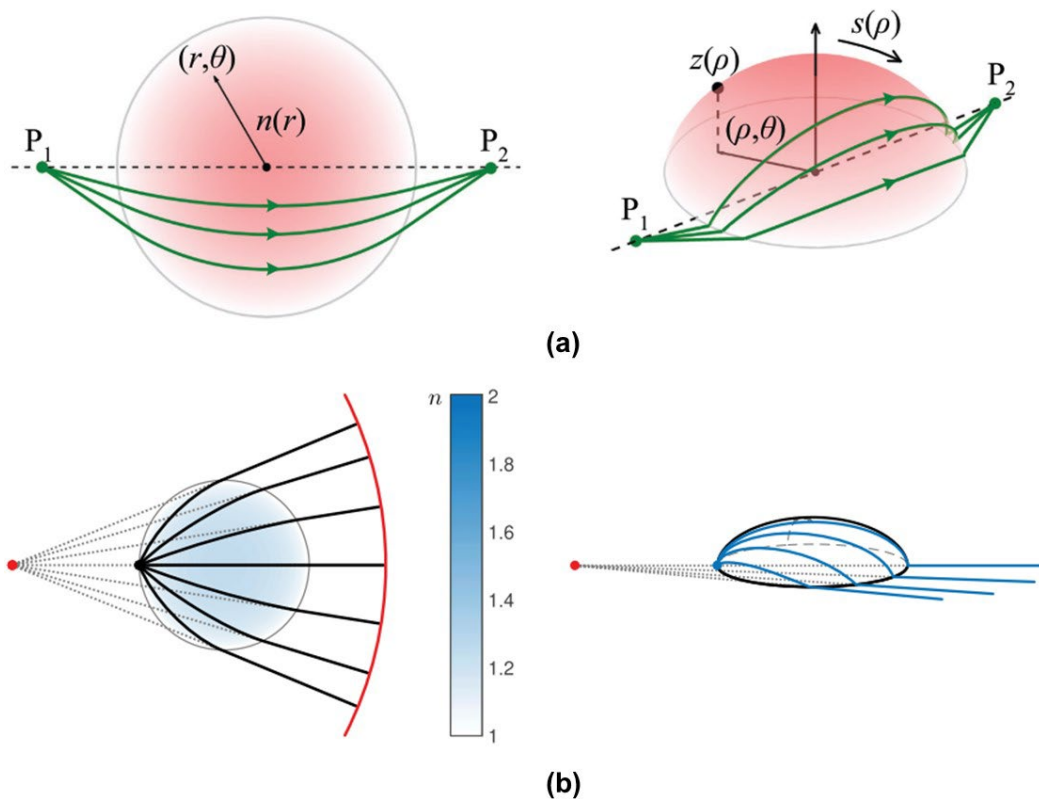
Fig. 4.1 Schematic of: (a) a Luneburg inverse problem to find the refractive index profile, $n(r)$ or the equivalent geodesic lens shape, $z(r)$, with pre-specified foci P_1 and P_2 [135]. (b) Complementary Luneburg lens with virtual image with inhomogeneous index (left) and geodesic lens geometry (right) [136].

Spherically and rotationally symmetric lenses producing sharp virtual images can be of interest in antenna systems, complementing and extending existing solutions. Combined with reflector systems, can improve the unifocal property of a hyperbolic sub-reflector in a classical dual-reflector Cassegrain geometry. In the case studied here, the

complementary solution is employed to illuminate a planar reflector in a dual-layer parallel plate design to achieve a compact footprint.

This chapter is then devoted to the design of a complementary GLL with a virtual focus designed to illuminate a planar reflector at 60 GHz. This complementary GLL design configuration provides a virtual focus far away from the GLL. This way, the parabolic reflector "sees" a virtual source placed at a point aligned with its focus several wavelengths away, even though the actual source is at the GLL edge. Hence, a compact system can be achieved. The prototype is realized using a dual-layer parallel plate, namely a pillbox structure [101], [117], [118]. Fig. 4.2 illustrates the wave propagation from the feeding point towards free space. A source near the GLL is used to excite the wave on the top layer. The wave at the output of the GLL has a cylindrical wavefront with center at the virtual lens focus. This propagates towards a parabolic reflector placed at the end of the top layer whose focal length coincides with the virtual focus of the GLL. Then through a 45 deg chamfered mirror [Fig. 4.2(inset)] the wave is coupled to the bottom layer and propagates in the opposite direction with a planar wavefront thanks to the effect of the parabolic reflector. Furthermore, taking advantage of the rotationally symmetrical property of the geodesic lenses, multiple feeding is proposed in order to obtain beam scanning capability.
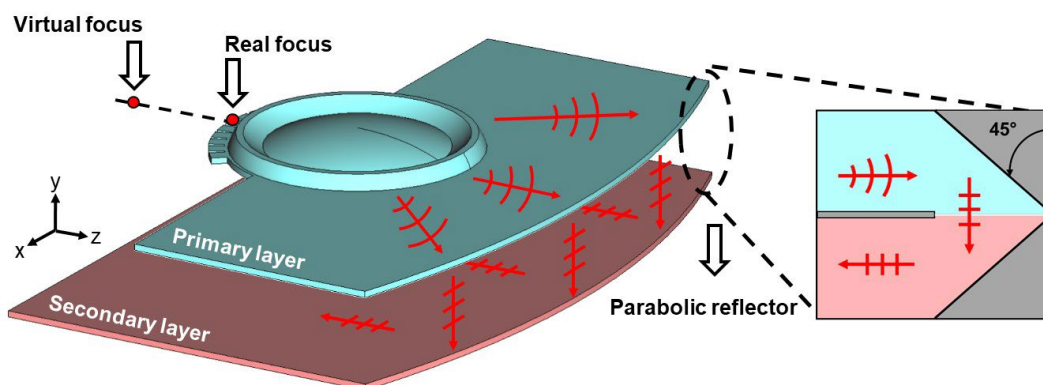
Fig. 4.2 Schematic of a dual-layer (pillbox structure) GLL + parabolic mirror system. Conceptual representation of the field propagation from the top layer (cylindrical wavefront) to the bottom layer (planar wavefront) through the parabolic reflector. Inset, detail of the corner reflector.

Finally, a comparison with a standard parabolic reflector is done using a ray-tracing analysis to evaluate the pillbox structure behavior. The parameters evaluated are directivity, SLLs, and scanning range. This comparison demonstrates the advantages of the complementary GLL configuration over classical reflectors.

4.2 Geodesic lens configuration

In a geodesic lens, the physical path is modulated by changing gradually the height profile, $z(\rho)$. The system considered here is a PPW filled with a homogenous and isotropic dielectric, in this case air. As discussed in [91], the height gradient as a function of the radius particularized to the case of GLL (a rotationally symmetric case) can be obtained with the following equation, obtained by geometrical optics:

$$\frac{dz}{d\rho} = \sqrt{\left(\frac{1}{2} + \frac{1}{2\sqrt{1-\rho^2}}\right)^2 - 1} \qquad (4.1)$$

A schematic of a generalized LL inverse problem with foci at P_1 and P_2 and a gradual index is shown in Fig. 4.1(a) left. Fig. 4.1(a) right shows the same case as before, but this time in a geodesic shape, where the physical path is modulated with a gradual height, $z(\rho)$ [91][1]. Most lens profiles are usually obtained by solving a canonical Luneburg inverse problem[2] with a pair of pre-specified foci that must be real [91]. However, this concept

---

[1] The profile is obtained by solving Eq. (9) in the mentioned reference.

[2] In the literature this denomination is used because the refractive index of the lens is calculated by solving an inverse problem: assuming a plane wave coming from the infinite and focused in an arbitrary predefined point.

can be extended to produce a virtual focus on the same side as the source point of the lens by solving a complementary Luneburg inverse problem [136], Fig. 4.1(b).

4.2.1   A complementary solution to the generalized Luneburg lens problem

The complementary solution of the generalized LL is a family of lenses that can have a virtual focal image. They are designed to produce a real image as a direct consequence of the formulation of the generalized LL problem [87], [91], see Fig. 4.3(a).

Fig. 4.3(b) illustrates the complementary problem which in essence is similar to a classical divergent lens. The circle delimits the boundaries between the lens filled with a gradient index, $n(r)$, and the background, $n = 1$. In this complementary lens, the rays emerging from the lens converge in a virtual image point at the same semi space as the source. Therefore, the rays stemming out of the lens apparently come from this virtual image point (r_i) and diverge from it rather than converging at the output (unlike the generalized LL depicted in Fig 4.3 (a)). The analytical solution for the complementary LL is provided in [128] for both gradient index and geodesic versions.

(a)   **(b)**
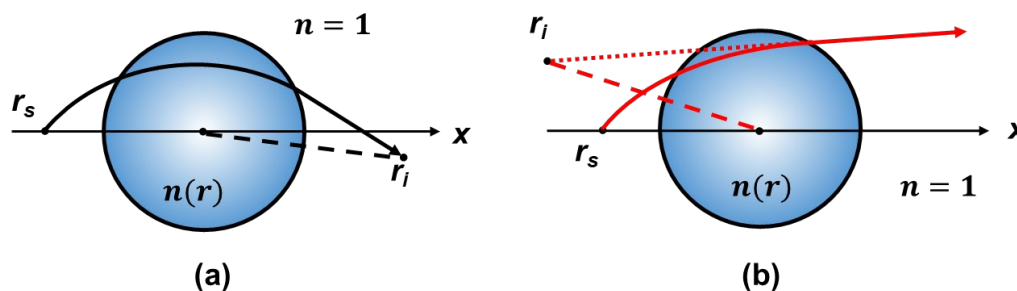
Fig. 4.3 A schematic representation of (a) the generalized Luneburg lens problem and (b) the proposed complementary problem in an inhomogeneous medium.

The complementary GLL profile is obtained by using the approach described in [91] and developed in [136], assuming $r_s = 1$ (real source exactly on the lens edge):

$$s(\rho) = \frac{\rho}{2} + \frac{1}{\pi}\left[\rho \sin^{-1}\sqrt{\frac{1-\rho^2}{r_i^2-\rho^2}}\right.$$

$$\left. + r_i \sin^{-1}\left(\rho\sqrt{\frac{r_i^2-1}{r_i^2-\rho^2}}\right) - \left(\sqrt{r_i^2-1} + \sin^{-1}\frac{1}{r_i} - \frac{\pi}{2}\right)\sin^{-1}\rho\right]. \tag{4.2}$$

The corresponding geodesic lens profile in cylindrical coordinates (ρ, θ, z) is obtained by solving the differential equation $dz^2 = ds^2 - d\rho^2$. Due to the eminently practical content of this thesis, the detailed theoretical development of this complementary solution extensively analyzed in [136], has not been delved into.

To illustrate the physical operation, a full simulation using the commercial software CST Studio Suite® was done comparing the classical and the complementary LL. Fig. 4.4(a) shows the shape of a geodesic Luneburg lens following eq. (4.1) for $P_1 = 1$ (on the periphery) and $P_2 = \infty$ (planar wavefront). Fig. 4.4(b) shows the electric field response, showing clearly that the wavefront at the output is planar, as determined by the LL equation.
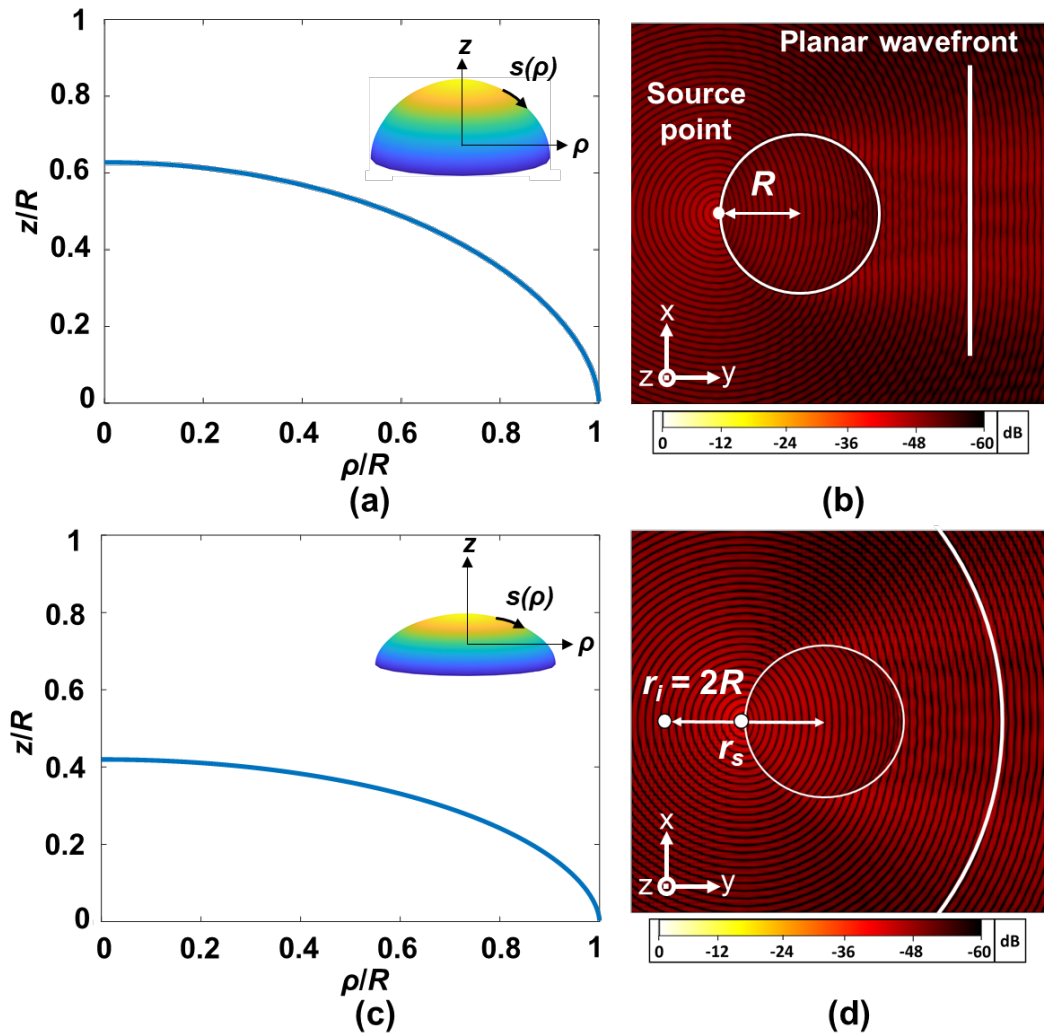
Fig. 4.4 (a) Normalized geodesic Luneburg lens. (b) Normalized $|Ez|$ field magnitude for a geodesic Luneburg lens. (c) Normalized geodesic curve for the complementary lens with a virtual source with $r_s = R$ and $r_i = 2R$, where R is the radius of the lens. (d) Normalized $|Ez|$ field for the complementary problem.

The shape of a complementary GLL obtained from (4.2) is shown in Fig. 4.4(c) placing the virtual image at $r_i = 2R$ (where R is the radius on the lens) from the center when the lens is excited from the periphery ($r_s = R$). Fig 4.4(d) shows that the wavefront at the output is centered on the virtual image (r_i) on the left side of the plot. The virtual image and the cylindrical wavefront centered on it are highlighted in white in the figure.

4.3 Simplified complementary geodesic lens designs

In order to simplify the design of complementary GLL it is possible to use an alternative formulation to (4.2) as proposed in [94] by taking into account that geodesic lens profiles (both conventional and complementary) resemble half of an ellipse curve:

$$z(\rho) = h_0(1 - \rho^p)^{\frac{1}{q}} \tag{4.3}$$

where $h_0 = 0.4191$ is the height of the reference Rinehart–Luneburg lens, and $p = 2.07$ and $q = 1.802$ are exponents of the generalized super ellipse. The super ellipse is a closed curve resembling the ellipse, retaining the geometric features of semi-major axis and semi-minor axis, and symmetry about them, but a different overall shape. This approximation is easier to implement in a simulator like CST Studio Suite® because it has a closed and simple parametric dependence, unlike eq. (4.2). For the lens implemented here, the error between both expressions is less than $1.2 \cdot 10^{-3}$, see Fig. 4.5(a) inset.

(a) (b) (c)
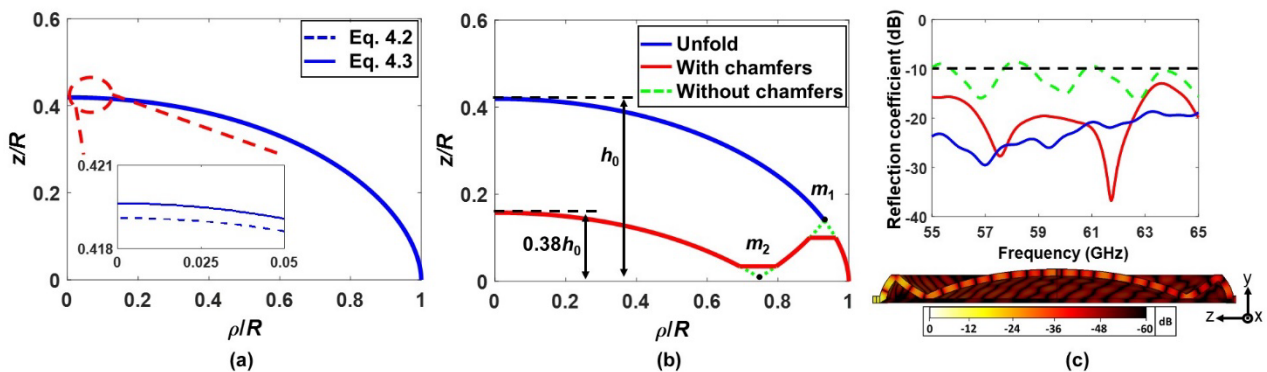
Fig. 4.5 (a) Axial symmetric normalized height complementary lens profiles using (4.2) dashed blue curve and (4.3) solid blue curve. (b) Representation of three profiles, where m_1 = 0.93 and m_2 = 0.75 are mirror points. Blue solid curve is the lens profile using (4.3), red solid curve is the lens profile with chamfers at the inflection points (m_1 and m_2) and green dashed curve is the lens profile without chamfers. (c) Top, reflection coefficient for the three considered cases (all the lens is simulated). Bottom, cross-sectional view of the normalized E-field distribution at 60 GHz for the case with two chamfers implemented.

In [93], Kunz suggested that a geodesic lens may be folded by applying reflection symmetry with respect to a plane perpendicular to the lens curve and intersecting it. This principle was applied twice in the complementary geodesic profile as shown in Fig. 4.5(b). This strategy allows reducing the overall height in such a way that the folded profile height is reduced to around $0.38h_0$. However, the inflection points (m_1 and m_2) that appear in the lens profile due to the folding introduce singularities that need to be optimized to keep the impedance matching (green dashed curve). To smooth out the singularities, chamfers can be implemented in the profile, see Fig. 4.5(b) red solid curve. In this representation, the green dashed curves are removed and are replaced by two lineal chamfers which avoid the singularity points. Fig. 4.5 (c) shows the reflection coefficient of the three lens profiles studied, where clearly the green dashed curve (lens profile without chamfers) has the worst behavior and is clearly improved when chamfers are added (red curve). For the sake of completeness, the normalized electric field distribution in the chamfered design is presented in Fig. 4.5(c) bottom.

Next, a folded complementary GLL with a radius equal to R = 4 λ_0, where λ_0 is the wavelength at 60 GHz (centered at the operation band), and a virtual focus at $8\lambda_0$ from the lens center ($r_i = 2R$) is designed, see Fig. 4.6(a). The lens is fed on the periphery using a WR-15 waveguide and a transition to fit the size of the lens PPW with the size of the WR-15 waveguide. This height needs to be fit because the gap between the parallel plates is selected to be below $\lambda_0/4$ (*gap* = 1 mm) to avoid higher order modes in the PPW and hence is smaller than the height of the WR-15 waveguide hollow. The transition is similar to the one used in [94] but in this case tuned at 60 GHz. Fig. 4.6(b) shows a full

wave simulation of the transition alone, where the reflection coefficient is below -20 dB over the operation bandwidth.

(a)

(b)
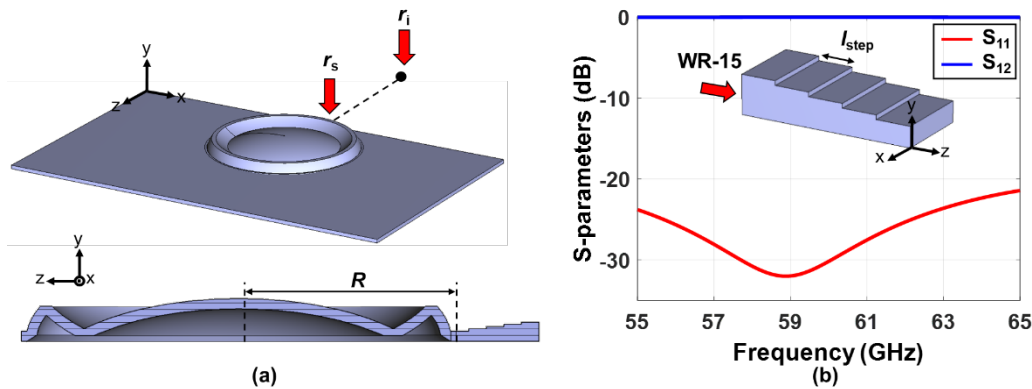
Fig. 4.6 (a) Schematic of a complementary geodesic lens with $r_i = 2R$ and $r_s = R$. Cross-sectional view of the geodesic complementary shape with $R = 4\lambda_0$ (b) S-parameters for transition between WR-15 and the input of the lens.

4.3.1   Phase center calculations

Up to this point, a complementary GLL with a compact height using two folds and fed by a WR-15 waveguide has been designed. This lens is designed to produce a virtual focus at a distance $2R$ from the center of the lens when the source is placed on the edge. This section is devoted to the evaluation of the lens performance, with the aim to ascertain the exact location of the virtual focus, so that it can be then aligned with the focus of the parabolic mirror. The scheme followed to perform this study is shown in Fig. 4.7(a). The idea is to obtain the electric field phase along a circumference of radius $6R$ centered at $-2R \pm 2\lambda_0$ (i.e. the expected virtual focus location $\pm 2\lambda_0$). The solid blue curve in Fig. 4.7(a) represents just the one case, $mov_{off} = 0$ where mov_{off} is the offset of the source with respect to the central position $-2R$.

The virtual focus will then correspond with the location where the phase along the circumference is nearly uniform, following the definition of phase center. The chosen circumference radius is long enough to ascertain with little error if the wave has a cylindrical wavefront.

79

As phase center could have variations according to the actual source used to feed the lens, two studies are made: first using a dipole as omnidirectional feed and then a waveguide port. The standard deviation is used to measure the amount of variation or dispersion of the electric field phase along the circumference. Obviously, a small standard deviation indicates that the values tend to be close to the mean. The calculation is done applying the definition of standard deviation:

$$\sigma = \sqrt{\frac{\sum_i^n (X_i - \bar{X})^2}{n}} \tag{4.4}$$

where $(x_1, x_2...,x_n)$ X_i are the observed values of the sample items, $\bar{X}$ is the mean value of these observations and n while the denominator N stands for the size of the sample. Therefore, the point where the standard deviation is minimum corresponds with the point where the phase is more uniform. Fig. 4.7(b) illustrates the standard deviation of 20 positions analyzed. The minimum appears when $mov_{off} = 0$ mm with a standard deviation of $\sigma = 7°$, demonstrating that the virtual image is obtained at $r_i = -2R$.
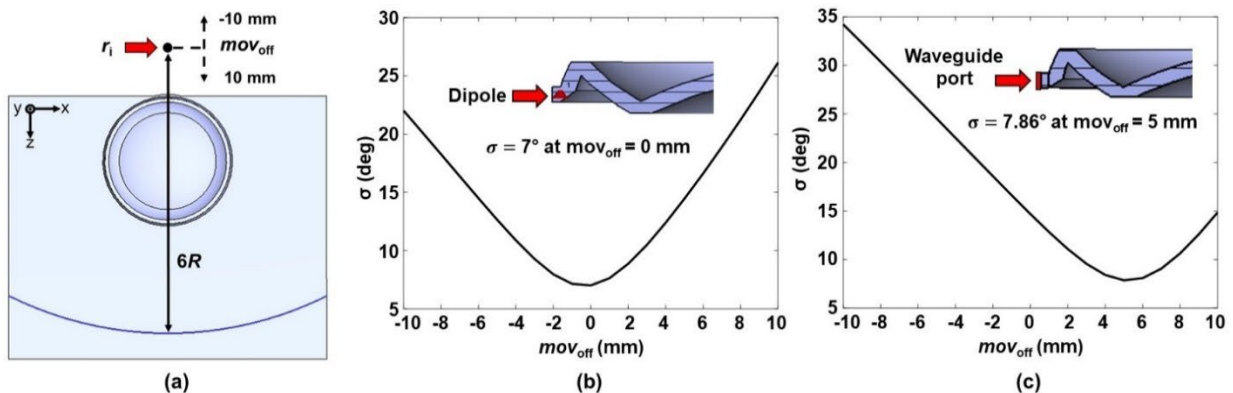
Fig. 4.7 (a) Schematic of a complementary geodesic lens phase validation, where mov_{off} is the displacement (in z-axis of ±10 mm) applied to the circumference center r_i and radius 6R. (b) Standard deviation study feeding with a dipole. (c) Standard deviation study feeding with a waveguide port.

A similar study is performed using a waveguide to feed the lens. Fig. 4.7(c) shows the standard deviation for the same positions analyzed. The flatter phase appears when $mov_{off} = 5$ mm (with $\sigma = 7.86°$), which means that the virtual image appears closer to the

lens, with a displacement of λ_0 with respect to the design position. This shift is caused by the waveguide port, whose phase center is not located exactly at its physical location. This shift will be considered in the reflector design to match the focal length. Now, the radius of the lens is the same ($R = 4\,\lambda_0$), but the virtual focus is at $7\,\lambda_0$ from the lens center due to the phase center calculations.

4.3.2   Spillover efficiency calculations

As mentioned at the beginning of the chapter, the main aim of the GLL is to illuminate a parabolic reflector whose focal lens matches with the virtual image and achieve beam scanning by using multiple sources along the lens circumference. It is clear that each source is associated to a particular virtual image that produces a different illumination on the parabolic reflector. Here, a spillover study is done by considering several source positions and from it the spillover efficiency of the entire system is obtained.

Fig. 4.8(a) shows a schematic of the setup used for spillover calculation using a waveguide attached to the transition designed before. Two main positions are analyzed, with the source position at 0° (symmetrical pattern) from the center of the lens, and at 45°. In this last position, although the lens's radiation pattern is symmetrical, the angle subtended from the parabolic mirror is not symmetrical and hence the integration limits are not symmetrical either (following the spillover formulation presented in [26]). Fig. 4.8(b) and (c) show the behavior for several some F/D ratios changing only F and keeping constant D, where F is the focal length and D is the diameter of the parabolic reflector, at 0° and 45° feeding positions. When the F/D ratio is between 0.57 to 0.75, the behavior is similar, achieving efficiencies around 88 to 96%. However, when $F/D = 1$, the efficiency decreases abruptly, being the worst case when the feed is at 45° feed. This can be explained by noting that for large F a large portion of the power is not intercepted by the reflector. Therefore, a value of $F/D = 0.75$ is selected as a compromise solution to design the final system because it has a good spillover efficiency in the operation band.
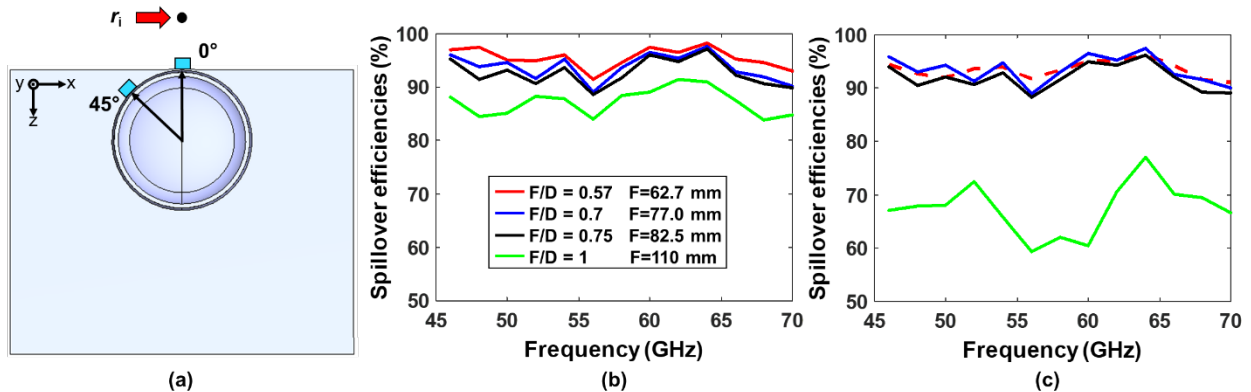
Fig. 4.8 (a) Schematic of a complementary geodesic lens spillover study of several *F/D* values. (a) Spillover analysis when the source is at 0°. (b) Spillover when the source is at 45°.

4.3.3 Compact pillbox reflector based on a complementary GLL

In this section, the entire system is designed and its performance analyzed. The sketch in Fig. 4.9(a) shows a parabolic reflector positioned at 9λ from the center to the complementary GLL with *F/D* = 0.75 and *D* = 22 λ_0 mm. The focal length of the parabolic reflector matches the virtual source location of the lens, determined by studying the phase center of the GLL. Eleven WR-15 waveguide ports are placed along the periphery to feed the GLL in order to achieve scanning angle capability. The separation between the center of each port is around 9.2°, taking as reference the center of the lens. Fig. 4.9(a) inset shows a profile view of the folded GLL.

As mentioned at the beginning of the chapter, the parabolic reflector is illuminated by the complementary GLL placed on the top layer (cyan). The wave travels along a PPW with height *gap* = 1 mm upon the parabolic mirror that has a corner reflector (two 45° chamfers in the cross section) to steer the wave to the bottom layer, see Fig. 4.9(b). Finally, the wave travels along the bottom PPW and is radiated in the air.
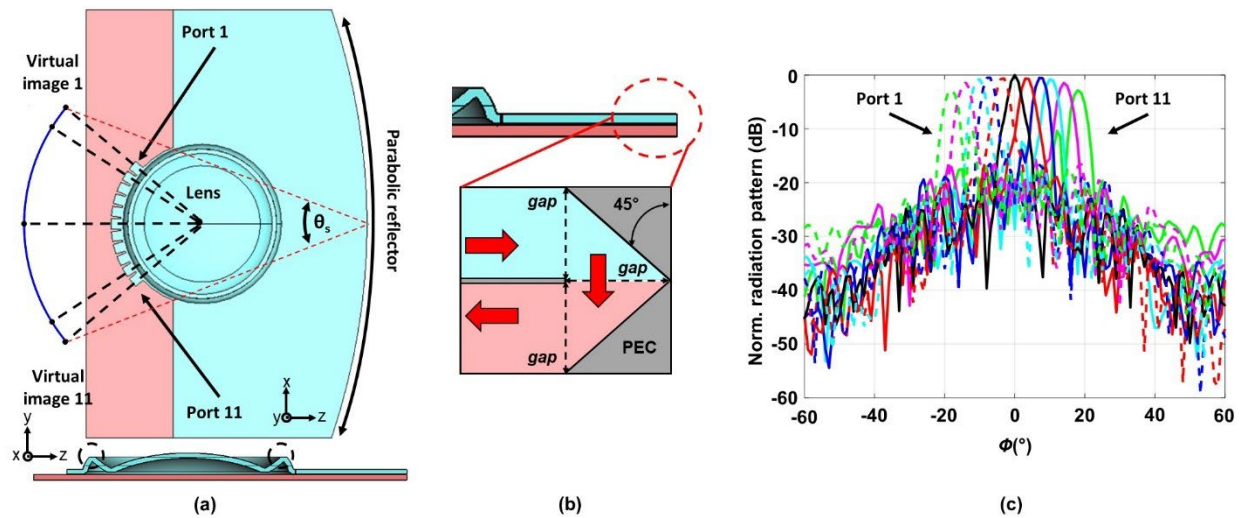
Fig. 4.9 (a) Schematic of a dual layer geodesic lens integrated with parabolic reflector: (a) Cross sectional view of both layers, where cyan represents the top layer and red the bottom one. (b) Detail of the corner reflector (c) Normalized radiation pattern of the dual layer geodesic lens integrated with the parabolic reflector.

Fig. 4.9(c) shows the normalized radiation pattern obtained for the entire system using CST Studio Suite® simulator for all the considered sources. The maximum scanning range is around ±18°. In addition, the directivity decreases by 2.6 dB in the maximum scanning angle close to 18°.
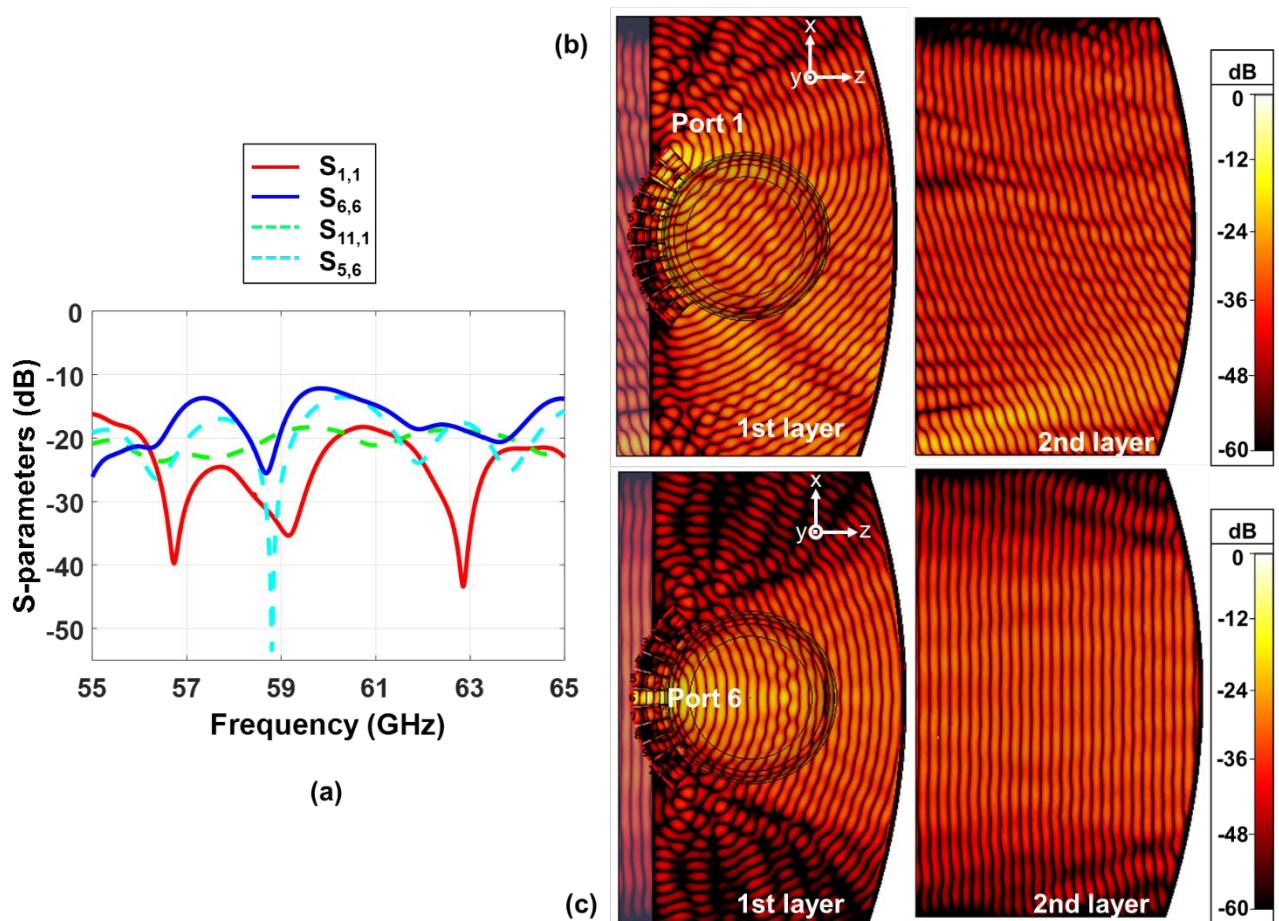
Fig. 4.10 (a) Reflection and coupling coefficients at some selected ports when the active ports are number 1 and 6. Top view of the electric field obtained with the numerical simulator considering the entire system at 60 GHz, 1st layer (left) and 2nd layer (right) when the excitation is done through (b) Port 1 and (c) Port 6.

To get a closer view of the system performance, the simulated S-parameters of ports 1 (extreme) and 6 (center) are presented in Fig. 4.10(a). Both have a reflection coefficient below −10 dB from 55 to 65 GHz. These ports were selected as they are an opposite case regarding possible cross-coupling between ports. Although not presented for the sake of clarity, the rest of the ports are also matched with S11 below −10 dB in all the considered band. A top and bottom view of the simulated electric field at 60 GHz when ports 1 and 6 are excited are shown in Fig. 4.10(b) and (c) respectively. As it can be

observed, a planar wavefront is generated at the output with a tilt angle that depends on the excitation source position.

4.4   Comparison with other reflector systems.

The motivation to include a GLL in the system is to achieve beam scanning using a parabolic reflector in a compact system. Here, a comparison is done with a simple parabolic reflector to evaluate the beam scanning. In addition, the system is compared with other classical solutions for compact reflector systems such as the Cassegrain reflector. Notice that the comparison shown below is made in terms of size, scanning angle, directivity and SLL in order to determine how compact the GLL system is compared to classical solutions. In the Cassegrain reflector system case, given the number of design variables, the study presented in this thesis is not exhaustive and the comparison is done for only two representative cases. A comprehensive analysis may be the subject for a better optimization process to obtain a more exhaustive and detailed comparison in the future.

In the next subsections, the analysis of a classic parabolic reflector and two different configurations of a Cassegrain reflector system are presented. After that, the most relevant results are simulated in CST Studio Suite® in order to establish a comparison with the GLL.

4.4.1   Classical parabolic reflector

The first case analyzed is a classical parabolic design, with the same dimensions as the devised pillbox-antenna. The parameters evaluated are directivity, SLL, and scanning range. Initially, in order to perform a fast analysis all these parameters are calculated using an in-house ray-tracing program, see appendix A.

The problem under consideration is illustrated in Fig. 4.11(a) with the origin of coordinates placed at the vertex of the parabola. The rays emitted from a horn feed (denoted as p_s and modelled with a cosine radiation pattern) reach the parabolic reflector

which has a focal distance $F = 17\lambda_0$ and a diameter D, with $F/D = 0.75$. To avoid the blockage effects, a dual-layer (pillbox system) reflector is assumed. The black and red arrows denote the first and the second layer, respectively.

The beam scanning is realized by moving and rotating the feeding source off the focus, so that it always points to the parabola center. This leads to a beam deviation in the radiation pattern [137]. In the analysis below, the source is moved inside the boundaries of the gray box shown in Fig. 4.11(a) defined by $\pm D/2$ ($D = 110$ mm) and $p_s \pm x_{mov}$ (where $x_{mov} = 10$ mm is the maximum horizontal displacement proposed from the focal point, $p_s = -82.5$ mm).
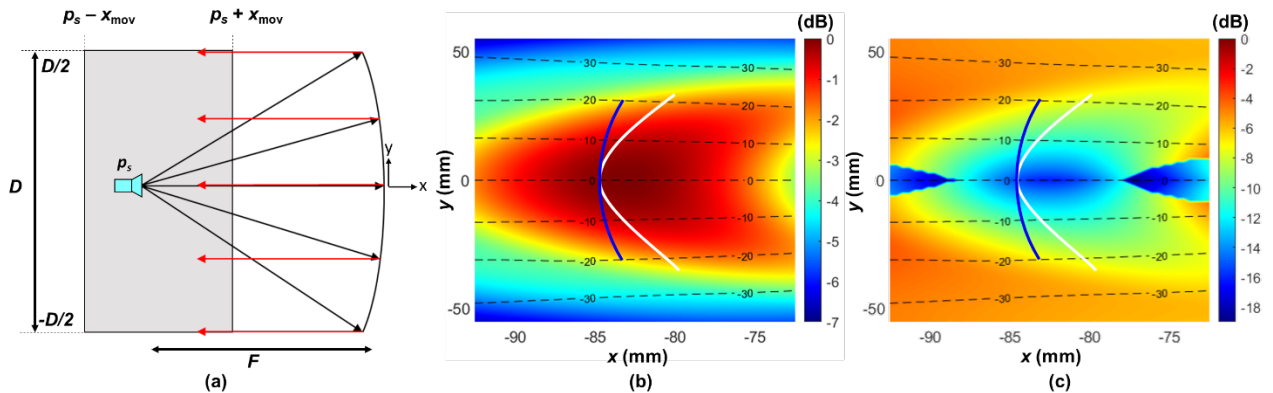
Fig. 4.11 (a) Schematic of the analyzed problem with a horn feed illuminating a parabolic reflector. The black rays represent those in the first layer and the red ones those in the second layer. (b) Contour plot of the normalized maximum of the radiation pattern (in dB) as a function of the position of the feed along x and y (the analysis is restricted to the gray area shown in (a)). (c) SLL in dB with respect to the maximum. The dashed lines in (b) and (c) represent the angle of the main beam after reflection by the parabolic mirror. The white curves in (b) and (c) approximate the optimal positions for the feed and the blue curve is the arc followed for the geodesic shape with a virtual source at $2R$.

Fig 4.11(b) shows a contour plot of the normalized (to the maximum of the broadside beam) radiation pattern maximum as a function of the source position, varied along x and y in steps of 0.5 mm within the gray area. The dashed lines indicate the main beam in azimuth direction. The maximum directivity values appear near the focus. However, if the feeding source is moved away from the focus the directivity decreases. It happens due to

the phase aberration introduced by placing the feed out of the focus which degrades substantially the far-field pattern, and depends very strongly on the *F/D* ratio. Likewise, Fig. 4.11(c) shows the SLL in dB. The behavior is similar to the directivity results: close to the focus, the SLL is below −10 dB and increases when the source is displaced from that point. From these graphs, it is found heuristically that to achieve the greatest possible scanning angle while maintaining a high directivity and low SLL, the feeding source should move approximately along the white curve shown in Figs. 4.11(b) and (c).

4.4.2   Classical Cassegrain reflector system

Now a comparison with a Cassegrain reflector system is done, considering two different configurations, with a big sub-reflector (as explained below) and another with a smaller one at a distance below 12 λ_0 to get a compact system.

The Cassegrain dual-reflector system consists of a larger (main) reflector that must be a paraboloid and a smaller (secondary) reflector which could be a hyperboloid or an ellipsoid, see Fig. 4.12(a). The use of a second reflector, which is usually referred to as the sub-reflector or sub-dish [138], gives an additional degree of freedom for achieving compact systems in a number of different applications (such as terrestrial communication satellite antennas, radio telescopes, and the antennas of some communication satellites).

Typically, in antenna design, the parameters to consider when developing a Cassegrain system are: the diameter of the main reflector (*D*), the focal length of the main reflector (*F*), the focal length of the sub-reflector (F_c), and the feeding beamwidth of the sub-reflector (Φ_r). The rest of the design parameters, such as the diameter (D_c) and the eccentricity (e_c) of the sub-reflector, are dependent on these and can be calculated following the formulation presented in [138]. Since the objective is to compare the GLL and the classic parabolic reflector, *F* and *D* will be considered fixed parameters. Therefore, the optimization parameters will be F_c and Φ_r. To simplify the analysis, it was decided to set $F_c = F = 82.5$ mm and only modify the sub-reflector with the Φ_r parameter. This has as a direct consequence that the best performance of this system (in directivity

terms) is when the feeding source supply is located at the vertex of the main reflector $p_s(0;0)$.

The first configuration tries to maximize the size of the sub-reflector. This way, it is possible to intercept most of the rays emanating from the source even form large angels. For this purpose, Φ_r was fixed to 70° which results in a sub-reflector diameter D_c=97.2 mm, near the diameter of the main reflector (D = 110 mm). Following the equations shown in [138] for a classical Cassegrain the sub-reflector shape is elliptical.

Fig. 4.12(a) shows the configuration proposed, where the elliptical sub-reflector is close to the horn feed and the same parabolic reflector considered above. As before, the origin of coordinates was placed at the vertex of the main parabola which the rays emitted from the source p_s reach the elliptical sub-reflector placed at – 26.6 mm.

The beam scanning was realized by moving the feeding source within the boundaries of the gray box shown in Fig. 4.12(a) and rotating it so that it pointed always towards the sub-reflector center. To analyze the behavior of the Cassegrain system and keeping the same notation used in the classical parabolic reflector, the gray box limits are:

- Along x-axis: p_s + 5 mm in positive and p_s – 2 mm in negative direction.
- Along y-axis p_s ± 35 mm.

(a)   (b)   (c)
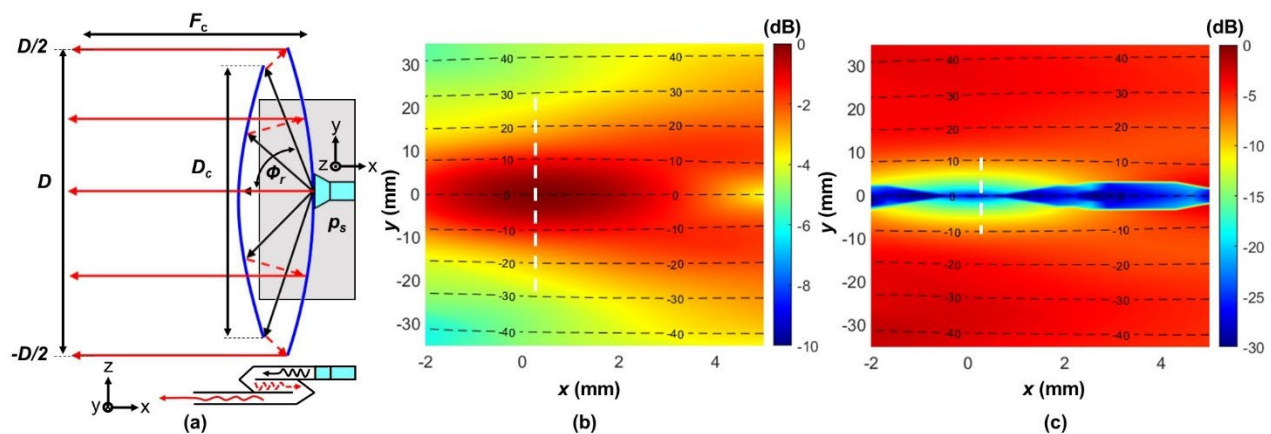
Fig. 4.12 (a) Schematic of the first problem analyzed with a horn feed illuminating a Cassegrain reflector. Inset, cross-sectional view where the black rays represent those in the first layer, the red dashed rays those in the second layer, and the solid red rays those the third layer. (b) Contour plot of the normalized radiation pattern (in dB) as a function of the position of the feed along x and y [the analysis is restricted to the gray area (a)]. (c) SLL in dB with respect to the maximum. The dashed lines in (b) and (c) represent the angle of the main beam after reflection by the parabolic mirror.

Using the ray-tracing method (Appendix A), a study of directivity, scanning angle and SLL was realized. Fig 4.12(b) shows a contour plot of the normalized (to the maximum of the broadside beam) radiation pattern as a function of the source position, varied along x and y in steps of 0.5 mm within the gray area.

The maximum directivity values appear near the focus and decrease if the feeding source is moved away from the focus. However, the scanning capability is increased compared to the GLL and single parabolic reflector (see the dashed lines), achieving a maximum scanning range around ±30° [this is an approximate result assuming that the source moves along the dashed white line illustrated in Fig. 4.12(b)]. Another criterion to evaluate the performance is having a maximum SLL of −10 dB. According to Fig. 4.12(c), when the feeding source is moved away from the focus, the SLL increases rapidly. Thus, this parameter limits the scanning range of the system to ±12°, see Fig 4.12(c) white dashed line.

A second configuration is evaluated, this time with a smaller sub-reflector. The new Cassegrain system is presented in Fig. 4.13(a). In this case, the same criteria are maintained, where $F_c=F$ and Φ_r controls the shape of the sub-reflector with a reduced beam width to optimize the illumination. So, $\Phi_r = 50°$ and the diameter of the sub-reflector is modified to $D_c=75.9$ mm. Due to the modification of the diameter, the position of the sub-dish is now −34.4 mm. The gray box boundaries have the same size as before.
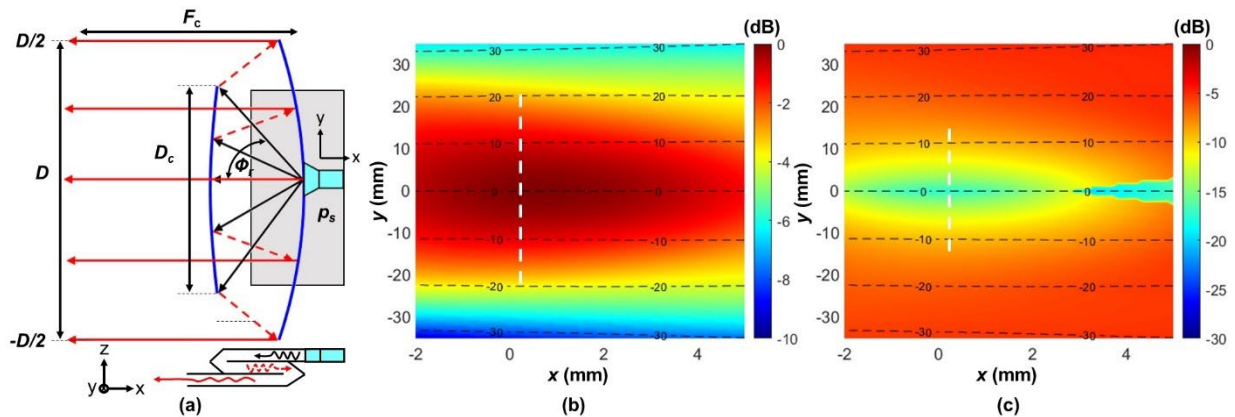
Fig. 4.13 (a) Schematic of the second problem analyzed with a horn feed illuminating a Cassegrain reflector. Inset, cross-sectional view where the black rays represent those in the first layer, the red dashed rays those in the second layer, and the solid red rays those the third layer. (b) Contour plot of the normalized radiation pattern (in dB) as a function of the position of the feed along x and y [the analysis is restricted to the gray area (a)]. (c) SLL in dB with respect to the maximum. The dashed lines in (b) and (c) represent the angle of the main beam after reflection by the parabolic mirror.

The directivity behaves similarly as in the previous cases. In this case, the scanning angle goes up to ±20°, see dashed white lines Fig 4.13(b). Fig 4.13(c) shows the SLL results. It is clear that again the SLL increases abruptly as the source is shifted from the focal point, limiting the scanning range of the system to ±14°, see Fig 4.13(c) white dashed line.

These two configurations demonstrate the improved scanning capability of the Cassegrain system compared with the parabolic reflector and the GLL. Nevertheless, the high SLL values when the source is moved out of the focal point represents a limitation for this structure compared to the GLL system. In addition, although the Cassegrain reflector is more compact than the parabolic reflector and the GLL (in *x*-axes), it is necessary to fabricate it in three vertical layers to avoid blockage effects. This an increased degree of complexity compared to the GLL system.

4.4.3   Comparison results using numerical simulations

In this section a full-wave numerical comparison between a classical parabolic reflector and the proposed compact pillbox reflector GLL antenna is done. The Cassegrain system is not analyzed due to the high SLL foreseen in the previous study.

In the numerical simulations, the source point p_s (whose radiation pattern was modelled with a cosine) is replaced by a waveguide that is a good approximation to that radiation pattern. The results of the numerical simulations of the GLL system and the parabolic reflector alone are presented in Fig. 4.14(a) and (b), respectively. For the sake of completeness, this last case is compared with the ray-tracing calculation, Fig. 4.14(c).

The maximum length in the classical parabolic reflector is around $17\lambda_0$, while the GLL solution is more compact, around $12\lambda_0$. Due to the symmetry of the GLL, the virtual sources are located along a circumference centered at the center of the GLL, represented as a blue curve in Fig. 4.11(b). The numerical simulations give a beam scanning of the GLL system around ±18° with a directivity drop of 2.59, dB, Fig. 4.14(a). Beyond that angle, with the angular precision available determined by the size of the waveguides attached to the GLL, the directivity drops more than 3 dB. Using the same arc to illuminate the parabolic reflector [blue curve in Fig. 4.11(c)] the scanning range taking only the criterion of −3 dB of directivity drop would be of ±28°. Nevertheless, for angles beyond ±18.2° the SLL rises above −10 dB, see figures. 4.14(b), (c) where the maximum scanning angle is very close to this criterion. Thus, in practical terms, the maximum scanning range is ±18.2°.

The larger directivity drops of the GLL system compared to the single parabolic reflector at ±18° can be explained by noting that the output wave in the GLL case only points towards the center of the parabolic mirror when the source is in the central position; otherwise, the output wave points in a different direction, as presented in Fig. 4.10(b). In contrast, in the case of the parabolic reflector alone a horn antenna can be placed so that it points to the center of the parabolic reflector in whatever position. The worst case in the GLL configurations happens for a beam scanning angle of 18° where SLL is equal to -

14.5 dB. For the classical parabolic reflector, it happens for a beam scanning angle of 18.2° where SLL is equal to -10.6 dB.
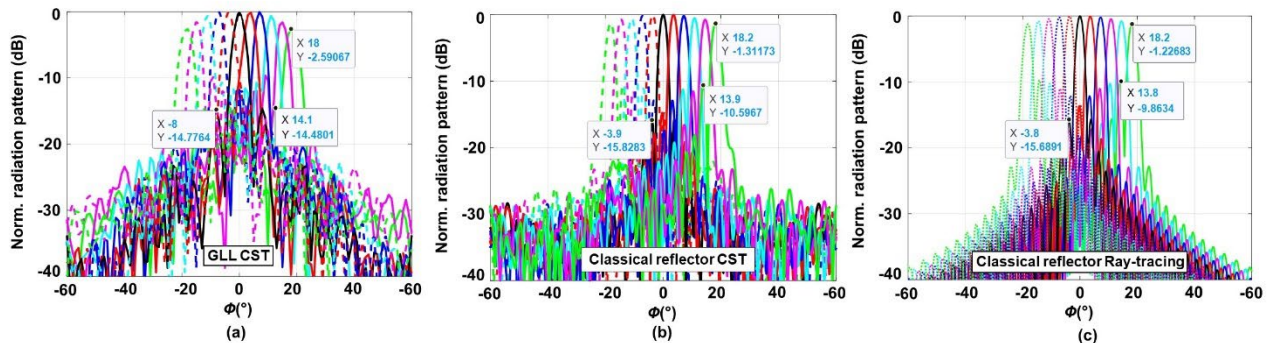
Fig. 4.14 Normalized radiation pattern comparison between the: (a) complementary GLL and (b) classical parabolic reflector in a dual layer implementation using CST Studio Suite® and (c) ray tracing implementation using an in-house program.

4.5 Conclusions

To sum up, in this chapter, a system combining a dual-layer Luneburg geodesic lens with a parabolic reflector system to produce a compact antenna has been demonstrated. First, the concept of GLL has been introduced and the extension to complementary GLL discussed. To get a more compact structure and improve impedance matching, two folds and chamfers have been introduced in the design of the GLL. Then the GLL has been inserted in a pillbox structure to illuminate a parabolic reflection. The resulting lens-antenna system has been simulated, analyzing first the phase center location and the spillover efficiency. The results achieved for the structure are excellent, with a beam scanning around ±18° using 11 ports distributed around the periphery of the lens. Furthermore, a good matching is obtained within the entire operation band.

Finally, a comparison between the complementary GLL, a classical parabolic reflector, and a Cassegrain reflector system has been performed. The radiation pattern

characteristics have been analyzed by using an in-house ray-tracing code and the main results have been corroborated with numerical simulations.

A comparison with two Cassegrain reflector systems has been carried out. According to the ray tracing calculations, the system with a big sub-reflector has a broad scanning range of ±30°, but the SLL limits it to ±12°. A second configuration, has been tested, this time fixing the same scanning range as the GLL system. Again, it has been observed that side lobes limit the performance to ±14°. Thus, Cassegrain systems can lead to more compact systems compared to the GLL solution but more research is needed to settle more solid conclusions.

In the classical parabolic reflector case, a thorough numerical study has been performed and it has been found that the GLL systems is compact with a good directivity and scanning range. The GLL system presents a size reduction of $5\lambda_0$ (30%) compared to the classical parabolic reflector. These results open new opportunities for directive antennas using fully metallic designs at millimetre-waves and terahertz frequencies.

Chapter 5: Homogenous Hyperbolic Lens Antenna in Groove Gap Waveguide

5.1. Introduction

Terahertz and sub-millimetre wave technology are attracting significant research interest due to the wide available bandwidth and a short wavelength that provides high resolution with modest apertures. Hence, among the most popular applications one finds high-resolution radars, imaging systems, sensing, security screening, and high-speed communications [139]. However, the design and implementation of antennas at these frequencies is challenging due to the limits in fabrication processes, small dimensions and strict tolerances. An interesting idea is to combine classical lens designs with the GW technique studied in this thesis.

In this chapter, a hyperbolic metamaterials lens is designed at 300 GHz using GGW technology, already presented in a previous chapter of this thesis. A GGW horn antenna is used to feed the lens and the system is designed to achieve a planar wavefront at broadside. The implemented metamaterial lens follows a hyperbolic profile, and consists of a bed of nails designed with uniform pin height to get a homogenous refractive index. Both devices, the metalens and the GGW H-plane horn antenna achieve excellent radiation results when combined together.

5.2 Hyperbolic lens and horn antenna design

The main advantages of using classical lens shapes such as hyperbolic and elliptical profiles are that they can be designed following analytical formulas, have a simple form and therefore easier development. The equation to get the geometry of a plano-convex lens can be expressed in polar coordinates as:

$$\rho(\psi) = \frac{(n_{eff} - 1)F}{n_{eff} \cos \psi - 1} \tag{5.1}$$

where ρ is the radial component, ψ is the angular component, n_{eff} is the refractive index of the lens and F is the focal distance between the lens and the focal point. It is evident that lens profile is governed by the magnitude of n_{eff} in (5.1): when $n_{eff} < 1$ the resulting curve is an ellipse and when $n_{eff} > 1$ is a hyperbola [140]. Fig. 5.1(a) illustrates the main geometrical parameters of a hyperbolic metalens (HL), which is the profile selected in the proposed lens antenna system.
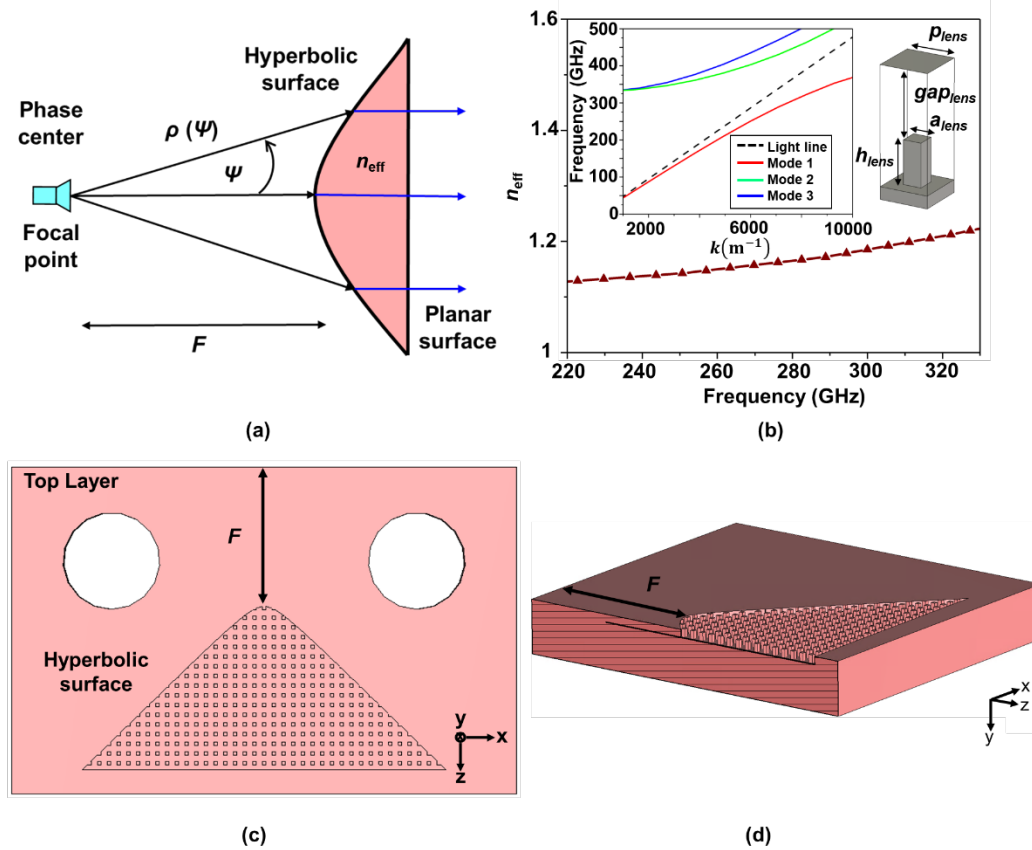
Fig. 5.1 (a) Geometry of the HL. (b) Equivalent refractive index of a periodic metallic pin array structure. The inset shows a dispersion diagram of a metallic pin unit cell with the following dimensions: p_{lens} = 0.16 mm, a_{lens} = 0.06 mm, h_{lens} = 0.121 mm and gap_{lens}=0.35 mm. (c) HL top layer, where F = 2.3 mm is the focal length. (d) Cross-section view of the HL.

To avoid dielectric loss which could be high at the design frequency of 300 GHz, here a metalens based on a metallic pin array is proposed. Unlike the LL studied in Chapter 3 a constant refractive index is implemented here, because the 2D hyperbolic profile converts the cylindrical wave emerging from the focal point into a plane wave [Fig. 5.1(a)] based only on the lens profile, without needing a gradient index for the lens material. As it was done in Chapter 3, the dispersion characteristics of the unit-cell were by employing the eigenmode solver of CST Studio Suite®. Fig. 5.1(b) inset shows the dispersion curves obtained with metallic pin unit cell with height h_{lens} = 0.121 mm, width a_{lens} = 0.06 mm, period p_{lens} = 0.16 mm and gap_{lens}=0.35 mm. A monomode propagation with a linear,

almost non-dispersive behavior in a large bandwidth within the considered frequency range is achieved, making this unit-cell a suitable candidate for the realization of the lens. The effective refractive index n_{eff} is then retrieved using $k_x = n_{eff}k_0$. In the operation band it is between 1.1 and 1.2, see Fig. 5.1(b). Finally, fixing F = 2.3 mm the hyperbolic profile shown in Fig. 5.1(c) and (d) is obtained by solving (5.1).

The next step is to design the GGW horn antenna feeding the HL. Notice that it must be ensured that the wave is confined within the groove of width 0.84 mm and height 0.35 mm by the metallic pins of the GGW structure and the top and bottom metallic plates. Again, the eigenmode solver of CST Studio Suite® was employed to obtain the pin dimensions that ensure a bandgap in the operation bandwidth. As shown in Fig. 5.2(a), with a width of a_{horn} = 0.1 mm, a height of h_{horn} = 0.3 mm, periodicity p_{horn} = 0.2 mm and distance to the upper metallic layer of 0.05 mm, a bandgap arises centered at 300 GHz and spanning from 200 to 386 GHz. Fig. 5.2(b) shows the dispersion diagram of the GGW infinite along the z-direction consisting of three rows of pins at each side with a central groove of width 0.84 mm, separated from the upper lid by the air gap of 0.05 mm. The mode inside the GGW is similar to the TE_{10} mode of a standard waveguide and is confined inside the groove the metallic pin array stopband (205 to 355 GHz), where higher-order modes are in cut-off, Fig. 5.2(b).

(a) (b) (c)
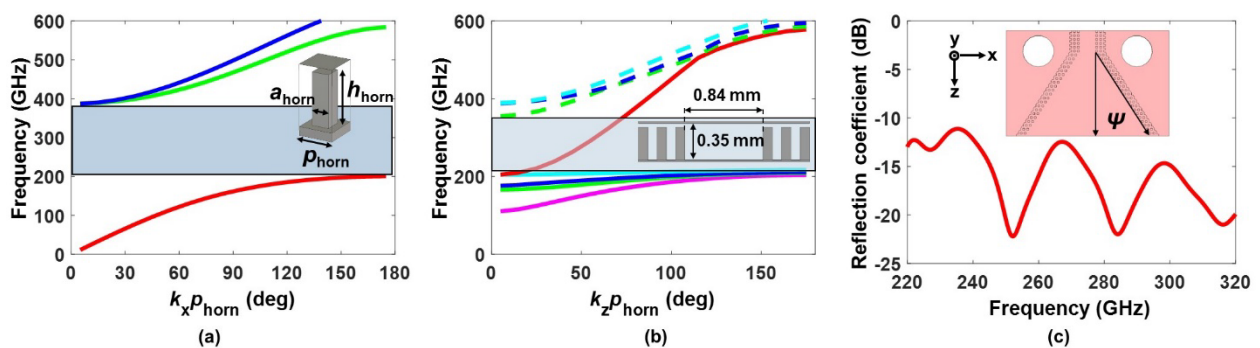
Fig. 5.2 (a) Dispersion diagram of a periodic metallic pins structure (shown in the inset) with dimensions: p_{horn} = 0.2 mm, a_{horn} = 0.1 mm and h_{horn} = 0.3 mm. (b) Dispersion diagram of a GGW with three rows of pins at each side and a central groove of 0.84 mm (c) Simulated input reflection coefficient of the GGW horn antenna in dB; (Inset) top view showing the horn flare angle (Ψ = 34°).

Using these dimensions for the GGW pins, the H-plane horn was designed optimizing the waveguide opening with a linear variation, and an angle of ψ = 34° for operation at 300 GHz. Fig 5.2(c) shows that the input reflection coefficient is below −10 dB from 220 GHz to 320 GHz.

The horn antenna and the HL were analyzed together, see Fig. 5.3(a) and (b). Usually, in metalens designs, the lens and feeding are in the same layer. However, the pins of the lens and the antenna have different the height increasing the manufacturing complexity considerably. For example, to manufacture the structure in a single layer different films of photoresist to protect each etching should be employed, increasing the error due to the selectivity of the photoresist (see Appendix B). In the proposed solution, the HL and the horn were implemented in different silicon substrates so that they can be fabricated independently. This way, the HL can be placed on the top and the horn antenna on the bottom layer to simplify the manufacturing process. Another method could be to implement a variable dose in the exposition procedure in order to obtain the required height difference between pins. However, this would require a long exposition time and a complex configuration in the exposition machine.
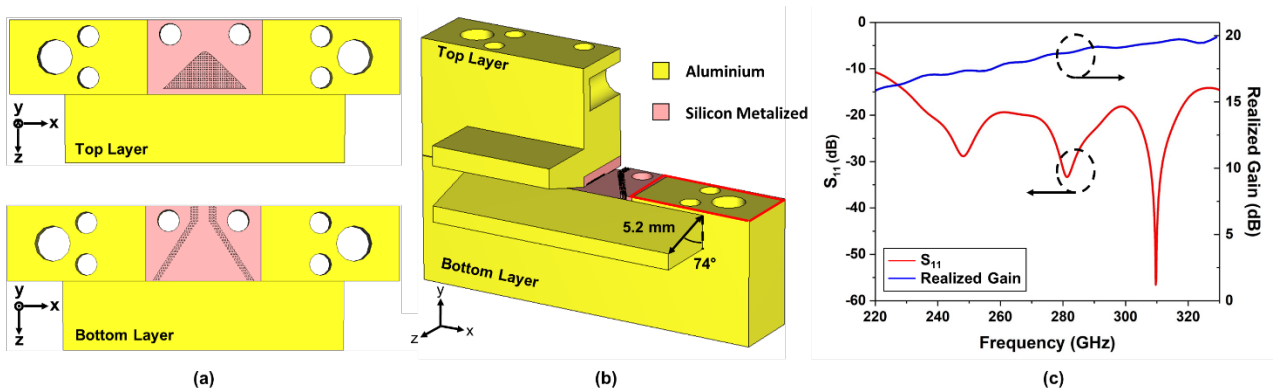
Fig. 5.3 (a) (Top) HL top layer; (bottom) GGW horn antenna bottom layer. (b) Encapsulated of a horn GGW antenna plus hyperbolic lens system. (c) Simulated results of the structure. Magnitude of the reflection coefficient in dB (red curve) and realized gain (blue curve) vs frequency.

The numerical analysis of the entire system using CST Studio Suite® was performed. Fig 5.3(b) shows the design setup: two aluminum blocks are used to host and sandwich the metallized micromachined Si pieces with the HL and the GGW. Each aluminum block presents a flared section to achieve a smooth air transition. The PPW opens gradually with an angle of 74°, and its length is 5.2 mm. The lens and GGW horn antenna layers are colored differently, because their manufacture is foreseen by means of silicon micromachining and metallization, in contrast to the encapsulation blocks. Two thin silicon spacers [red square in Fig. 5.3(b)] of a height of 0.05 mm are placed to fix the gap between the pins and top layer satisfies the condition ($gap_{horn} < \lambda_0/4$, where λ_0 is the wavelength at the central frequency). In addition, these spacers fix the metalized Si layer to avoid displacement in the structure. Note that gap_{horn} is different to gap_{lens}, as this last one is defined by the depth of the GGW horn antenna ($gap_{lens} = h_{horn} + gap_{horn}$).

Due to the high frequency considered, losses in the metal parts must be carefully considered. In this case, the aluminum is modelled with an effective conductivity corresponding to its nominal direct current conductivity divided by a factor of 6, to model imperfections such as roughness, etc. Therefore $\sigma_{Al,eff} = 5.93 \times 10^6$ S/m. To emulate the experimental setup, the system is feed by a standard WR-3.4 waveguide. Fig. 5.3(c) shows the input reflection coefficient (red curve) and the realized gain (blue curve) as a function of frequency. The antenna is matched in the entire operation band (from 220 to 330 GHz), with the criterion of having a reflection coefficient magnitude below −10 dB. The prototype presents a high gain with a maximum around 20 dB at 325 GHz, see Fig. 5.3(c) blue curve.
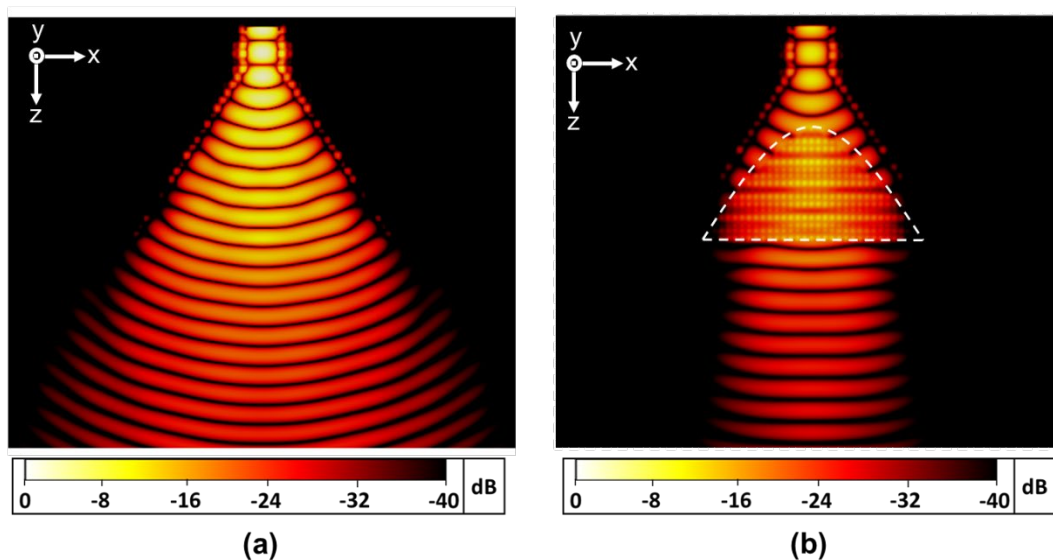
Fig. 5.4 Simulation of (a) Normalized $|E_z|$ without HL and (b) normalized $|E_z|$ at 300 GHz in decibel scale.

Moreover, Fig. 5.4 (a) and (b) show a comparison of the normalized vertical component of the electric field from a top view of the antenna with and without HL at 300 GHz. It is clear that a planar wavefront at broadside is achieved when the HL is included in the design. Therefore, it can be concluded that the GGW horn antenna provides a good radiation characteristic which, when combined with the HL, leads to an improvement of the radiation characteristics maintaining a compact setup.
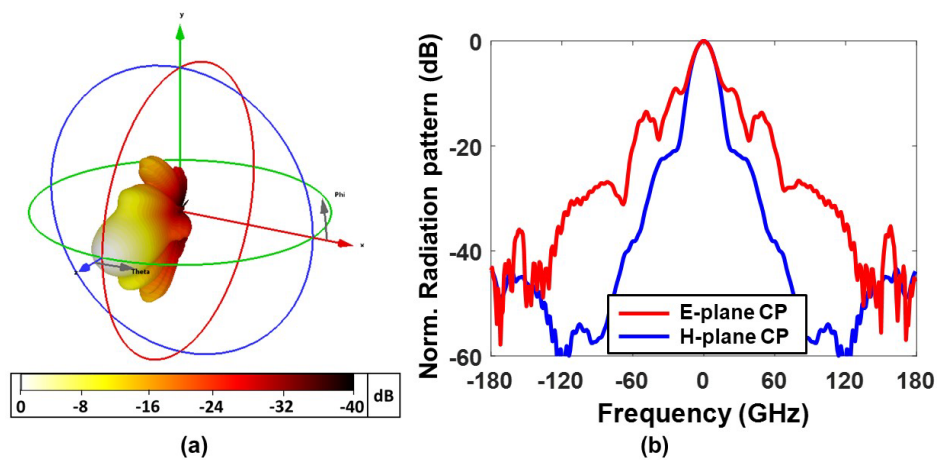
Fig. 5.5 (a) Simulated 3D radiation pattern of a horn antenna system using a metalens HL at 300 GHz. (b) Normalized far field radiation patterns obtained in simulation at 300 GHz, where the red and blue lines correspond to E and H-planes copolar components, respectively.

Fig 5.5(a) illustrates the radiation pattern of the lens antenna system using an metalens HL at the same frequency (300 GHz), with a similar beamwidth in the H and E-plane (H_{HPBW} = 16.6° and E_{HPBW} = 16.8°). The normalized radiation pattern at the same frequency in Cartesian coordinates (Fig. 5.5(b)) clearly shows the similarity of both beamwidths. The side lobe level in H- and E-plane at 300 GHz is around −22 dB and −9.1 dB, respectively.

5.3 Teflon lens design

A hyperbolic shape using Teflon is analyzed to compare its performance with the previous metalens using the same the H-plane horn antenna to feed the lens. Following eq. (5.1) a hyperbolic dielectric lens is designed using Teflon, see Fig. 5.6(a). Notice that this new implementation has a modified focal length from F= 2.3 mm to 2.9 mm to cover the volume in the horn antenna and avoid any intersection with the horn pins. In addition, the dielectric lens is not into the top layer but fills the volume between the bottom and top layer (d = 0.35 mm). The Teflon used has been modelled with a permittivity ε_r = 2.1 and a loss tangent $\tan\delta$ = 2·10^{-4}.

(a) (b) (c)
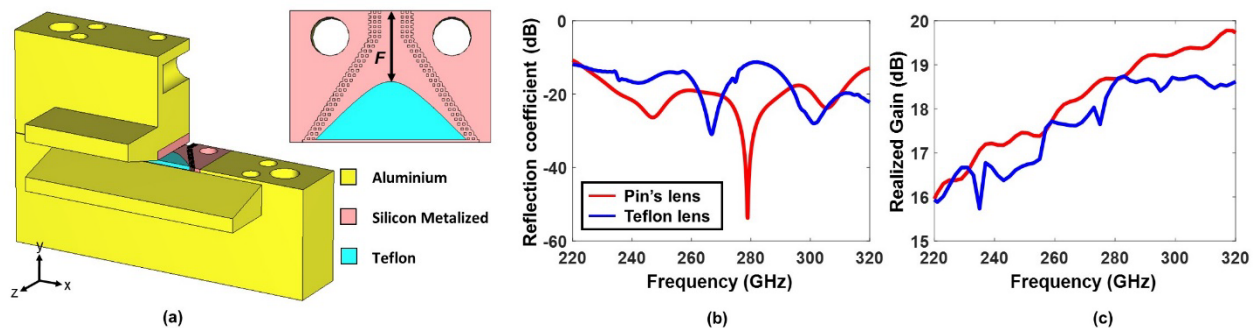
Fig. 5.6 (a) Encapsulated view of a horn GGW antenna plus hyperbolic dielectric lens system. The inset shows a top view of the dielectric lens placement, with *F*=2.9 mm. Simulated comparison results of the structure with metalens (red curve) and dielectric lens (blue curve). (b) Magnitude of the reflection coefficient (c) Realized gain.

Fig. 5.6 (b) and (c) show the reflection coefficient and realized gain for both cases, where the solid red curve corresponds to the antenna with metalens and solid blue curve to the antenna with Teflon (dielectric) lens. The reflection coefficient results show differences between both lenses, although both prototypes have good matching within the entire band. However, in the Teflon lens case, the realized gain curve has a similar behavior with respect to the case with metalens, but it presents some irregularities. These irregularities are attributed to a hard transition from the waveguide cavity to the dielectric material. In order to realize a smooth transition a matching layer process is added.

Fig. 5.7(a) shows the new HL design, this time with a matching layer surrounding the lens to achieve a smooth wave transition. Calculating a $\lambda_0/4$ transformer, the permittivity value of the new material is found. In this case, the impedance is:

$$\varepsilon_{\lambda_0/_4} = \sqrt{\varepsilon_{Teflon}} \qquad (5.2).$$

(a)   (b)   (c)
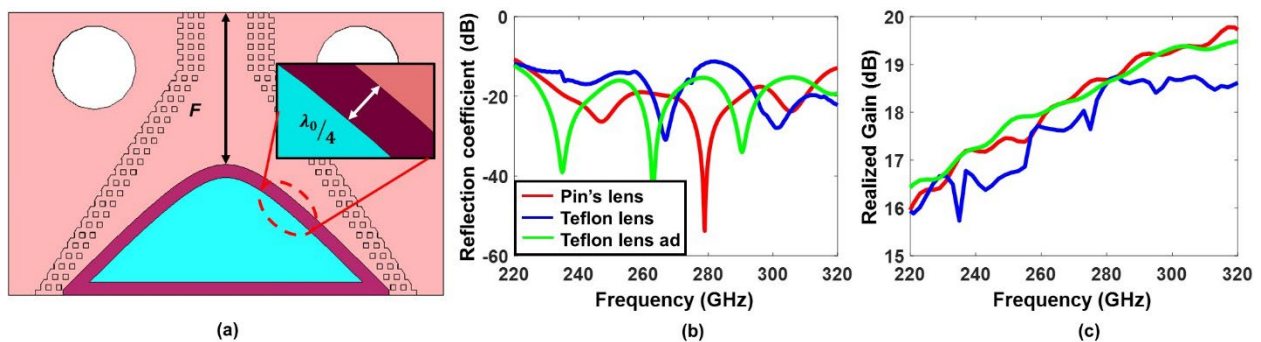
Fig. 5.7 (a) HL top layer using Teflon plus a $\lambda_0/4$ impedance transformer, where F = 2.9 mm is the focal length. Simulated comparison results of the structure with metalens (red curve), dielectric lens (blue curve) and dielectric lens with $\lambda_0/4$ matching layer (green curve). (a) Magnitude of the reflection coefficient (b) Realized gain.

Fig. 5.7(b) and (c) show a comparison between the lenses designed, where the new one with the matching layer is represented with a green solid curve. The new reflection coefficient is better than the original Teflon lens and does not present irregularities in the realized gain parameter. Furthermore, the realized gain is cleaner and more similar to the metalens case.

5.4   Lenses comparison

In this section a comparison of the designed lenses is performed and both are compared with the antenna design without lens. Fig. 5.8 shows the reflection coefficient, and realized gain for all the considered cases metalens (red), matched Teflon lens (green), and horn antenna (black). The simple Teflon lens was discarded because the lens with matching layer has a better behavior.
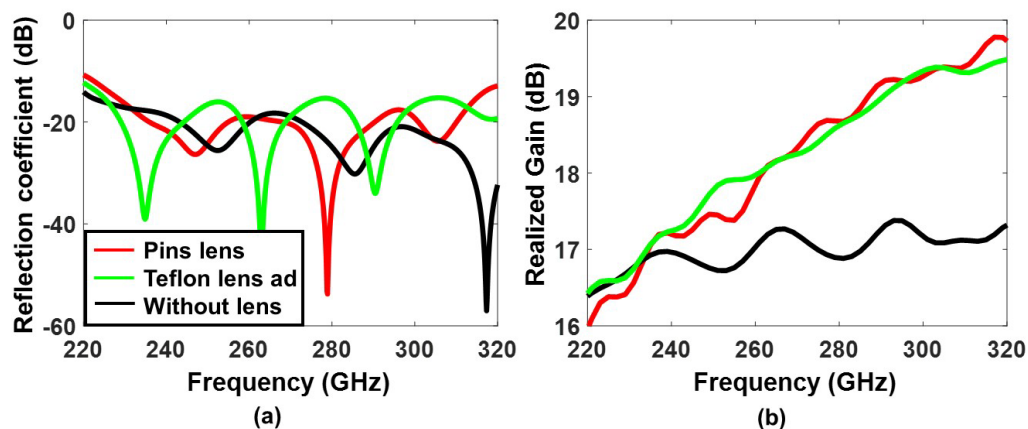
Fig. 5.8 Simulated comparison results of the structure with metalens (red curve), dielectric lens with $\lambda_0/4$ matching layer (green curve) and without lens (black curves). (a) Magnitude of the reflection coefficient (b) Realized gain. (a) Encapsulated

The reflection coefficient results shown in Fig. 5.6(a) do not show significant differences, with all the prototypes having a good matching within the entire band. However, the realized gain shows an improvement of around 3 dB for frequencies above 260 GHz for both lenses compared to the horn antenna alone, see Fig. 5.8(b).

An important conclusion that can be drawn from these results is that the metalens and the matched Teflon lens have almost an identical performance. Nevertheless, the $\lambda_0/4$ transformer needed in the latter lens to get good radiation characteristics makes the manufacturing process cumbersome. First, the dielectric material must match with the required exact permittivity value, have low losses at 300 GHz and a precise thickness of 0.23 mm thickness. In addition, a demanding manufacturing process is necessary to integrate both pieces keeping a hyperbolic shape without undesired air gaps caused by bad contact or misalignment that can lead to resonances or frequency detuning. Another alternative to get impedance matching with the Teflon lens could be by making steps in a lens border, but this solution would make the manufacturing process even more complex. For these reasons, the design of a metalens seems the best option because it is compact, is immediately matched, and gives more robustness due to its fully metallic composition.

5.5 Manufacturing process

The manufacturing process of the metalens HL was divided into two steps. First, the two aluminium blocks (used to host and sandwich the metallized Si wafers with the HL and the GGW) were fabricated in aluminium using CNC. Fig. 5.9(a) shows a profile view of the manufactured pieces, where the top and bottom layers are finished in a flare structure to guarantee a smooth transition to the air and symmetrize the beam; see the details in Fig. 5.9(a). The blue dashed circles drawn in Fig 5.9(b) and (c) are screw holes,

and the red ones are alignment pin holes. The green dashed square delimits the area where the metalized silicon pieces (HL and GGW horn antenna) will be placed.
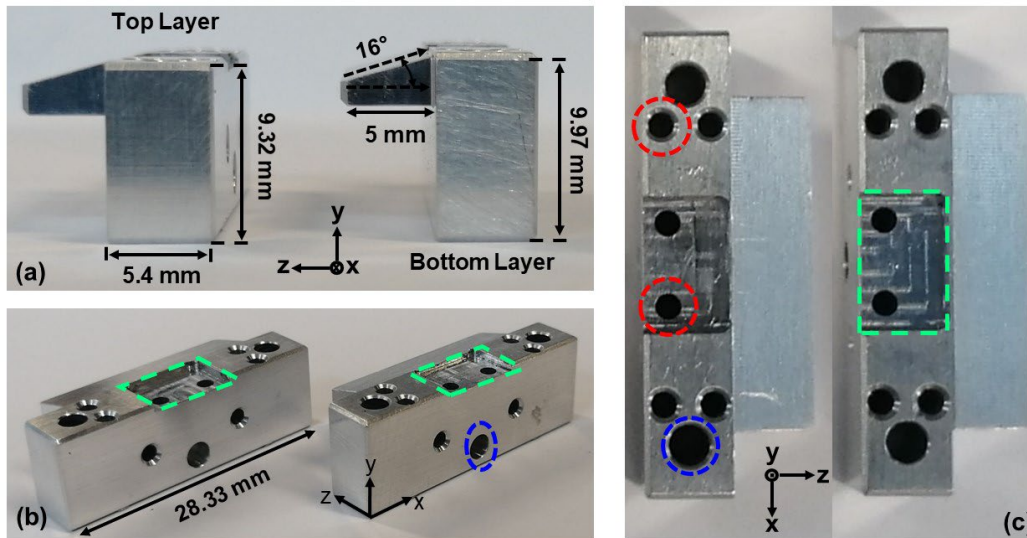
Fig. 5.9 Photographs and details of the two manufactured aluminum blocks, used to host and sandwich the metallized Si wafers with the hyperbolic lens and the GGW. (a) Profile view (b) Perspective view (c) Top view. The green dashed square is where the metalized silicon pieces will be placed, the blue dashed circles are screw holes, and the red ones are alignment pin holes.

The second step is to manufacture the GGW horn antenna and the HL using the clean room facilities of the Public University of Navarra. All the manufacturing process developed is described in Appendix B.

Fig. 5.10 shows a microscope photograph of the metalized GGW layer, where specific details such as GGW horn ground (green dashed square), feed transition (red dashed square), and alignment hole (blue dashed square) can be appreciated.
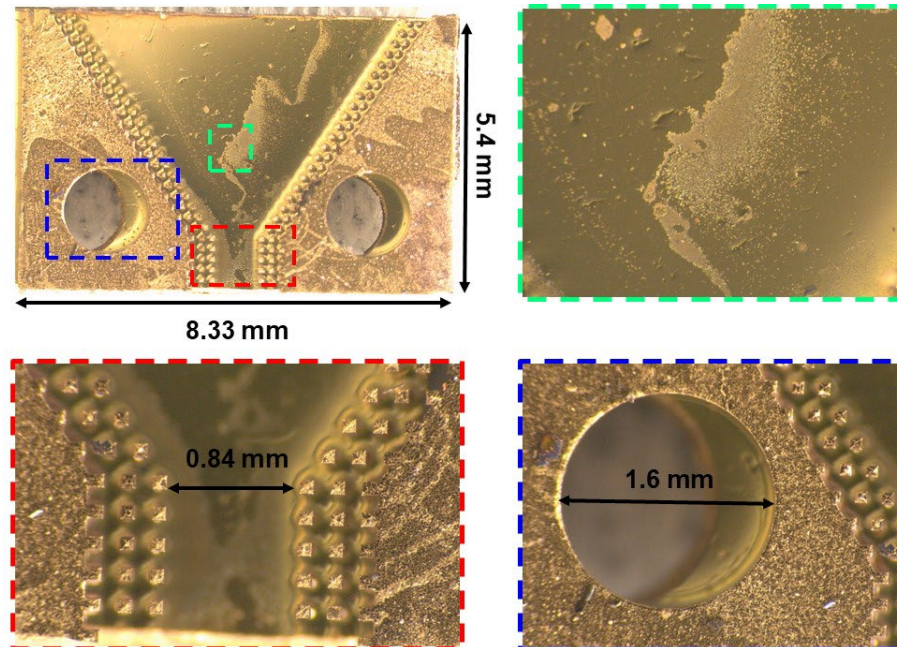
Fig. 5.10 Microscope photograph of a GGW horn antenna after metallization process with some manufacture details. GGW horn ground (green dashed square), feed transition (red dashed square) and alignment hole (blue dashed square)

A top layer corresponding to a structure similar to the HL but without pins was manufactured using the same methodology to validate experimentally the comparison presented in section 5.4. Fig. 5.11(a) shows the metallized piece without pins and Fig. 5.11(b) illustrate two spacers that keep the gap between top and bottom layer to assure the wave propagation, as was explained in section 5.2.
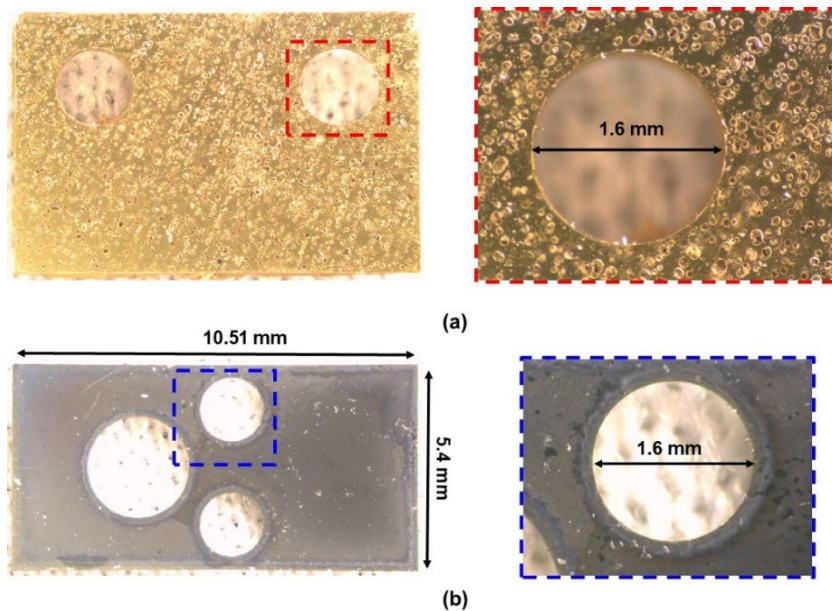
Fig. 5.11 (a) Photograph of a single top layer piece without lens. The dashed red square is a zoom of the alignment hole. (b) Photograph of one spacer to keep the gap between top and bottom layer. The dashed blue square is a zoom of the alignment hole.

Up to this point, the bottom layer (GGW horn antenna) has been manufactured. This piece is used in both studies made in section 5.2, a top layer without a lens and two spacers to assure the gap between layers. Fig. 5.12 shows the top layer including the aluminium block plus the spacers (dashed red curve), and the top layer without the lens. Unfortunately, the manufacturing process has not ended at the time of writing this chapter.
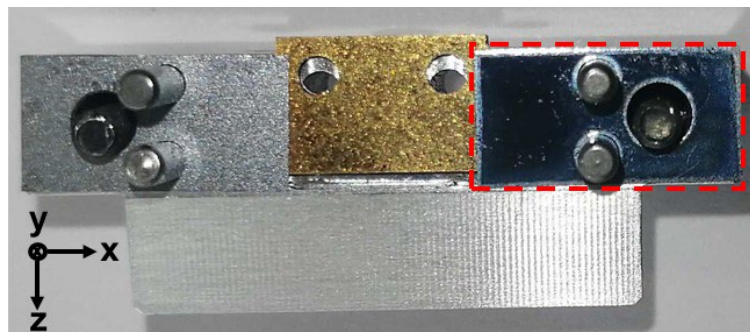
Fig. 5.12 Photograph of the top aluminum layer plus the dividers (red square), alignment pins and top layer without HL.

5.6   Conclusions

To conclude, in this chapter the designs of HLs illuminated by a GGW horn antenna at 300 GHz have been presented. The HL shapes has been synthesized using metallic pins and dielectric material to obtain a homogeneous refractive index profile, which provides a planar wavefront in the direction of propagation. In addition, the dielectric lens was implemented using Teflon in order to compare the behaviour of both systems. A GGW horn antenna has been also considered and combined with the HL to get a design compatible with wireless communication systems at sub-mmWave. The simulated results demonstrate that it is a viable alternative even at high frequencies where tolerances are critical. The joint operation of both components has been verified and leads to good radiation characteristics. A high realized gain of around 20 dB is obtained at 320 GHz. A comparison with a similar design with a dielectric lens and without a HL has been made. It has been proved that the addition of the HL leads to a gain improvement of roughly 3 dB at frequencies above 260 GHz. The dielectric lens achieves similar results using a matched layer technique. These results open new opportunities for the design of directive antennas at high frequency bands using planar designs. Furthermore, the viability of using artificial and dielectric materials to implement these structures has been demonstrated.

Chapter 6: Reconfigurable Liquid Crystal Meta-Reflectarray

6.1   Introduction

Reconfigurable or tuneable RA antennas have attracted considerable interest in the last years due to their advantages over conventional phased arrays. Moreover, the incorporation of new components, design techniques, and materials gives the engineering community many alternatives to create structures that satisfy the demand of incoming applications.

Liquid crystals (LC) are mainly employed at optical frequencies but in the last few years their application as functional materials in the microwave and mmWave spectrum is being explored. They have an anisotropic response which can be modulated by applying an external biasing producing a change in the material permittivity, which can be exploited to produce reconfigurable RA. One of the main hurdles to fully exploit LC at mmWave is the difference between the typical thickness of LC (a few tens of microns) and the operation wavelength (millimeter). Hence, to have a significant phase difference between extreme biasing states it is necessary to work near a resonance. This does not happen at visible frequencies, where the wavelength is of the order of hundreds of nanometers, but is critical at mmWave.

This chapter implements a reconfigurable reflectarray with low loss and moderate bandwidth using a novel nematic LC composition. This resonant structure was designed

to operate in the frequency band of 105-120 GHz, allowing independent electric control of the RA unit cells in one dimension (for 1D beam steering). The investigation pursues two main goals: 1) to experimentally check prospects for using the developed LC composition in meta-devices; 2) to find an optimal RA configuration that combines fabrication simplicity and the ability to achieve the maximum phase shift while keeping the reflectance as high as possible.

6.2   Design and Numerical Results

In this section the unit cell design is described and some important considerations are summarized in order to have a better understanding of the LC used. The details of the LC composition are shown in detail in Appendix C.

All the full-wave simulations in this work (the unit cell and RA proposed) were performed in collaboration with the company Tafco Metawireless S.L. and using the commercial electromagnetic software CST Studio Suite® [132].

6.2.1   Reflectarray Unit Cell Design

A detailed illustration of the proposed unit cell geometry for the designed RA is shown in Fig. 6.1. The structure consists of two quartz wafers (represented in red) 2 and 6 mm thick, respectively, between which a LC layer (represented in cyan) with height h_{LC} = 40 μm is placed. Quartz was selected due to its low dielectric losses in the spectral band of interest (see details in the next paragraph). The incident wave impinges on the structure along the z-axis from the side of the upper 2-mm-thick wafer, on the bottom surface of which a MTS facing the LC layer and playing a role of the upper electrode is patterned. The MTS unit cell consists of a rectangular aluminum patch with transverse dimensions w_x = 0.65 mm, w_y = 0.8 mm and thickness t = 0.4 μm connected through narrow strips 70 μm wide to the vertically neighboring unit cells (represented in orange). The lateral periodicities of the unit cells in x- and y-directions are d_x = 0.9 mm and d_y = 1.05 mm, respectively. The MTS is implied to be excited by a polarization perpendicular to strips,

which do not affect the device performance but are necessary to deliver the same electric potential to all the patches in line when biasing the LC. The lower 6-mm-thick wafer contains a uniform (unpatterned) 0.4-μm -thick aluminum layer forming the ground plane (GP) bottom electrode kept at a zero potential.

As shown in Fig. 6.1(b), two thin orienting layers are deposited onto both the MTS and GP. They are made of poly (vinyl alcohol) and have a thickness below 0.1 μm so they have a negligible impact on the electromagnetic response of the device. These layers are important in the LC technology: due to a procedure of mechanical rubbing conducted with them beforehand, the orienting layers ensure a proper alignment of the LC molecules in the prescribed direction (in our case parallel to the *y*-axis) when no bias voltage is applied.
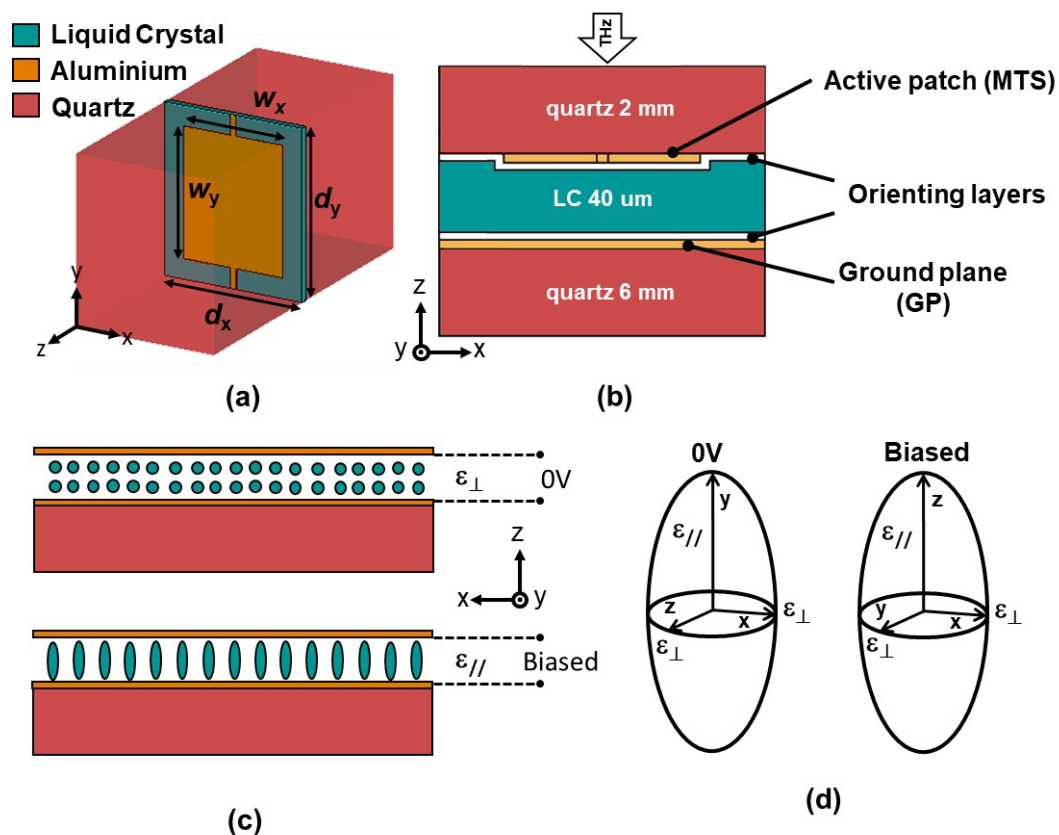
Fig. 6.1 Schematic view of the LC-based RA unit cell: (a) isometric view with the main dimensions; (b) cross-sectional view, showing the materials and arrangement. (c) Schematic representation of the LC molecules in the 0 V and biased states. (d) LC permittivity tensor orientation in both states.

6.2.2   Full-Wave Simulations

In the simulations, aluminum was modelled as a lossy metal with conductivity σ = 5 .93×10^6 S/m (effective conductivity corresponding to its nominal DC conductivity divided by a factor of 6, to model imperfections such as roughness, etc.), while the relative complex dielectric permittivity ε_{Quartz} = 3.78 (1 − j0.002) was specified for the quartz wafers.

The inherently anisotropic LC medium was modeled using a complex dielectric permittivity tensor $\bar{\bar{\varepsilon}}$. In general, the local components of $\bar{\bar{\varepsilon}}$ at every point of the LC layer depend on the orientation of the local director vector of LC molecules. This vector represents a local optical axis of the LC medium and is a function of the local bias electric field inside the medium. Since the biasing of the LC is done by applying a low-frequency alternating current (AC) voltage [141] (typically 1 kHz), in a strict sense, the accurate electromagnetic analysis of the RA should involve two subsequent stages: 1) calculation of the self-consistent 3D spatial distribution of the quasi-static electric field inside the LC cell and the induced distribution of local directors taking into account the geometry of the MTS electrode (with an AC bias voltage as a variable parameter); 2) full-wave high-frequency simulations of the RA response at millimetre waves using a 3D spatial distribution of the dielectric permittivity tensor $\bar{\bar{\varepsilon}}$ (x,y,z) which directly relates to the calculated LC director distribution.

The aforementioned two-stage scheme for the electromagnetic analysis of LC devices is non-trivial and is not readily available in commercial electromagnetic simulators, such as CST Studio Suite®, typically employed to model high-frequency structures. This problem, however, can be solved approximately by assuming that the LC director is rotated uniformly below the upper patch as the biasing voltage is varied and is kept with the original orientation (parallel to y in our case) outside the patch. Such simplification is

valid for the patch-like geometry of MTS unit cells with a large fraction of metal filling MF $= w_x \times w_y / d_x \times d_y$. In this case, MF ≈ 0.55 meaning that near 45% of the LC layer (in gap areas) remain biased weakly. This partially decreases the tunability of the device versus MF ≈ 1 case but, at the same time, it potentially diminishes dissipative losses in the structure.

When modelling, orientation of the LC director vector $\boldsymbol{n}$ was specified by the angle α taken from the y-axis in yz-plane: $\boldsymbol{n} = (0, \cos\alpha, \sin\alpha)$. In the unbiased state ($V_b = 0$) the LC molecules are oriented along the rubbing direction, i.e. y-axis [$\alpha = 0$, Fig. 6.1(c), top and (d) "0 V"], and the permittivity tensor in the chosen coordinate system xyz is diagonal and follows the next expression [142]:

$$\bar{\bar{\varepsilon}}\,(V_b = 0) = \begin{bmatrix} \varepsilon_\perp & 0 & 0 \\ 0 & \varepsilon_\parallel & 0 \\ 0 & 0 & \varepsilon_\perp \end{bmatrix}, \tag{6.1}$$

where $\varepsilon_{\parallel,\perp}$ is the complex permittivity as defined before and the numerical values of the real and imaginary parts are given in Table C.2. Likewise, in the maximum bias state the LC director is oriented perpendicular to the wafer surface, i.e. along z-axis ($\alpha = 90$ deg, Fig. 6.1(c), bottom and (d) "Biased"), and the permittivity tensor transforms to:

$$\bar{\bar{\varepsilon}}\,(V_b = V_{max}) = \begin{bmatrix} \varepsilon_\perp & 0 & 0 \\ 0 & \varepsilon_\perp & 0 \\ 0 & 0 & \varepsilon_\parallel \end{bmatrix}. \tag{6.2}$$

To cover all possible intermediate orientations of the LC optical axis in the simulator the local coordinate system $x'y'z'$ associated with the LC layer was introduced, where x'- and y'-axes coincide with the x-axis of the global coordinate system xyz and the LC director vector $\boldsymbol{n}$, respectively. The vector unit basis ($\boldsymbol{e}_{x'}$, $\boldsymbol{e}_{y'}$, $\boldsymbol{e}_{z'}$) of the system $x'y'z'$ is as follows: $\boldsymbol{e}_{x'} = (1, 0, 0)$, $\boldsymbol{e}_{y'} = (0, \cos\alpha, \sin\alpha)$, $\boldsymbol{e}_{z'} = (0, -\sin\alpha, \cos\alpha)$. In the local system $x'y'z'$ the permittivity tensor is described by the matrix (6.1).

The structure was simulated in the frequency domain by using the software defined unit cell boundary conditions, which perform a Floquet modes analysis on a single unit cell. A TEM mode with vertical polarization (electric field parallel to x) at normal incidence was used to excite the structure. The structure parameters w_x, w_y, d_x, d_y were tuned to get the maximum possible phase excursion of the reflection coefficient between the extreme cases of the LC permittivity while keeping at the same time the highest possible magnitude of the reflection coefficient in the operation band between 105 and 125 GHz. The LC layer thickness h_{LC} was fixed at a value of 40 µm defined by the thickness of technological spacers available. As mentioned above, only the LC substrate below the patch was rotated, assuming that only that area would be properly biased in the experimental demonstration.
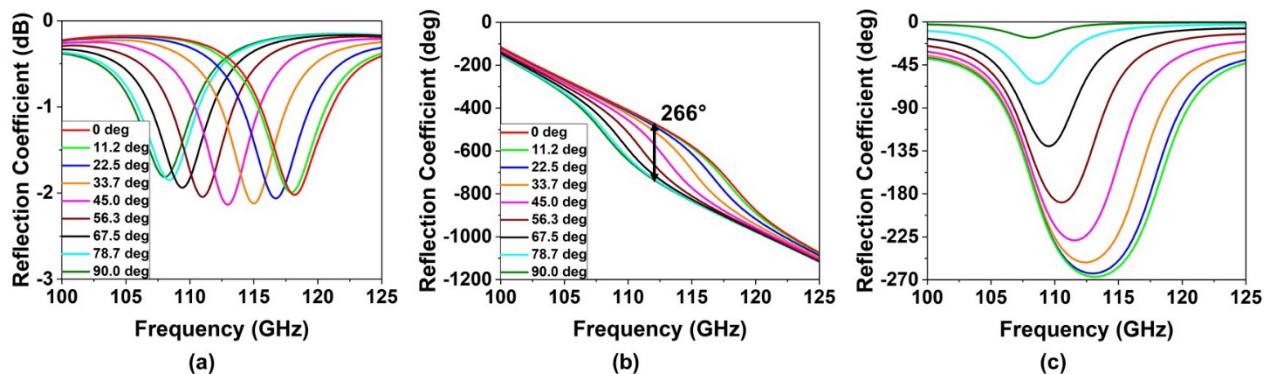
Fig. 6.2 Simulated characteristics of the RA for different orientation angles α of the LC director: (a) reflection coefficient magnitude in dB; (b) reflection phase in degrees; (c) phase curves normalized to the case of 0 deg.

Fig. 6.2 shows the amplitude and the phase for the reflection coefficient of the RA at different rotations of the LC director vector α varying from 0° to 90°. As shown in Fig. 6.2(a), there is a resonant dip in the spectrum of the reflection coefficient magnitude which shifts from 117 to 108 GHz when the LC tensor is rotated from 0° to 90°. In all considered cases, its magnitude is above −2.5 dB within the entire frequency band. This resonance is accompanied by a phase variation [Fig. 6.2(b)] which can be modulated by rotating the LC tensor. A maximum phase excursion of 266° is obtained at 113 GHz. To ease the

114

comparison, all the phase curves have been normalized in Fig. 6.2(c), by simply subtracting the phase of each case to that of the 0° state of the LC tensor. There, it can be appreciated clearly the range of phases achieved by rotating the permittivity tensor. These results validate the initial hypothesis that it is necessary to work near a resonance to have a significant phase excursion.

With the previous simulation results, a complete characterization of the reflection phase with respect to the LC tensor orientation was obtained. This study can be used to implement a beam steerer working in reflection by introducing an arbitrary orientation of the LC tensor in each unit cell. The characterization in this case was done using a single row of the RA with 1 × 33-unit cells, illuminated by a plane wave with horizontal polarization at an incidence angle of θ_i = 10 deg, see Fig. 6.3(a). Periodic boundary conditions were implemented along y and open+add space along x and z. The tensor rotation in each unit cell of the RA was configured by defining the desired angle for the reflected beam. Fig. 6.3(b) shows the radar cross section far-field patterns for the considered cases at the frequency of maximum amplitude for the deflected peak (see label). Fig. 6.3(c), (d), (e) and (f) show a contour plot diagram representing the radar cross section far-field patterns as a function of frequency and angle when the RA is configured to produce a reflected beam at 20°, 25°, 30° and 35°, respectively. As shown there, in all cases the main reflection beam occurs at 10° (that corresponds to the specular reflection) in all the considered bandwidth except at the operation band wherein the RA is able to modulate the beam in the desired direction.
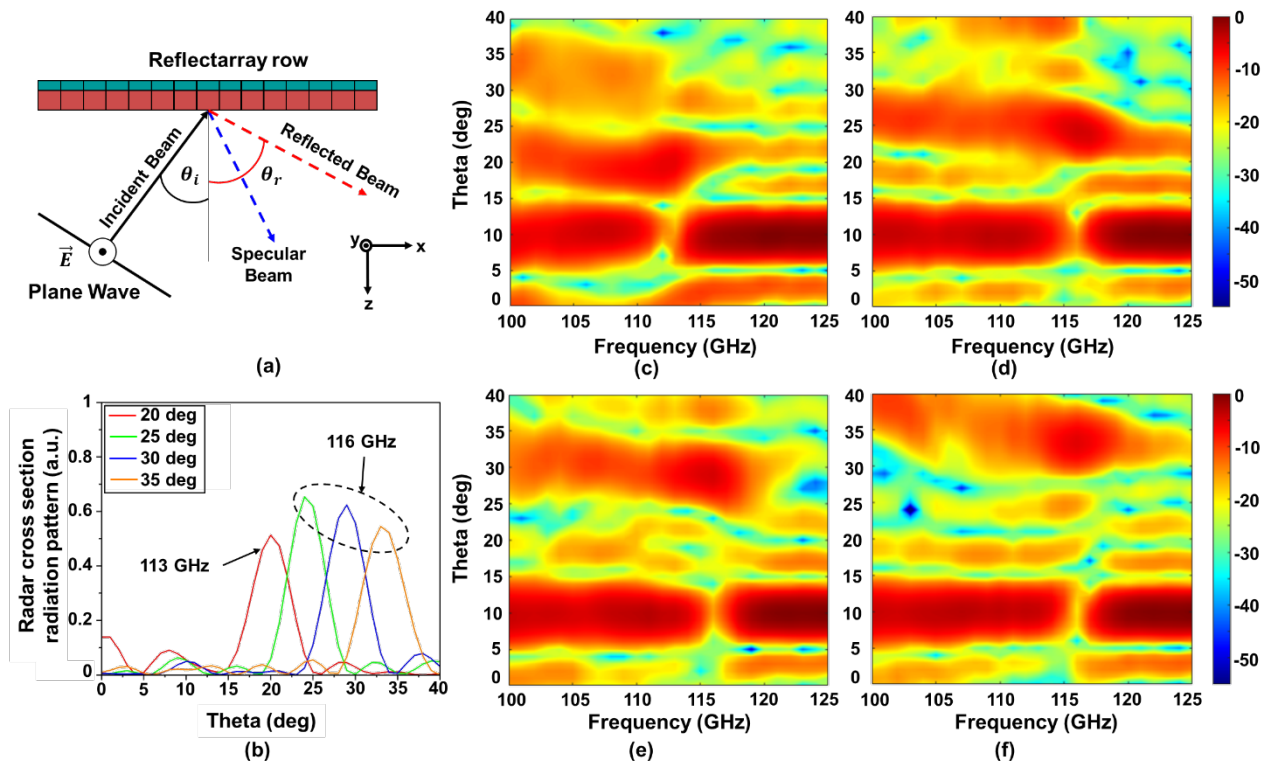
Fig. 6.3 (a) Beam-steerer simulation scenario where θ_i = 10 deg is the angle of the incident beam and θ_r is the angle of the beam reflected in the desired direction. (b) Radar cross section far-field pattern at the frequency of maximum amplitude for the deflected peak (see label) for four different beam-steering cases. Contour plot diagram for a beam reflected at (c) 20°, (d) 25°, (e) 30° and (f) 35°. Scale is in dB and each panel is normalized to the maximum.

6.3   Prototype Fabrication and Characterization

To corroborate experimentally the previous results, the designed RA prototype was fabricated and measured. It contains 29 × 33 RA unit cells with overall dimensions of 29.7 × 30.45 mm. Fig. 6.4(a) shows in detail the biasing configuration used, with each of 33 columns connected to a corresponding metallic pad to introduce the biasing voltage and drive correctly the LC.

116

To fabricate the prototype, first, two polished round wafers made of fused quartz 2 mm thick (used for MTS) and 6 mm thick (used for GP) with a diameter of 60 mm were prepared. Both wafers were symmetrically cut from both sides by 13 cm as shown in Fig. 6.4(a) and (b). Such a form of the quartz wafers was chosen to ease electric connection to the GP electrode after assembling the device by orienting the wafers orthogonally to each other, see Fig. 6.4(b). Both wafers were metalized then on one surface with 0.4-µm-thick aluminum using magnetron sputtering. For the 2-mm-thick quartz wafer, a contact photolithography technique was applied afterwards to create the MTS pattern. Besides the active patch array itself, elongated contact pads were added to the pattern at the periphery to allow the electric connection to individual biasing lines, see Fig. 6.4(a). To avoid excessively narrow gaps between pads, these were separated into two sets: 17 pads were placed on one side to control the odd biasing lines, while 16 pads were located on the opposite side to govern the even ones.
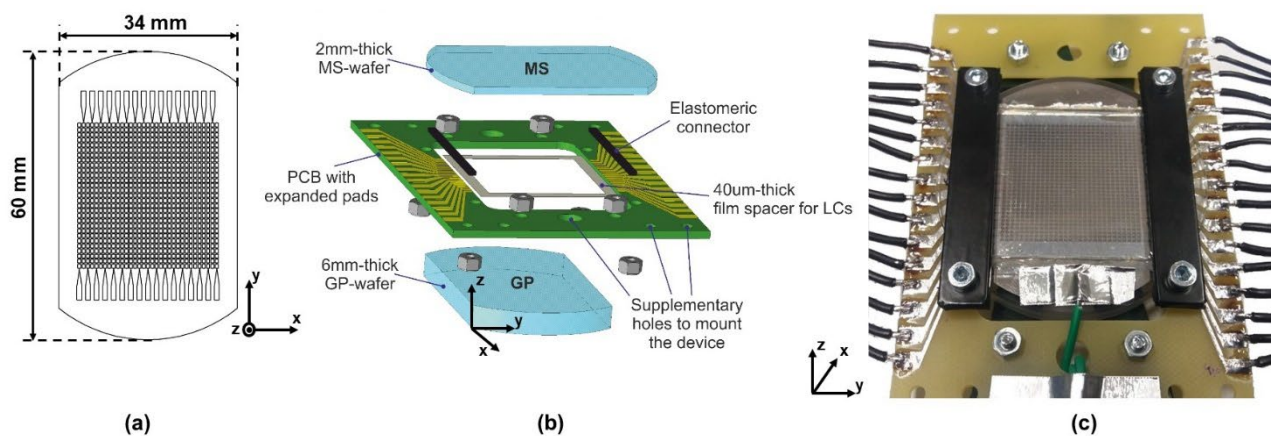
Fig. 6.4 (a) Schematic representation of the manufactured RA: (a) front view of the 2-mm-thick quartz wafer with active patches (MTS) and contact pads. (b) Isometric exploded view of all the pieces composing the RA and showing in the center the PCB used to realize the bias connection. (b) Photo of the assembled device prepared for connection to a 33-channel voltage generator.

After metallization and photolithography, the MTS and GP faces of the wafers intended to be in contact with the LC were spin-coated with thin poly(vinyl alcohol) orienting layers using a spin coater HO-TH-05 (Holmarc, India). The orienting layers were then gently

rubbed with a rubbing machine HO-IAD-BTR-01 (Holmarc, India) to ensure alignment of unbiased LC molecules on the wafer surface along *y* axis. After rubbing, the LC was injected into the gap between the quartz wafers provided by peripheral 40 µm-thick polypropylene strip spacers 4 mm wide. Finally, all edges were sealed to guarantee proper consolidation without LC leakage.

After completing fabrication of the "quartz-LC" core of the device, an auxiliary printed circuit board (PCB) was implemented to simplify the biasing connections, see Fig. 6.4(b). The electric connection between pads on the quartz wafer and PCB was done using elastomeric connectors [143]. This type of flexible connectors, well-known in LC display technologies, is made as a set of narrow conductive layers interleaved with insulating ones. With elastomeric connectors the soldering process on the quartz wafers is avoided, preserving integrity of the LC device. Fig. 6.4(c) shows the final structure after assembling. Notice that soldering joints are located on the PCB outside the RA. The ground connection is provided through the green wire which is attached to the GP electrode by means of a metal foil sticky tape.
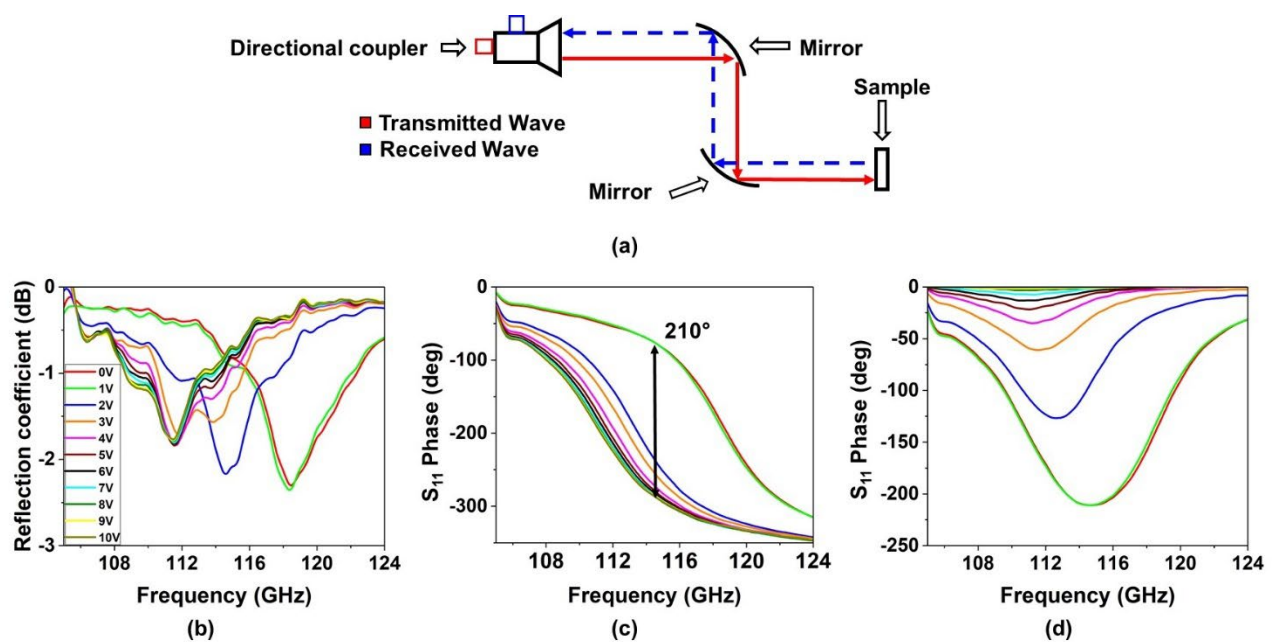
Fig. 6.5 (a) Setup employed in the characterization (b) Reflection coefficient magnitude in dB. (c) Reflection phase in degrees. (d) Phase curves normalized to the case of 0 V.

For the experimental characterization of the fabricated RA, an AB Millimetre Vector Network Analyzer MVNA-8-350 [143], equipped with a quasioptical bench and a rotary platform was employed. The samples were measured from 105 to 125 GHz with a step of 50 MHz. The first setup used in the characterization consisted of a transmitting horn antenna illuminating a pair of elliptical mirrors to focus the beam on the sample at normal incidence, see Fig. 6.5(a). In this first set of experiments, all the biasing lines were driven at the same voltage so that the reflected wave also travelled in the normal direction (since there is no phase difference amongst the unit cells). The reflected wave travelled back to the horn antenna guided by the parabolic mirrors and was further detected through a directional coupler connected to the antenna. Before performing the experimental characterization of the prototypes, the setup was calibrated by putting a mirror at the sample position. The biasing voltage was varied from 0 V to 10 V, with a step of 0.50 V, although in the figures curves are represented with a step of 1 V for clarity.

Fig. 6.5(b) shows the reflection coefficient magnitude achieved for the prototype, demonstrating good agreement with the simulation results. The losses obtained in measurements are similar to those obtained in simulation, with a minimum of the reflection coefficient around −2.5 dB. A frequency shift towards higher frequencies with respect to the simulation results was also noticed, especially near the maximum bias state. The maximum experimental phase excursion was 210°, which is 56° below the simulation results, see Fig. 6.5(c) and (d). It is also noticed that there is an abrupt change for the phase between 1 V (light green curve) and 2 V (dark blue curve), indicating that the sensitivity of the LC molecules is maximal in this region and that a small variation of the biasing voltage yields large changes in the LC director orientation. Despite the mentioned differences, the experimental results validate the simulation study, the good performance of the LC used, and the correct bias connection implemented in the structure.

With the previous measurements, a complete characterization of the reflection phase with respect to the spatially uniform bias voltage was obtained. In the second set of

experiments a non-uniform biasing was applied to the RA. This was done using the experimental setup shown in Fig. 6.6(a). The setup is composed of two horn antennas (working in *D*-band from 105 to 125 GHz) and the sample holder where the RA is placed. The distances from the sample to the transmitting and receiving horn antennas were 20 mm and 25 mm, respectively. The sample holder was placed on a rotary platform (grey color) to control the angle of incidence upon the RA. The receiving antenna was also placed on a platform connected through an arm to the axis of the rotary platform, so that it could freely rotate and scan the angular power distribution, see Fig. 6.6 (a). The setup was covered with absorbing resin to minimize spurious ambient reflections. A custom-made 33-channel voltage generator (voltage control unit) was used to feed all the biasing lines of the RA independently, see Fig. 6.6(b).

To characterize the beam steering performance of the device, the incidence angle between the transmitter and the RA was fixed to 10 deg. The RA unit cells were biased properly by defining the desired angle for the reflected beam and tuning consequently the voltage generator. Fig. 6.6(c), (d), (e) and (f) show a contour plot diagram for the beam reflected at 20°, 25°, 30°, and 35°. Analysing Fig. 6.6(c) for the beam reflected at 20°, it is seen that from 105 to 120 GHz a good pointing is achieved, validating the correct biasing made and corroborating the simulation results. For 25° (Fig. 6.6(d)) the bandwidth is reduced with respect to the previous result and the beam does not have a big resolution. The rest of angles characterized have good behavior, achieving an adequate pointing in the desired direction maintaining the bandwidth (from 105 to 120 GHz in most cases).
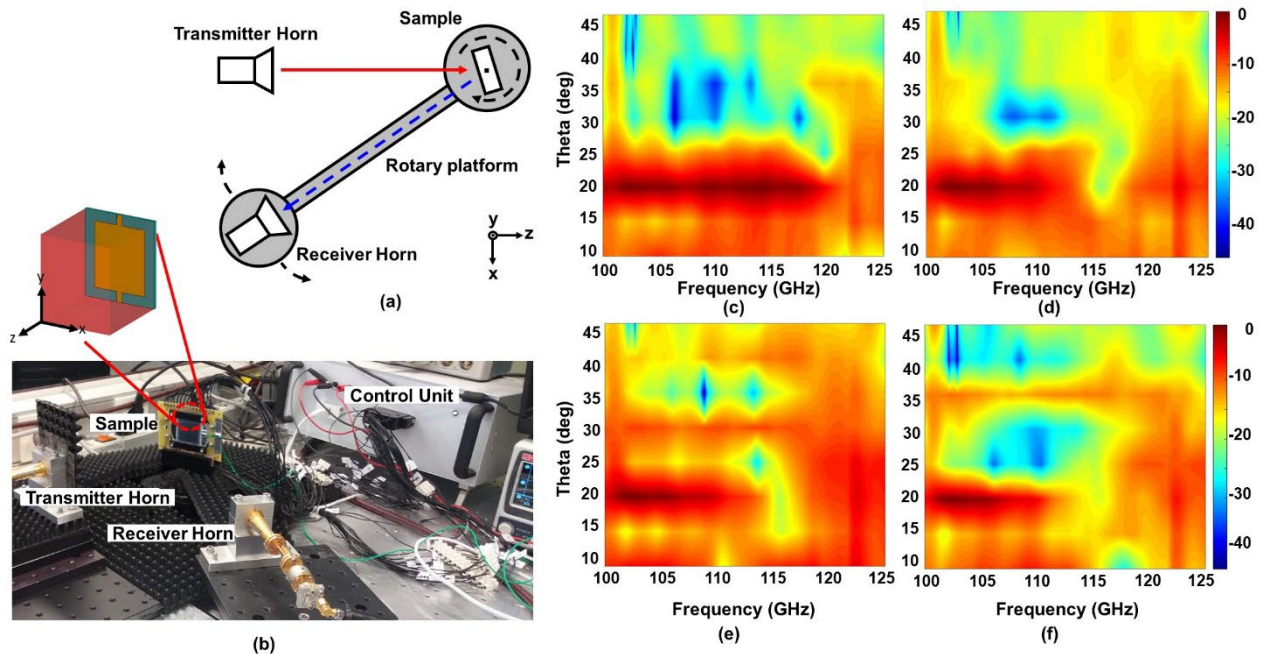
Fig. 6.6 (a) Top view of the setup employed in the non-uniform biasing characterization (b)Photograph of the measurement scenario composed of two horn antennas and a rotating positioner where the RA under test is placed. Contour plot diagram for a reflected beam: (b) 20°, (c) 25°, (d) 30°, and (e) 35°. Scale is in dB and each panel is normalized to the maximum.

6.4   Conclusions

To conclude, in this chapter a reconfigurable LC-loaded reflectarray operating near 110 GHz has been simulated, manufactured and experimentally measured. The device has a configuration of a high-impedance surface with a patch MTS patterned on a 2-mm-thick quartz substrate separated from the ground plane through a 40-µm-thick LC layer. The electric biasing of the LC-loaded RA unit cells is realized by introducing narrow inductive strips connecting neighboring patches in one dimension. The simulations show a maximum phase excursion of 266° with losses below 3 dB. In the 1D beam steering scenario, when properly tuned, the reflected beam is directed in the engineered direction at the operation frequency. The manufactured prototype with 33 × 29-unit cells shows a maximum phase excursion of 210° with losses around 2.5 dB. The experimental results

demonstrate the ability of this structure to steer the beam in the desired direction with a good pointing in a bandwidth around 12 GHz.

One of the novelties of this work lies in a new LC composition developed by the Institute of Applied Physical Problems of Minsk for millimeter-wave applications. This composition based on n-quaterphenyl and n- quinquiphenyl substances was successfully proven in the implemented reflectarray and is distinguished by the best dielectric parameters in comparison with other LC developers: it has low dielectric losses (<0.003) and high dielectric anisotropy (>1.3). In addition, the main criteria concerning parameters of LC molecules affecting the dielectric anisotropy, dielectric losses and tunability of LC compositions both at microwave and subterahertz frequencies were found.

The presented results demonstrate that LC technology can be viable for reconfigurable devices operating at millimeter and submillimeter waves, providing simple solutions for new applications.

Chapter 7: General Conclusions and Future Lines

7.1 General Conclusions

Noteworthy advances have been obtained in communication systems in the last years at mmWave and terahertz waves, proposing new challenges to the engineering community. In addition, the increase in the application and services demanding more capability has opened new avenues for developing structures and systems that solve the novel challenges proposed. In this thesis novel devices at mmWave and sub-mmWave based on metamaterial concepts have been proposed as alternative solutions to address some of the problematics created by the rapid development of digital communications in modern society. The research work has covered concepts and technologies deemed essential to develop the structures presented:

- Gap Waveguide technology to guide waves.
- Simple and effective way to generate circular polarization with different bandwidths.
- The use of metasurfaces (with homogenous and variable refractive index) to improve antenna system radiation characteristics.
- Geodesic lens combined with reflector to get a compact system with beam scanning capability.
- Liquid crystal material to devise a reconfigurable a reflectarray operating at mmWave.

7.1.2   Compact fully metallic antennas with circular polarization in Gap Waveguide Technology.

After the work realized it is clear that low loss feeding networks at mmWave are feasible using GW technology, specifically RGW variant, which in addition fits seamlessly with the novel way to generate CP proposed in this thesis. Chapter 2 was dedicated to the design and experimental demonstration of three fully metallic CP antennas operating in the V-band that use these concepts.

- It has been demonstrated that using two arms of different lengths in the feeding system allows the generation of CP in a simple and compact setup.

- A simple antenna using the previous configuration and a slot on top with a gain of 5.49 dB and a BW of 11.5% has been demonstrated

- A broad operation BW of 14.5% with an AR < 3 dB and RHCP has been obtained by the DHG antenna with a small footprint (30 mm × 30 mm).

- The gain has been improved from 5.49 dB (D antenna) to 11.1 dB (DHG antenna) with the insertion of two modifications: a horn antenna profile and a circular concentric groove.

- Introducing four periodic circular corrugations on the top plate the gain has been enhanced up to 18.4 dB exploiting leaky wave excitation and extending the reach of BE antennas to GW technology.

- In relation with the previous point, it is worth mentioning that the GW BE antenna is the first antenna of this type having CP with a single feeder (without combining two orthogonal sources)

- In all cases, numerical simulations have been corroborated with experimental results with good general agreement, demonstrating good radiation characteristics in compact and low-profile structures.

7.1.3   Fully metallic metalens systems

Metasurfaces were considered in Chapter 3 to 5 to improve the radiation characteristics of systems based on GW technologies, keeping their versatility and the constraint using fully metallic structures.

Chapter 3:

- A fully metallic lens antenna system combining a LL with a GGW horn antenna and operating at the V-band has been numerically and experimentally demonstrated.

- The LL refractive index profile has been synthesized using unit cells based on metallic pins. It has been demonstrated that this implementation generates a planar wavefront at broadside, validating the approximation using metallic pins.

- When combined with the GGW antenna, a compact system with excellent radiation characteristics is obtained.

- The system is fully metallic, so that it presents low loss and is more robust than other solutions using dielectrics. Furthermore, due to its flat profile is easy to adapt to planar surfaces.

- The simulated and experimental results are in excellent agreement with peak realized gain 22.5 dB at 61 GHz and a BW of 26.2%.

- An important conclusion is that it has been demonstrated that CNC micromachining is reliable even at high frequencies such as the one considered here.

In Chapter 4:

- A combination of a dual-layer Luneburg geodesic lens with a parabolic reflector system has been designed.

- Using the solution to the complement of the generalized Luneburg lens problem, virtual images have been implemented to illuminate the parabolic reflector and get a compact system.

- The system proposed has achieved a beam scanning around ±18° using 11 ports distributed around the periphery of the lens.
- A comparison between the complementary GLL and a classical parabolic reflector has demonstrated a reduction of size around 30%.

In Chapter 5:

- A hyperbolic metalens illuminated by a GGW horn antenna at 300 GHz has been presented.
- The unit cell is based on a metallic pin array that synthesizes an effective permittivity to build a hyperbolic lens with an equivalent homogeneous refractive index.
- The behaviour of the system has been compared with a conventional dielectric lens implemented using Teflon.
- A realized gain around 20 dB is obtained at 320 GHz.
- The simulated results suggest that GW technologies and homogenized metalenses could be successfully implemented at high frequencies.
- The design proposed is pioneering in proposing antennas fully based on GW operating at THz frequencies.

7.1.4   Liquid Crystal Reflectarray

At the end of the investigation research, a new and exciting line was considered to design a prototype that increases the scanning capabilities. This recent incursion was developed at mmWave, specifically at D-band.

- A reconfigurable RA operating at 100 GHz based on LC has been numerically and experimentally demonstrated.
- Given the contrast between the wavelength and the typical LC thickness, a resonant structure has been designed to work near a region with a fast phase variation. This is challenging, because near resonances losses tend to grow.

- Despite the necessary resonant behavior, a maximum phase excursion of 210° with low losses around 2.5 dB have been demonstrated in the experimental results.

- The experimental results demonstrate the ability of this structure to steer the beam in the desired direction with a good pointing in a bandwidth around 12 GHz.

- This study demonstrates the viability of using LC in mmWave range devices.

7.2 Futures Lines

The research presented in this thesis opens new questions an research lines in a variety of topics. The two main research topics in this thesis have been focused on GW technologies and MTS antennas and therefore most of the envisaged future work is oriented towards consolidating and expanding the practical applicability of these two topics:

- A possible extension of the CP GW antennas investigated in Chapter 2 is to add another pair of orthogonal arms at the opposite side, to generate RHCP and LHCP in the same system. The idea is shown in Fig. 7.1(a).

- Also, apertures of different shapes could be investigated to get different radiation patterns or polarization characteristics.

- Implement said antennas in similar technologies, such as SIW, more oriented towards microwave frequencies.

- Develop tunable antennas able to control de polarization exploiting the novel way to generate CP combined with GW technology. The idea is based on the fact that CP is obtained by using arms of different lengths. Therefore, the arms can be divided in two parts connected by an active element (a pin diode for example) so that in off-state the arm is short and in on-state the arm is long. Hence, by combining states one can have RH, LH or linear polarization. To get the necessary isolation necessary for the biasing of the active elements, the optimal technology to implement this idea would be the MGW (RGW and GGW are fully metallic and

then electrodes would be short-circuited). Adding active devices would definitely extend the reach of the antennas described in Chapter 2.

- Similar to the first point and related with the previous one, several elements could be combined in an array to have a richer variety of polarization states. Therefore, controlling their relative phase with active elements one could switch between different polarization states or point in different directions (i.e. active beam steering capability).

- With regards to the LL GW discussed in Chapter 3, perform an experimental study of the scanning capability using different feeding ports. Alternatively, an interesting solution could be implementing mechanical scanning using one feeding port that rotates around the structure.

- Extend the reach of fully metallic antenna lens systems with metalenses based on metallic pins towards other configurations, such as the half Maxwell fish eye lens that can result in more compact structures at mmWave and terahertz frequencies.

- A limitation of the LL GW antenna demonstrated in Chapter 3 is that only the H-plane is modulated by the LL, giving rise to a fan beam radiation pattern. A possible solution to enhance the E-plane as well is to implement a vertical packaging. This way, several antenna-lens systems can work in parallel enhancing the directivity in the E-plane. Fig. 7.1(b) shows an example of three vertically packaged half Maxwell fish eye lenses.

- Regarding Chapter 4, a task that is pending is manufacturing the GLL pillbox antenna and performing the experimental demonstration.

- Establish formally (other than heuristically) the optimal curve for the feeder that illuminates the parabolic reflector [shown in Fig. 4.11(a),(b)].

- Related with previous point, study if that feeding curve can be also used with a geodesic lens, calculating mathematically the index profile it should have to illuminate efficiently the parabolic reflector.

- Another possibility would be keeping the same GLL and modify the reflector to have a profile different from parabolic so that the beam scanning is optimized,

considering that the wave at the output of the GLL lens does not point towards the parabola vertex for angles different from zero.

- As for Chapter 5, manufacturing and experimental demonstration of the HL is still pending. The fabrication could be done using the two methods proposed: CNC and photolithography process (at the Public University of Navarre's clean room). The experimental demonstration can also be done at the Public University of Navarre's facilities.

- Lens profiles different from hyperbolic such as elliptical can be explored to study their behavior at these frequencies.

- Design LC based reflectarrays able to perform full-space scanning (at least in the two principal planes), beyond the single plane scanning demonstrated in Chapter 6.

- Another possibility is to combine LC and bed of nails structures to get reconfigurable lenses, where the index variation is achieved by modifying the biasing or the LC. That way, the same structure could implement a Luneburg lens, Maxwell lens, Eaton lens, etc. with a dynamical control over the response.
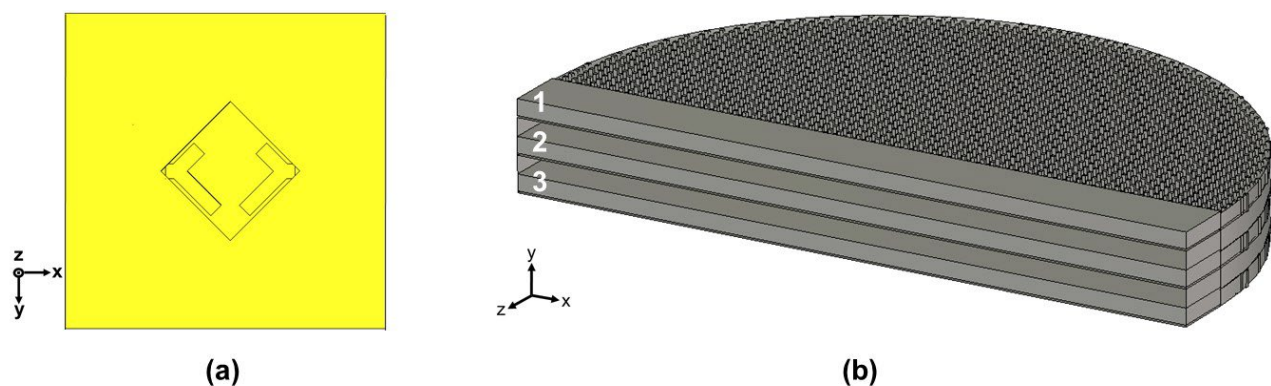
Fig. 7.1 (a) Top view of two feeding networks in opposite sites to generate RHCP and LHCP. (b) A vertically package of three half Maxwell fish eye lenses.

Appendix A

A.1 Ray-tracing configuration for a simpler reflector

This appendix describes the procedure and methodology followed to develop the ray – tracing used in Chapter 4 section 4.4 to achieve the radiation pattern of a classic parabolic reflector. The study presented here defines some concepts employed that evaluates the directivity, SLLs, and scanning range in the structures mentioned before.

A.2 Ray tube basics

First, the ray tube theory is presented. With this model, it is possible to obtain the amplitude of the electric field in a ray tracing representation. If the phase and amplitude of the electric field are known, a far-field radiation pattern can be calculated using the Huygen's principle.

The ray tube theory is used in GO and assumes that the electromagnetic energy propagates as rays with the phase velocity of the medium, and the power flows along the ray forming a closed ray tube. The power magnitude stays constant as it propagates in a lossless and source-free medium. Fig. A.1 shows the concept of the ray tube model with a ray constrained inside an enclosed tube (k) by two neighboring rays [($k - 1$) and ($k + 1$)]. The components dA and dA' are the differential areas or cross-section areas of the wavefronts, and the ray is defined as orthogonal to these areas [144]. The ray points to

dA' and the power flows from dA to dA'. Due to energy conservation, the power density follows the equation:

$$PdA = P'dA',$$

where P and P' are the power density at dA and dA', respectively. In particular, when the ray tube cross section dA decreases, the power density P increases P' and vice versa. The case in which the power density decreases represents diverging rays, and when the power density increases, represents converging rays.
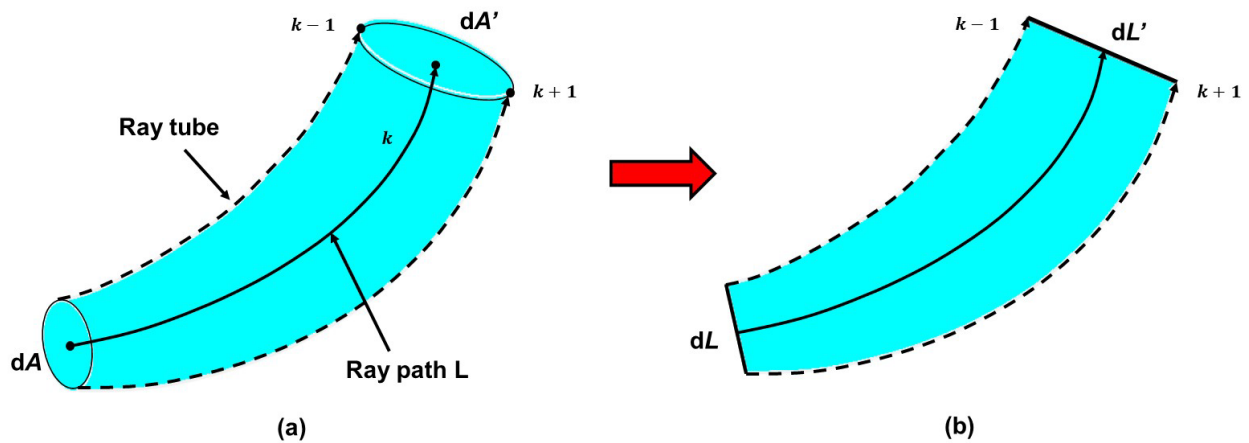
Fig. A.1 Power flows along the ray path and is constrained inside the ray tube (shaped by two neighboring rays ($k - 1$) and ($k + 1$) form k ray), where dA and dA' are the cross-section areas of the wavefronts [144] (b) Bi-dimensional transformation of the ray tube concepts.

As the amplitude of the electric field is proportional to the square root of the power density P, the ray tube eq. (A.1) can be rewritten as:

$$E^2 dA = E'^2 dA',$$

$$E' = E\sqrt{\frac{dA}{dA'}}$$

(A.2)

131

Therefore, the amplitude of the electric field is related to the cross-section area. The phase can be directly obtained from the path followed by the ray. According to Fermat's principle, which states that the variation of a ray path has a stationary optical length, the rays follow the shortest optical path length (OPL) [145].

This method can be particularized to bi-dimensional problems by using a differential of length instead of a differential of area, see Fig. A.1(b). Following the notation proposed before, the transformation in a bi-dimensional system is:

$$PdL = P'dL',$$ (A.3)

where dL'_k is the width of the ray tube at the output and dL_k at the input, see Fig A.1(b). Then the amplitude of the electric field can be rewritten as:

$$E^2 dL = E'^2 dL',$$

$$E' = E\sqrt{\frac{dL}{dL'}}$$ (A.4)

A.2.1 Far-field pattern control

In this section, the previous procedure is applied in a simple problem considering a single point source to illustrate the main concepts. The problem is sketched in Fig. A.2 where a bi-dimensional system invariant along the *x* direction is considered. The analysis is done following the method explained above and in [144], [146]. The wave radiated by the source propagates a certain distance. Applying Huygens' principle, the points illuminated behave as secondary sources from which new wavelets are launched. The farfield distribution can be then calculated from these secondary sources. Figure A.2(a) shows the model with the main source P_k and the three secondary sources $(k-1)$, k, $(k+1)$

132

with their corresponding rays. Taking the excitation point as the reference (P_k), the phase of the k_{th} ray Φ_k at the aperture is:

$$\phi_k = k_0 \sigma_k \qquad \text{(A.5)}$$

where σ_k is the shortest physical path length between the excitation point P_k and the k_{th} radiating dipole. The shortest physical path length σ_k is calculated simply as the distance between two points, because the medium is considered homogeneous.

Let A_k be the E field amplitude of the k_{th} ray at the input of the ray tube, and A'_k the amplitude at the output. Following this notation, the amplitude associated with a given ray-tracing is given by A.4 and rewritten as:

$$A'_k = A_k \sqrt{\frac{dL_k}{dL'_k}} \qquad \text{(A.6)}$$

The distance dL'_k can be estimated as the projection of the infinitesimal arc length ds_k on the aperture

$$dL'_k = ds_k \cos\theta_k, \qquad \text{(A.7)}$$

where θ_k is the angle between the normalized Poynting vector $\widehat{s_k}$ of the ray and the normal vector of the aperture $\widehat{n_k}$ in the dipole. In this case, the angle $\theta_k = 0°$ because the wave is propagating in a same medium without any variations (free space) and the ray follows a straight-line trajectory ($dL'_k = ds_k$), see Fig. A.2(a).
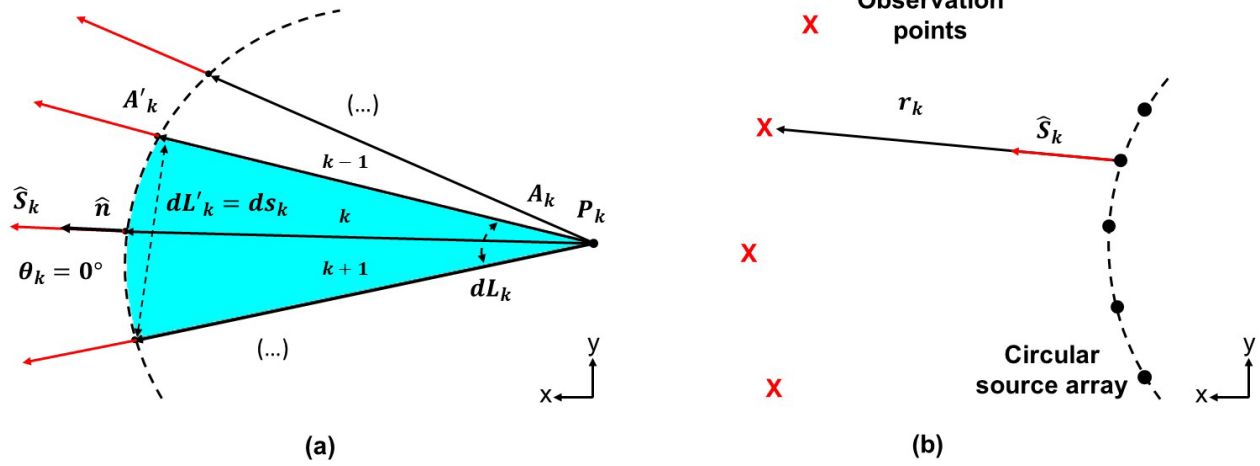
Fig. A.2 (a) Schematic of the ray-tracing model. The two neighboring rays ($k − 1$) and ($k + 1$) form the ray tube of the k_{th} ray in a bi-dimensional system. (b) Circular source array model for calculating the far-field radiation pattern. The red crosses are the observation points.

To calculate the radiation pattern the contribution of each secondary source is considered. According to Huygens' principle every point of the wavefront becomes a source of wavelets that radiate in the direction of the Poynting vector [147]. An arbitrary number of observation points are placed to calculate the radiation pattern. These points need to be far enough to keep the far-field conditions, see Fig. A.2(b). The distance between the k_{th} radiating dipole to the observation points (red crosses) is r_k. The total E field in the far-field region can be calculated by assuming that the wavelet sources are an array of antennas:

$$E(\theta) \propto \sum_k E_k(\theta) A'_k \frac{e^{jk_0(r_k+\sigma_k)}}{r_k} [\widehat{n_k} \cdot \widehat{s_k} + \widehat{n_k} \cdot \widehat{r_k}] ds_k \tag{A.8}.$$

A.2.2 Radiation pattern calculation for a classical parabolic reflector

The explained methodology is here used to evaluate the behavior of a classical parabolic reflector to validate the behavior of this in-house code before performing the

more complex analysis developed in Chapter 4. The scenario studied is presented in Fig. A.3(a). The code is evaluated in two different situations: horn antenna is placed in the focal length, and shifted off the focal length.
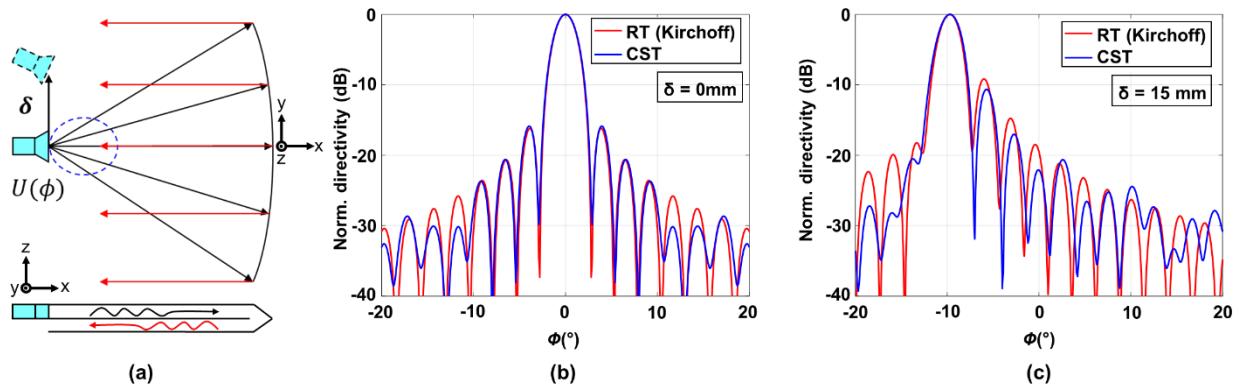
Fig. A.3 (a) Schematic of a horn feed illuminating a parabolic reflector. Comparison of ray-tracing method and CST Studio Suite® analyzing: (b) Normalized radiation patterns with *δ* = 0 mm (b) Normalized radiation patterns with *δ* = 15 mm.

Here, the geometrical optics results are compared with CST Studio Suite®. Fig. A.3(a) shows a schematic representation of the problem under consideration. It is a dual-layer parabolic reflector (to avoid the blockage effects, see Fig A.3(a) cross-sectional view) with *F/D* = 0.75, where *F* is the focal length and *D* the diameter of the reflector, illuminated by a horn antenna. The black rays represent the wave in the first layer and the red ones in the second. Fig. A.3(b) shows the results when the horn antenna is placed in the focal position *δ* = 0 mm. The agreement between the ray-tracing method and the CST Studio Suite® simulation is excellent. When the feed is shifted at *δ* = 15 mm pointing towards the parabola vertex, the radiation pattern still has a good agreement (Fig. A.3(c)) although there are more differences compared with the previous case. Anyway, a deviation in the main beam is appreciated in both cases. These results suggest that the ray-tracing can be used as an alternative to get initial results, instead of depending on time-consuming numerical simulations in all the design stages.

Appendix B

In this appendix the second part of the manufacturing process (Chapter 5) developed in the clean room of the Public University of Navarre is described.

The manufacturing process was divided in two main steps: CNC and photolithography development. First, two aluminium blocks (used to host and sandwich the metallized Si wafers with the HL and the GGW) were fabricated in aluminium and presented in section 5.5. The second step is to manufacture the GGW horn antenna and the HL using the clean room facilities. A diagram summarizing the photolithography process followed to manufacture both devices is presented in Fig. B.1.
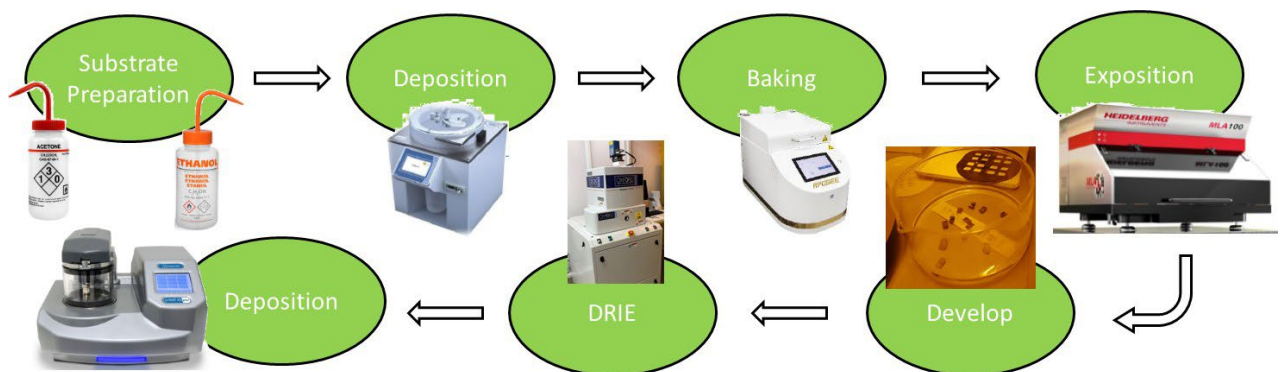
Fig. B.1 Diagram of the methodology followed in the fabrication process.

Substrate Preparation

A 110 mm diameter Si wafer is cleaned using acetone and isopropyl alcohol in the spin coater to prepare the substrate for the deposition process.

Deposition

The deposition is performed using an A10XT positive photoresist to cover the Si wafer with a thin layer around 14 µm thick (on the spin coater at 1000 rpm).

Baking and hydration

A soft bake time of 180 seconds at 110°C with direct contact hotplate is needed to improve the resist adhesion to the substrate and minimize the dark erosion of positive resist during development. Positive photoresists require a minimum water concentration of a few per thousand during exposure for the photoreaction. However, after the soft bake, water is not present in sufficient quantity in the resist film. Therefore, it must be fed back via rehydration to give the subsequently exposed areas a sufficiently high development rate. Thus, the source of water for rehydration is the atmosphere in the clean room. This depends on the humidity of the UPNA's room. Usually, 45 minutes is enough.

Exposition

The exposition process is developed by an Maskless Aligner MLA 100 machine with a dose of 1350 mJ/cm^2. A GDS file is uploaded in the MLA machine with the GGW horn antenna design in this case (see Fig. B.2(a)), where the blue zones will be etched in the Deep Reactive Ion Etching process and the white zones are protected by the photoresist A10XT. This design is exposed over the Si wafer (after the rehydration process) using the MLA exposure technique for 3 hours.

Develop

After that, a develop process using AZ 400K in a concentration 1:4 (1 of AZ 400K to 4 water portion) for 6 minutes is needed to achieve a 4 × 4 GGW horn antenna impression, see Fig. 5B.2(b).
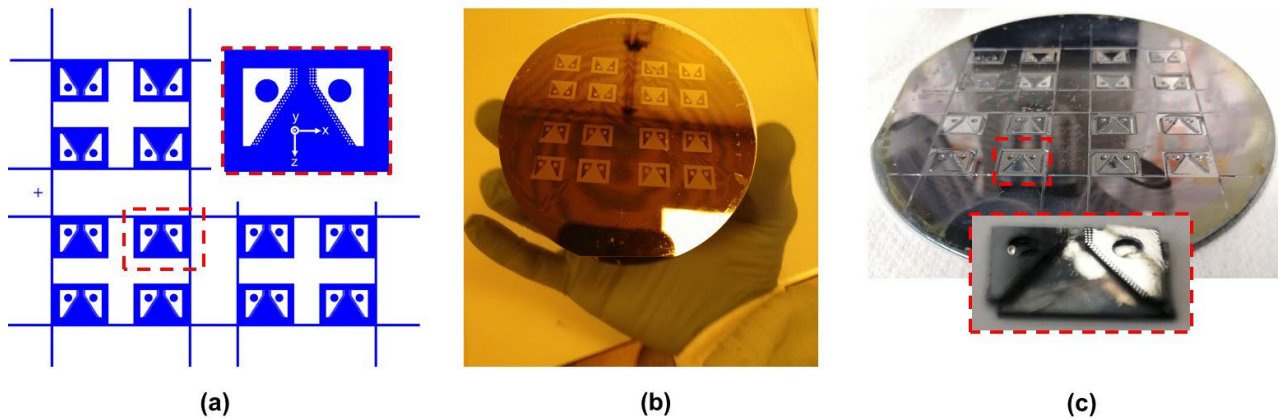
Fig. B.2 (a) GDS file of 4 × 4 GGW horn antennas. (b) Photograph of a Si wafer after develop process, where the dark zones have photoresist that protect the silicon of the etch process. (c) Photograph of a Si wafer etched, the red dashed square is a single piece in the end of the etch process.

Deep Reactive Ion Etching (DRIE)

The etching is performed with the Deep Reactive Ion Etching procedure employing the Oxford Instruments Plasma Pro NGP80 ICP65. This is a complex process where the material is exposed to a plasma of certain gases (typically for etching of Si are chlorinated and fluorinated carbon) in a high vacuum environment. The etching is achieved because a chemically reactive radical is formed in the plasma and accelerated towards the substrate (physical bombardment). Therefore, different materials can be etched depending on the combination of gases, RF and ICP powers, and temperature. As shown in Fig. B.2(b), the photoresist protects the zones that should not be etched with a selectivity of 30 µm per 1 µm of photoresist. Therefore, in the deposition step, the Si wafer was covered by 14 µm of photoresist, which allows 420 µm of etching, enough to achieve 300 µm of height in the GGW's antenna pins, see Fig. B.2(c).

Metallization deposition

The metallization of wafers is usually done by thermal evaporation or sputtering. Since the adhesion of many metals to silicon is comparatively poor, it is sometimes advisable to use a thin layer (10 – 20 nm) of chrome or titanium metallic adhesion layer between

the substrate and the actual metallization. In this case, the metallization deposition was done by sputter deposition, which ensures a volumetric metallization able to cover the ground and the side walls of the pins.
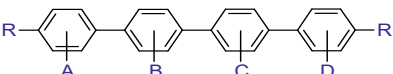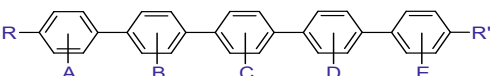
Sputter deposition is a physical vapor deposition method of thin-film deposition by the phenomenon of sputtering. Applying this method, a thin layer of 10 nm of chrome was deposited to improve the adhesion, 1 µm of cooper as the main metallic conductor, and 30 nm of gold to avoid oxidation finalizing the sputtering metallization process.

Appendix C

C.1 Developed Liquid Crystal Composition

Among the most promising classes of LC compounds for high-frequency applications nematic LC compositions based on polycyclic LC substances stand out, in particular, derivatives of n-quaterphenyl and n-quinquiphenyl with different terminal (R, R') and lateral (A, B, C, D, E) substituents [148]–[150]. The latter ones can be represented by the general structural formulas given in Table C.1. As compared to 2- and 3-ring substances, 4- and 5-ring LC compounds are characterized by higher optical anisotropy that makes them attractive for tunable LC-devices, while the introduction of lateral substituents into the ring molecules enables to decrease their melting point and improve miscibility.

Table C.1: Components of the developed LC composition LCM-1.

In collaboration with Institute of Applied Physical Problems of Minsk, new approaches towards the synthesis of liquid-crystalline laterally substituted polyaromatic derivatives of n-quaterphenyl and n-quinquiphenyl was developed, involving condensation methods for the formation of substituted cyclic fragments [149], [150]. These methods are distinguished by implementation, simplicity and availability of the initial reagents. The developed technology opens the possibility to synthesize new polyaromatic LC compounds with high optical anisotropy ($\Delta n \geq 0.4$, where Δn is the refractive index difference between ordinary and extraordinary axes), as well as high chemical and photochemical stability. The melting point for most of the synthesized substances does not exceed +80, +90°C (for the best n-quaterphenyl compound it is even below +65°C, being the best result ever achieved in the world) and have the temperature of transition to the isotropic state less than 210°C. Synthesized LC compounds have rod-shaped molecules and are characterized by good solubility in most organic solvents and good miscibility with all known low-viscosity classes of LC compounds.

Table C.2: Dielectric properties of LCM-1 @110 GHz

$\varepsilon'_{\perp}$	$\varepsilon'_{\parallel}$	$\Delta\varepsilon'$	$\tan\delta_{\perp}$	$\tan\delta_{\parallel}$
2.38	3.72	1.34	0.003	0.002

Based on the synthesized LC compounds, a LC composition promising for applications in tunable meta-devices both at microwaves and millimeter waves was experimentally optimized and produced. Such a composition, hereafter referred to as LCM 1, is characterized by low dielectric losses (< 0.003), high dielectric anisotropy (>1.3), and low dispersion in comparison with similar products of other developers. The experimentally measured dielectric propertied of the developed LC composition are summarized in Table C.2, wherein the values of the real part $\varepsilon_{\parallel,\perp}$ and loss tangent $\tan\delta_{\parallel,\perp}$ of the complex dielectric permittivity $\varepsilon_{\parallel,\perp} = \varepsilon'_{\parallel,\perp}\left(1 - j\tan\delta_{\parallel,\perp}\right)$ parallel and perpendicular to the vector of the high-frequency electric field, respectively, are presented.

The results of this collaboration carried out also allow to draw the following conclusions in regard to LC compounds for microwave and mmWave applications: (i) the value of the LC molecule birefringence itself is a very important parameter, however, it is not the main factor influencing on the dielectric anisotropy in the high frequency region; (ii) the main factors affecting the dielectric anisotropy strongly depend on the bulk and type of the polar groups; (iii) the bridge fragments in the LC molecules decrease the dielectric anisotropy at high frequencies.

C.2 Operation Principle of Reflectarray and its Electromagnetic Features

The electromagnetic features of a LC-based RA when the free-space wavelength λ is much larger than the LC layer thickness, h_{LC}, can be explained through a high-impedance surface (HIS concept [151]. HISs are metamaterial structures, also referred to as artificial magnetic conductors, which were originally introduced in the microwave antenna engineering as ultra-thin artificial substrates for low-profile antennas.

In a conventional design, the LC-loaded RA has a configuration of HIS and is represented by a single-layer frequency-selective surface or MTS of a capacitive type patterned on a thin dielectric slab (in our case the LC layer and hence it will be referred to as LC) with uniform back metallization ("ground plane" or GP), see Fig. C.1(a). The term "capacitive" means that the reactive part of the MTS impedance Z_{MTS} in the frequency band of HIS/RA operation satisfies the condition: Im (Z_{MTS}) < 0. The thinnest HIS is obtained when the MTS is comprised of electrically isolated (for a working polarization) subwavelength metallic elements, e.g. patches (see Fig. C.1(a)), operating at angular frequencies ω below any possible plasmonic MTS resonances: $\omega<\omega_{res}$. In the limit $\omega\rightarrow0$, the metallic elements do not support excitation of ohmic surface currents and act as an effective lumped capacitance C_{MTS}: $Z_{MTS}|_{\omega\rightarrow0} = 1/(j\omega C_{MTS})$.
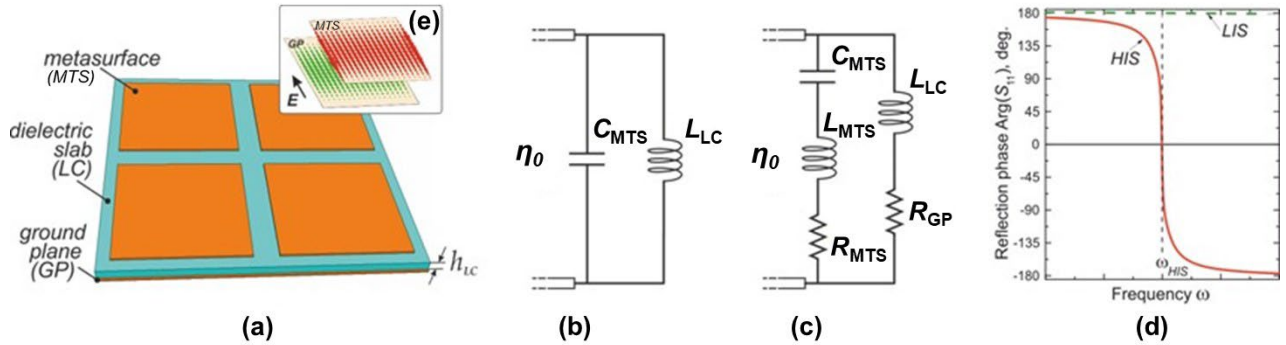
Fig. C.1 Conventional HIS configuration (a) and its simplified (b) and complete (c) equivalent circuit representation. The lumped resistance R_{MS} is introduced to consider ohmic dissipation in the MTS metallization and dielectric losses in the LC layer, while R_{GP} describes ohmic dissipation in the GP [152]. (d) Qualitative spectral behavior for the HIS reflection phase. (e) Illustration of the vector distributions of surface currents induced in the MTS and GP layers at the HIS resonance (full-wave simulations).

The possibility to realize a small electrical thickness for the HIS configuration is based on the fact that, when neglecting dissipative losses, the input impedance Z_{LC} of the "grounded" LC layer becomes purely inductive if $h_{LC}/l \ll 1$ (ultra-thin regime): $Z_{LC} \cong j\omega L_{LC}$ [151]. Herein, L_{LC} represents an effective inductance of the "grounded" layer, which is linearly proportional to its thickness h_{LC}:

$$L_{LC} = \frac{\mu h_0}{c_0}\, h_{LC}.$$

(C.1)

where μ is the relative magnetic permeability of the LC layer (at sub-THz frequencies $\mu \cong 1$), c_0 is the speed of light, η_0 is the impedance of the medium facing MTS ($\eta_0 \cong 377$ Ω for the free space). The structure can be modelled as a parallel connection of the impedances Z_{MTS} and Z_{LC} (Fig. C.1(b)), thereby forming a resonant circuit whose total impedance Z in the lossless case with a purely capacitive MTS is:

$$Z \cong \frac{j\omega L_{LC}}{1 - \omega^2 C_{MTS} L_{LC}}.$$

(C.2)

143

The HIS resonance is achieved at the angular frequency $\omega_{HIS} = 1/\sqrt{C_{MTS}L_{LC}}$ where the total impedance goes to infinity. The value of Z specifies a complex amplitude reflection coefficient S_{11} of the structure according to the well-known formula [153]:

$$S_{11} = \frac{Z - h_0}{Z + h_0}. \qquad (C.3)$$

The typical spectral behavior of the reflection phase $\text{Arg}(S_{11})$ near the HIS resonance is shown in Fig. C.1(d). It is worth highlighting that $\text{Arg}(S_{11})$ undergoes a strong variation near ω_{HIS}, at which $S_{11}=+1$ so that the phase crosses a zero-point corresponding to the characteristic of an artificial magnetic conductor. This distinguishes HISs from ordinary conductors (metals) acting as low-impedance surfaces (LISs), for which $S_{11} \cong -1$ which implies that $|\text{Arg}(S_{11})| \cong 180°$. As illustrated in the inset in Fig. 6.1(e), the strong artificial magnetic properties of the HIS-structure originate from large antiparallel surface currents flowing in the MS and GP layers at the HIS resonance. These currents are induced almost in phase and form an effective magnetic dipole with a magnetic flux concentrated mainly between the MTS and GP.

The rapid change of $\text{Arg}(S_{11})$ is crucial for the operation of the LC-loaded RA. Actually, its phase tunability is achieved by varying the dielectric permittivity of the LC layer by means of a biasing quasi-static external electric field that directly affects the LC-loaded MTS capacitance, C_{MTS}. In real RA implementation, the biasing is achieved by transforming the MTS and GP into electrodes. In case of the patch array MTS, this requires, however, introduction of inductive strips connecting the patches in one direction which are to be excited by an external electromagnetic wave with polarization orthogonal to the strips. Alternatively, it is allowed to use a MTS with "inductive" topology represented by a metal layer with slot-like resonant elements operating at frequencies where $\text{Im}(Z_{MTS}) < 0$. In this case, when the MTS inductance L_{MTS} cannot be neglected (Fig. C.1(c)), the HIS resonance for the lossless regime ($R_{MTS} = R_{GP} = 0$) is achieved at the frequency [152], [154].

$$\omega_{HIS} \cong \frac{1}{\sqrt{C_{MTS}L_{LC}}} \cdot \left(1 + \frac{L_{MTS}}{L_{LC}}\right)^{-1/2} \tag{C.4}$$

It is further clear that the narrower the fractional HIS bandwidth $\Delta\omega_{\text{HIS}}/\omega_{\text{HIS}}$, the stronger the tunability. Derived from the definition $|\text{Arg}(S_{11}[\omega_{\text{HIS}} \pm \frac{1}{2}\Delta\omega_{\text{HIS}}])| = 90°$ [152], conditioned by $\omega_{HIS}L_{LC} \ll h_0$, the bandwidth is bound to the h_{LC}/l_{HIS} ratio via a weakly non-linear law [152], [154]:

$$\frac{\Delta\omega_{\text{HIS}}}{\omega_{\text{HIS}}} = \cong \frac{1}{h_0}\sqrt{\frac{L_{LC}}{C_{MTS}}} \cdot \left(1 + \frac{L_{MTS}}{L_{LC}}\right)^{-\frac{3}{2}} = 2\pi\left(1 + \frac{c_0 L_{MTS}}{\mu h_0 h_{LC}}\right)^{-1}\frac{h_{LC}}{l_{HIS}} \tag{C.5}$$

The relation (C.5) illustrates the key feature of the HIS configuration, which is narrowing the bandwidth when thinning the structure. A supplementary conclusion arising from (C.5) is that the bandwidth can be additionally decreased by augmenting the MTS inductance LMTS (see also [154]).

Bibliography

[1] A. Borji, D. Busuioc, and S. Safavi-Naeini, "Efficient, Low-Cost Integrated Waveguide-Fed Planar Antenna Array for Ku-Band Applications," *IEEE Antennas Wirel. Propag. Lett.*, vol. 8, pp. 336–339, 2009, doi: 10.1109/LAWP.2008.2004973.

[2] D. Pozar, "Considerations for millimeter wave printed antennas," *IEEE Trans. Antennas Propag.*, vol. 31, no. 5, pp. 740–747, Sep. 1983, doi: 10.1109/TAP.1983.1143124.

[3] A. Giri, S. Dutta, S. Neogy, K. Dahal, and Z. Pervez, "Internet of things (IoT): A survey on architecture, enabling technologies, applications and challenges," *ACM Int. Conf. Proceeding Ser.*, 2017, doi: 10.1145/3109761.3109768.

[4] Y. Wang, J. Li, L. Huang, Y. Jing, A. Georgakopoulos, and P. Demestichas, "5G Mobile: Spectrum Broadening to Higher-Frequency Bands to Support High Data Rates," *IEEE Veh. Technol. Mag.*, vol. 9, no. 3, pp. 39–46, Sep. 2014, doi: 10.1109/MVT.2014.2333694.

[5] Z. Pi and F. Khan, "An introduction to millimeter-wave mobile broadband systems," *IEEE Commun. Mag.*, vol. 49, no. 6, pp. 101–107, 2011, doi: 10.1109/MCOM.2011.5783993.

[6] V. Dang, "Benefits of 5G Millimeter-wave Communication in IoT applications," no. January, 2022.

[7] G. A. Siles, J. M. Riera, and P. García-Del-Pino, "Atmospheric attenuation in

wireless communication systems at millimeter and THz frequencies [Wireless Corner]," *IEEE Antennas Propag. Mag.*, vol. 57, no. 1, pp. 48–61, 2015, doi: 10.1109/MAP.2015.2401796.

[8]   D. Lockie and D. Peck, "High-data-rate millimeter-wave radios," *IEEE Microw. Mag.*, vol. 10, no. 5, pp. 75–83, Aug. 2009, doi: 10.1109/MMM.2009.932834.

[9]   D. Liu, U. Pfeiffer, J. Grzyb, and B. Gaucher, *Advanced millimeter-wave technologies: antennas, packaging and circuits*. John Wiley & Sons, 2009.

[10]   J. A. Nanzer, *Microwave and millimeter-wave remote sensing for security applications*. Artech House, 2012.

[11]   C. Hansen, "WiGiG: Multi-gigabit wireless communications in the 60 GHz band," *IEEE Wirel. Commun.*, vol. 18, no. 6, pp. 6–7, Dec. 2011, doi: 10.1109/MWC.2011.6108325.

[12]   M. Elkashlan, T. Q. Duong, and H. H. Chen, "Millimeter-wave communications for 5G: Fundamentals: Part i [Guest Editorial]," *IEEE Commun. Mag.*, vol. 52, no. 9, pp. 52–54, 2014, doi: 10.1109/MCOM.2014.6894452.

[13]   W. Menzel and A. Moebius, "Antenna concepts for millimeter-wave automotive radar sensors," *Proc. IEEE*, vol. 100, no. 7, pp. 2372–2379, 2012, doi: 10.1109/JPROC.2012.2184729.

[14]   C. Waldschmidt, J. Hasch, and W. Menzel, "Automotive Radar — From First Efforts to Future Systems," *IEEE J. Microwaves*, vol. 1, no. 1, pp. 135–148, Jan. 2021, doi: 10.1109/JMW.2020.3033616.

[15]   P. Sun, T. Liu, X. Chen, S. Zhang, Y. Zhao, and S. Wei, "Multi-source Aggregation Transformer for Concealed Object Detection in Millimeter-wave Images," *IEEE Trans. Circuits Syst. Video Technol.*, vol. 8215, no. c, pp. 1–1, 2022, doi: 10.1109/tcsvt.2022.3161815.

[16]   P.-S. Kildal, A. U. Zaman, E. Rajo-Iglesias, E. Alfonso, and A. Valero-Nogueira,

"Design and experimental verification of ridge gap waveguide in bed of nails for parallel-plate mode suppression," *IET Microwaves, Antennas Propag.*, vol. 5, no. 3, p. 262, 2011, doi: 10.1049/iet-map.2010.0089.

[17]   P.-S. Kildal, E. Alfonso, A. Valero-Nogueira, and E. Rajo-Iglesias, "Local Metamaterial-Based Waveguides in Gaps Between Parallel Metal Plates," *IEEE Antennas Wirel. Propag. Lett.*, vol. 8, pp. 84–87, 2009, doi: 10.1109/LAWP.2008.2011147.

[18]   E. Rajo-Iglesias, M. Ferrando-Rocher, and A. U. Zaman, "Gap Waveguide Technology for Millimeter-Wave Antenna Systems," *IEEE Commun. Mag.*, vol. 56, no. 7, pp. 14–20, Jul. 2018, doi: 10.1109/MCOM.2018.1700998.

[19]   E. Pucci, A. U. Zaman, E. Rajo-Iglesias, P. S. Kildal, and A. Kishk, "Losses in ridge gap waveguide compared with rectangular waveguides and microstrip transmission lines," *EuCAP 2010 - 4th Eur. Conf. Antennas Propag.*, pp. 10–13, 2010.

[20]   E. Rajo-Iglesias and P.-S. Kildal, "Numerical studies of bandwidth of parallel-plate cut-off realised by a bed of nails, corrugations and mushroom-type electromagnetic bandgap for use in gap waveguides," *IET Microwaves, Antennas Propag.*, vol. 5, no. 3, p. 282, 2011, doi: 10.1049/iet-map.2010.0073.

[21]   A. Polemi, S. Maci, and P.-S. Kildal, "Dispersion Characteristics of a Metamaterial-Based Parallel-Plate Ridge Gap Waveguide Realized by Bed of Nails," *IEEE Trans. Antennas Propag.*, vol. 59, no. 3, pp. 904–913, Mar. 2011, doi: 10.1109/TAP.2010.2103006.

[22]   P.-S. Kildal, A. U. Zaman, E. Rajo-Iglesias, E. Alfonso, and A. Valero-Nogueira, "Design and experimental verification of ridge gap waveguide in bed of nails for parallel-plate mode suppression," *IET Microwaves, Antennas Propag.*, vol. 5, no. 3, p. 262, 2011, doi: 10.1049/iet-map.2010.0089.

[23]   A. Berenguer, V. Fusco, D. E. Zelenchuk, D. Sanchez-Escuderos, M. Baquero-Escudero, and V. E. Boria-Esbert, "Propagation Characteristics of Groove Gap

Waveguide Below and Above Cutoff," *IEEE Trans. Microw. Theory Tech.*, vol. 64, no. 1, pp. 27–36, Jan. 2016, doi: 10.1109/TMTT.2015.2504501.

[24] J. Liu, A. Vosoogh, A. U. Zaman, and J. Yang, "Design and Fabrication of a High-Gain 60-GHz Cavity-Backed Slot Antenna Array Fed by Inverted Microstrip Gap Waveguide," *IEEE Trans. Antennas Propag.*, vol. 65, no. 4, pp. 2117–2122, Apr. 2017, doi: 10.1109/TAP.2017.2670509.

[25] E. Pucci, A. U. Zaman, E. Rajo-Iglesias, P. S. Kildal, and A. Kishk, "Losses in ridge gap waveguide compared with rectangular waveguides and microstrip transmission lines," *EuCAP 2010 - 4th Eur. Conf. Antennas Propag.*, 2010.

[26] C. A. Balanis, *Antenna theory: analysis and design*. John wiley & sons, 2015.

[27] T. Manabe *et al.*, "Polarization dependence of multipath propagation and high-speed transmission characteristics of indoor millimeter-wave channel at 60 GHz," *IEEE Trans. Veh. Technol.*, vol. 44, no. 2, pp. 268–274, May 1995, doi: 10.1109/25.385918.

[28] J. Xi, B. Cao, H. Wang, and Y. Huang, "A novel 77 GHz circular polarization slot antenna using ridge gap waveguide technology," in *2015 Asia-Pacific Microwave Conference (APMC)*, Dec. 2015, pp. 1–3, doi: 10.1109/APMC.2015.7413566.

[29] T. Li and F. Fan, "Design of ka-band 2×2 circular polarization slot antenna array fed by ridge gap waveguide," in *2017 Sixth Asia-Pacific Conference on Antennas and Propagation (APCAP)*, Oct. 2017, pp. 1–3, doi: 10.1109/APCAP.2017.8420577.

[30] M. Ferrando-Rocher, J. I. Herranz-Herruzo, A. Valero-Nogueira, and A. Vila-Jimenez, "Single-Layer Circularly-Polarized Ka-Band Antenna Using Gap Waveguide Technology," *IEEE Trans. Antennas Propag.*, vol. 66, no. 8, pp. 3837–3845, Aug. 2018, doi: 10.1109/TAP.2018.2835639.

[31] J. I. Herranz-Herruzo, A. Valero-Nogueira, M. Ferrando-Rocher, and B. Bernardo-Clemente, "High-Efficiency Ka-band Circularly-Polarized Radial-Line Slot Array

Antenna on a Bed of Nails," *IEEE Trans. Antennas Propag.*, vol. 70, no. 5, pp. 3343–3353, 2021, doi: 10.1109/TAP.2021.3137376.

[32] J. I. Herranz-Herruzo, M. Ferrando-Rocher, A. Valero-Nogueira, and B. Bernardo-Clemente, "Novel Asymmetric T-Shaped Radiating Element for Circularly-Polarized Waveguide Slot Arrays," *IEEE Trans. Antennas Propag.*, vol. 69, no. 11, pp. 7452–7461, 2021, doi: 10.1109/TAP.2021.3076277.

[33] M. Ferrando-Rocher, J. I. Herranz-Herruzo, A. Valero-Nogueira, and B. Bernardo-Clemente, "Dual Circularly Polarized Aperture Array Antenna in Gap Waveguide for High-Efficiency Ka-Band Satellite Communications," *IEEE Open J. Antennas Propag.*, vol. 1, no. 1, pp. 283–289, 2020, doi: 10.1109/OJAP.2020.3001087.

[34] F. Fan and Z. Yan, "High gain circularly polarized slot antenna based on microstrip-ridge gap waveguide technology," in *2017 11th European Conference on Antennas and Propagation (EUCAP)*, Mar. 2017, pp. 1669–1672, doi: 10.23919/EuCAP.2017.7928621.

[35] E. Baghernia, R. Movahedinia, and A. R. Sebak, "Broadband Compact Circularly Polarized Spiral Antenna Array Fed by Printed Gap Waveguide for Millimeter-Wave Applications," *IEEE Access*, vol. 9, pp. 86–95, 2021, doi: 10.1109/ACCESS.2020.3046720.

[36] Z. Zang, A. U. Zaman, and J. Yang, "Single Layer Dual Circularly Polarized Antenna Array Based on Ridge Gap Waveguide for 77 GHz Automotive Radar," *IEEE Trans. Antennas Propag.*, no. c, pp. 1–1, 2022, doi: 10.1109/tap.2022.3161283.

[37] A. A. Oliner, "Leaky-Wave Antennas," in *Antenna Engineering Handbook*, R. C. Johnson, Ed. New York: Mc Graw-Hill, 1993.

[38] F. Monticone and A. Alù, "Leaky-wave theory, techniques, and applications: From microwaves to visible frequencies," *Proc. IEEE*, vol. 103, no. 5, pp. 793–821, 2015, doi: 10.1109/JPROC.2015.2399419.

[39]   W. W. Hansen, "Radiating electromagnetic waveguide," U.S. Patent No. 2 402 622, 1940.

[40]   U. Beaskoetxea Gartzia, "Leaky wave antennas, plasmonics and metamaterials in the terahertz," Sep. 2017, Accessed: Jul. 26, 2022. [Online]. Available: https://hdl.handle.net/2454/28768.

[41]   T. Tamir and A. A. Oliner, "Guided complex waves. Part 1: Fields at an interface," *Proc. Inst. Electr. Eng.*, vol. 110, no. 2, p. 310, 1963, doi: 10.1049/piee.1963.0044.

[42]   M. Beruete *et al.*, "Very low-profile 'Bull's Eye' feeder antenna," *IEEE Antennas Wirel. Propag. Lett.*, vol. 4, no. 1, pp. 365–368, 2005, doi: 10.1109/LAWP.2005.851104.

[43]   M. Guglielmi and D. R. Jackson, "Broadside radiation from periodic leaky-wave antennas," *IEEE Trans. Antennas Propag.*, vol. 41, no. 1, pp. 31–37, 1993, doi: 10.1109/8.210112.

[44]   P. Baccarelli, P. Burghignoli, G. Lovat, and S. Paulotto, "A novel printed leaky-wave 'bull-eye' antenna with suppressed surface-wave excitation," in *IEEE Antennas and Propagation Society Symposium, 2004.*, 2004, vol. 1, pp. 1078-1081 Vol.1, doi: 10.1109/APS.2004.1329861.

[45]   U. Beaskoetxea, A. E. Torres-Garcia, and M. Beruete, "Ku-Band Low-Profile Asymmetric Bull's-Eye Antenna With Reduced Sidelobes and Monopole Feeding," *IEEE Antennas Wirel. Propag. Lett.*, vol. 17, no. 3, pp. 401–404, Mar. 2018, doi: 10.1109/LAWP.2018.2791660.

[46]   U. Beaskoetxea *et al.*, "77-GHz High-Gain Bull's-Eye Antenna With Sinusoidal Profile," *IEEE Antennas Wirel. Propag. Lett.*, vol. 14, pp. 205–208, 2015, doi: 10.1109/LAWP.2014.2360215.

[47]   U. Beaskoetxea and M. Beruete, "High Aperture Efficiency Wide Corrugations Bull's-Eye Antenna Working at 60 GHz," *IEEE Trans. Antennas Propag.*, vol. 65,

no. 6, pp. 3226–3230, Jun. 2017, doi: 10.1109/TAP.2017.2696423.

[48] M. Chen, M. Kim, A. M. H. Wong, and G. V. Eleftheriades, "Huygens' metasurfaces from microwaves to optics: a review," *Nanophotonics*, vol. 7, no. 6, pp. 1207–1231, Jun. 2018, doi: 10.1515/nanoph-2017-0117.

[49] M. Bosiljevac, M. Casaletti, F. Caminita, Z. Sipus, and S. Maci, "Non-Uniform Metasurface Luneburg Lens Antenna Design," *IEEE Trans. Antennas Propag.*, vol. 60, no. 9, pp. 4065–4073, Sep. 2012, doi: 10.1109/TAP.2012.2207047.

[50] O. Zetterstrom, R. Hamarneh, and O. Quevedo-Teruel, "Experimental Validation of a Metasurface Luneburg Lens Antenna Implemented With Glide-Symmetric Substrate-Integrated Holes," *IEEE Antennas Wirel. Propag. Lett.*, vol. 20, no. 5, pp. 698–702, May 2021, doi: 10.1109/LAWP.2021.3060283.

[51] J. Li *et al.*, "Design of a Broadband Metasurface Luneburg Lens for Full-Angle Operation," *IEEE Trans. Antennas Propag.*, vol. 67, no. 4, pp. 2442–2451, Apr. 2019, doi: 10.1109/TAP.2018.2889006.

[52] J. G. Marin and J. Hesselbarth, "Lens Antenna With Planar Focal Surface for Wide-Angle Beam-Steering Application," *IEEE Trans. Antennas Propag.*, vol. 67, no. 4, pp. 2757–2762, Apr. 2019, doi: 10.1109/TAP.2019.2894336.

[53] H. Lu, Z. Liu, J. Liu, G. Wu, Y. Liu, and X. Lv, "Fully Metallic Anisotropic Lens Crossover-in-Antenna Based on Parallel Plate Waveguide Loaded With Uniform Posts," *IEEE Trans. Antennas Propag.*, vol. 68, no. 7, pp. 5061–5070, Jul. 2020, doi: 10.1109/TAP.2020.2975261.

[54] J. Liu, H. Lu, Z. Dong, Z. Liu, Y. Liu, and X. Lv, "Fully Metallic Dual-Polarized Luneburg Lens Antenna Based on Gradient Parallel Plate Waveguide Loaded With Nonuniform Nail," *IEEE Trans. Antennas Propag.*, vol. 70, no. 1, pp. 697–701, Jan. 2022, doi: 10.1109/TAP.2021.3098544.

[55] O. Quevedo-Teruel, J. Miao, M. Mattsson, A. Algaba-Brazalez, M. Johansson, and

L. Manholm, "Glide-Symmetric Fully Metallic Luneburg Lens for 5G Communications at Ka-Band," *IEEE Antennas Wirel. Propag. Lett.*, vol. 17, no. 9, pp. 1588–1592, Sep. 2018, doi: 10.1109/LAWP.2018.2856371.

[56]   J. Ruiz-Garcia, E. Martini, C. Della Giovampaola, D. Gonzalez-Ovejero, and S. Maci, "Reflecting Luneburg Lenses," *IEEE Trans. Antennas Propag.*, vol. 69, no. 7, pp. 3924–3935, Jul. 2021, doi: 10.1109/TAP.2020.3044668.

[57]   F. Fan, M. Cai, J. Zhang, Z. Yan, and J. Wu, "Wideband Low-Profile Luneburg Lens Based on a Glide-Symmetric Metasurface," *IEEE Access*, vol. 8, pp. 85698–85705, 2020, doi: 10.1109/ACCESS.2020.2992653.

[58]   H. Duan *et al.*, "All-dielectric metasurfaces for polarization manipulation: Principles and emerging applications," *Nanophotonics*, vol. 9, no. 12, pp. 3755–3780, 2020, doi: 10.1515/nanoph-2020-0220.

[59]   A. C. Overvig *et al.*, "Dielectric metasurfaces for complete and independent control of the optical amplitude and phase," *Light Sci. Appl.*, vol. 8, no. 1, 2019, doi: 10.1038/s41377-019-0201-7.

[60]   A. Moreno-Peñarrubia, J. Teniente, S. Kuznetsov, B. Orazbayev, and M. Beruete, "Ultrathin and high-efficiency Pancharatnam–Berry phase metalens for millimeter waves," *Appl. Phys. Lett.*, vol. 118, no. 22, p. 221105, May 2021, doi: 10.1063/5.0048907.

[61]   G. Thiele and R. Rudduck, "Geodesic lens antennas for low-angle radiation," *IEEE Trans. Antennas Propag.*, vol. 13, no. 4, pp. 514–521, Jul. 1965, doi: 10.1109/TAP.1965.1138483.

[62]   W. Rotman and R. Turner, "Wide-angle microwave lens for line source applications," *IEEE Trans. Antennas Propag.*, vol. 11, no. 6, pp. 623–632, Nov. 1963, doi: 10.1109/TAP.1963.1138114.

[63]   C. Pfeiffer and A. Grbic, "Planar Lens Antennas of Subwavelength Thickness:

Collimating Leaky-Waves with Metasurfaces," *IEEE Trans. Antennas Propag.*, vol. 63, no. 7, pp. 3248–3253, 2015, doi: 10.1109/TAP.2015.2422832.

[64]   A. Tellechea *et al.*, "Dual circularly polarized broadside beam antenna based on metasurfaces," *J. Phys. Conf. Ser.*, vol. 963, no. 1, pp. 2944–2953, 2018, doi: 10.1088/1742-6596/963/1/012006.

[65]   D. Perez-Quintana, C. Bilitos, J. Ruiz-Garcia, D. Gonzalez-Ovejero, and M. Beruete, "Flat Lens Antenna using Gap Waveguide Technology at Millimeter Waves," *2021 15th Int. Congr. Artif. Mater. Nov. Wave Phenomena, Metamaterials 2021*, no. September, pp. 343–346, 2021, doi: 10.1109/Metamaterials52332.2021.9577146.

[66]   M. Huang, S. Yang, F. Gao, R. Quarfoth, and D. Sievenpiper, "A 2-D multibeam half maxwell fish-eye lens antenna using high impedance surfaces," *IEEE Antennas Wirel. Propag. Lett.*, vol. 13, pp. 365–368, 2014, doi: 10.1109/LAWP.2014.2306207.

[67]   J. B. Pendry, D. Schurig, and D. R. Smith, "Controlling electromagnetic fields," *Science (80-.).*, vol. 312, no. 5781, pp. 1780–1782, 2006, doi: 10.1126/science.1125907.

[68]   D. L. Anderson, "References and notes," in *New Theory of the Earth*, vol. 312, no. June, Cambridge: Cambridge University Press, 2012, pp. 356–374.

[69]   W. Yan, M. Yan, and M. Qiu, "Necessary and sufficient conditions for reflectionless transformation media in an isotropic and homogenous background," vol. 19, no. 4, pp. 232–240, 2008, [Online]. Available: http://arxiv.org/abs/0806.3231.

[70]   H. Eskandari, A. R. Attari, and M. S. Majedi, "Reflectionless design of a nonmagnetic homogeneous optical waveguide coupler based on transformation optics," *J. Opt. Soc. Am. B*, vol. 35, no. 1, p. 54, 2018, doi: 10.1364/josab.35.000054.

154

[71]   Q. Chen, F. Giusti, G. Valerio, F. Mesa, and O. Quevedo-Teruel, "Anisotropic glide-symmetric substrate-integrated-holey metasurface for a compressed ultrawideband Luneburg lens," *Appl. Phys. Lett.*, vol. 118, no. 8, 2021, doi: 10.1063/5.0041586.

[72]   O. Quevedo-Teruel *et al.*, "Transformation optics for antennas: Why limit the bandwidth with metamaterials?," *Sci. Rep.*, vol. 3, pp. 1–5, 2013, doi: 10.1038/srep01903.

[73]   T. Driscoll *et al.*, "Performance of a three dimensional transformation-optical-flattened Lüneburg lens," *Opt. Express*, vol. 20, no. 12, p. 13262, Jun. 2012, doi: 10.1364/OE.20.013262.

[74]   J. Hunt *et al.*, "Planar, flattened Luneburg lens at infrared wavelengths," *Opt. Express*, vol. 20, no. 2, p. 1706, 2012, doi: 10.1364/oe.20.001706.

[75]   I. Aghanejad, H. Abiri, and A. Yahaghi, "Design of high-gain lens antenna by gradient-index metamaterials using transformation optics," *IEEE Trans. Antennas Propag.*, vol. 60, no. 9, pp. 4074–4081, 2012, doi: 10.1109/TAP.2012.2207051.

[76]   M. Ebrahimpouri and O. Quevedo-Teruel, "Bespoke lenses based on quasi-conformal transformation optics technique," *IEEE Trans. Antennas Propag.*, vol. 65, no. 5, pp. 2256–2264, 2017, doi: 10.1109/TAP.2017.2679494.

[77]   H. Eskandari, J. L. Albadalejo-Lijarcio, O. Zetterstrom, T. Tyc, and O. Quevedo-Teruel, "H-plane horn antenna with enhanced directivity using conformal transformation optics," *Sci. Rep.*, vol. 11, no. 1, pp. 1–9, 2021, doi: 10.1038/s41598-021-93812-6.

[78]   B. Fuchs, L. Le Coq, O. Lafond, S. Rondineau, and M. Himdi, "Design Optimization of Multishell Luneburg Lenses," *IEEE Trans. Antennas Propag.*, vol. 55, no. 2, pp. 283–289, Feb. 2007, doi: 10.1109/TAP.2006.889849.

[79]   Young-Jin Park, A. Herschlein, and W. Wiesbeck, "A photonic bandgap (PBG) structure for guiding and suppressing surface waves in millimeter-wave antennas,"

IEEE Trans. Microw. Theory Tech., vol. 49, no. 10, pp. 1854–1859, 2001, doi: 10.1109/22.954798.

[80]   F. Gaufillet and E. Akmansoy, "Graded photonic crystals for luneburg lens," *IEEE Photonics J.*, vol. 8, no. 1, pp. 1–11, 2016, doi: 10.1109/JPHOT.2016.2521261.

[81]   E. L. Holzman, "A highly compact 60-GHz lens-corrected conical horn antenna," *IEEE Antennas Wirel. Propag. Lett.*, vol. 3, no. 1, pp. 280–282, 2004, doi: 10.1109/LAWP.2004.831082.

[82]   P. Kadera, T. Mikulasek, J. Hruska, and J. Lacik, "Hyperbolic lens horn antenna for fixed-beam e-band communication," *Proc. 2020 30th Int. Conf. Radioelektronika, RADIOELEKTRONIKA 2020*, pp. 1–5, 2020, doi: 10.1109/RADIOELEKTRONIKA49387.2020.9092359.

[83]   B. Zhang *et al.*, "Dielectric and metallic jointly 3D-printed mmWave hyperbolic lens antenna," *IET Microwaves, Antennas Propag.*, vol. 13, no. 11, pp. 1934–1939, 2019, doi: 10.1049/iet-map.2018.6151.

[84]   N. Chudpooti, N. Duangrit, P. Akkaraekthalin, I. D. Robertson, and N. Somjit, "220-320 GHz Hemispherical Lens Antennas Using Digital Light Processed Photopolymers," *IEEE Access*, vol. 7, pp. 12283–12290, 2019, doi: 10.1109/ACCESS.2019.2893230.

[85]   J. Ala-Laurinaho, A. Karttunen, and A. V. Räisänen, "A mm-wave integrated lens antenna for E-band beam steering," *2015 9th Eur. Conf. Antennas Propagation, EuCAP 2015*, pp. 1–2, 2015.

[86]   A. Gonzalez, K. Kaneko, T. Kojima, S. ichiro Asayama, and Y. Uzawa, "Terahertz Corrugated Horns (1.25-- 1.57 THz): Design, Gaussian Modeling, and Measurements," *IEEE Trans. Terahertz Sci. Technol.*, vol. 7, no. 1, pp. 1–11, 2016, doi: 10.1109/TTHZ.2016.2634860.

[87]   R. K. Luneburg, *Mathematical Theory of Optics*. University of California Press,

1964.

[88] R. F. Rinehart, "A Solution of the Problem of Rapid Scanning for Radar Antennae," *J. Appl. Phys.*, vol. 19, no. 9, pp. 860–862, Sep. 1948, doi: 10.1063/1.1698221.

[89] R. C. Mitchell-Thomas, O. Quevedo-Teruel, T. M. McManus, S. A. R. Horsley, and Y. Hao, "Lenses on curved surfaces," *Opt. Lett.*, vol. 39, no. 12, p. 3551, Jun. 2014, doi: 10.1364/OL.39.003551.

[90] J. Sochacki, "Gradient-index Geodesic Lenses for Integrated Optics: A Uniform Theory," *J. Mod. Opt.*, vol. 35, no. 6, pp. 891–906, Jun. 1988, doi: 10.1080/09500348814551031.

[91] M. Šarbort and T. Tyc, "Spherical media and geodesic lenses in geometrical optics," *J. Opt.*, vol. 14, no. 7, p. 075705, Jul. 2012, doi: 10.1088/2040-8978/14/7/075705.

[92] R. F. Rinehart, "A family of designs for rapid scanning radar antennas," *Proc. IRE*, vol. 40, no. 6, pp. 686–688, 1952, doi: 10.1109/JRPROC.1952.274061.

[93] K. S. Kunz, "Propagation of Microwaves between a Parallel Pair of Doubly Curved Conducting Surfaces," *J. Appl. Phys.*, vol. 25, no. 5, pp. 642–653, May 1954, doi: 10.1063/1.1721704.

[94] N. J. G. Fonseca, Q. Liao, and O. Quevedo-Teruel, "Equivalent Planar Lens Ray-Tracing Model to Design Modulated Geodesic Lenses Using Non-Euclidean Transformation Optics," *IEEE Trans. Antennas Propag.*, vol. 68, no. 5, pp. 3410–3422, 2020, doi: 10.1109/TAP.2020.2963948.

[95] N. J. G. Fonseca and O. Quevedo-Teruel, "The Water Drop Lens: A Low-Profile Geodesic Parallel Plate Waveguide Lens Antenna for Space Applications," *13th Eur. Conf. Antennas Propagation, EuCAP 2019*, no. EuCAP, 2019.

[96] Q. Liao, N. J. G. Fonseca, and O. Quevedo-Teruel, "Compact Multibeam Fully Metallic Geodesic Luneburg Lens Antenna Based on Non-Euclidean Transformation Optics," *IEEE Trans. Antennas Propag.*, vol. 66, no. 12, pp. 7383–

7388, Dec. 2018, doi: 10.1109/TAP.2018.2872766.

[97]   N. J. G. Fonseca, Q. Liao, and O. Quevedo-Teruel, "Compact parallel-plate waveguide half-Luneburg geodesic lens in the Ka-band," *IET Microwaves, Antennas Propag.*, vol. 15, no. 2, pp. 123–130, Feb. 2021, doi: 10.1049/mia2.12028.

[98]   O. Orgeira, G. Leon, N. J. G. Fonseca, P. Mongelos, and O. Quevedo-Teruel, "Near-Field Focusing Multibeam Geodesic Lens Antenna for Stable Aggregate Gain in Far-Field," *IEEE Trans. Antennas Propag.*, vol. 70, no. 5, pp. 3320–3328, 2022, doi: 10.1109/TAP.2021.3139093.

[99]   Y. Sun, F. Dang, C. Yuan, J. He, Q. Zhang, and X. Zhao, "A beam-steerable lens antenna for Ku-band high-power microwave applications," *IEEE Trans. Antennas Propag.*, vol. 68, no. 11, pp. 7580–7583, 2020, doi: 10.1109/TAP.2020.2979282.

[100] T. K. Pham, L. Guang, D. González-Ovejero, and R. Sauleau, "Dual-Band Transmitarray with Low Scan Loss for Satcom Applications," *IEEE Trans. Antennas Propag.*, vol. 69, no. 3, pp. 1775–1780, 2021, doi: 10.1109/TAP.2020.3031410.

[101] T. Strober, S. Tubau, E. Girard, H. Legay, G. Goussetis, and M. Ettorre, "Shaped Parallel-Plate Lens for Mechanical Wide-Angle Beam Steering," *IEEE Trans. Antennas Propag.*, vol. 69, no. 12, pp. 8158–8169, Dec. 2021, doi: 10.1109/TAP.2021.3090789.

[102] Chih-Chieh Cheng and A. Abbaspour-Tamijani, "Evaluation of a Novel Topology for MEMS Programmable Reflectarray Antennas," *IEEE Trans. Microw. Theory Tech.*, vol. 57, no. 12, pp. 3333–3344, Dec. 2009, doi: 10.1109/TMTT.2009.2034420.

[103] O. Bayraktar, O. A. Civi, and T. Akin, "Beam switching reflectarray monolithically integrated with RF MEMS switches," *IEEE Trans. Antennas Propag.*, vol. 60, no. 2 PART 2, pp. 854–862, 2012, doi: 10.1109/TAP.2011.2173099.

[104] H. Zhang, X. Chen, Z. Wang, Y. Ge, and J. Pu, "A 1-Bit Electronically

Reconfigurable Reflectarray Antenna in X Band," *IEEE Access*, vol. 7, pp. 66567–66575, 2019, doi: 10.1109/ACCESS.2019.2918231.

[105] Z. Wang *et al.*, "1 Bit Electronically Reconfigurable Folded Reflectarray Antenna Based on p-i-n Diodes for Wide-Angle Beam-Scanning Applications," *IEEE Trans. Antennas Propag.*, vol. 68, no. 9, pp. 6806–6810, Sep. 2020, doi: 10.1109/TAP.2020.2975265.

[106] G. Perez-Palomino, J. A. Encinar, M. Barba, and E. Carrasco, "Design and evaluation of multi-resonant unit cells based on liquid crystals for reconfigurable reflectarrays," *IET Microwaves, Antennas Propag.*, vol. 6, no. 3, p. 348, 2012, doi: 10.1049/iet-map.2011.0234.

[107] X. Meng, M. Nekovee, and D. Wu, "Reconfigurable liquid crystal reflectarray metasurface for THz communications," *IET Conf. Publ.*, vol. 2019, no. CP762, 2019, doi: 10.1049/cp.2019.0733.

[108] E. Martini *et al.*, "Reconfigurable antenna based on liquid crystals for continuous beam scanning with a single control," *2019 IEEE Int. Symp. Antennas Propag. Usn. Radio Sci. Meet. APSURSI 2019 - Proc.*, no. 4000114502, pp. 449–450, 2019, doi: 10.1109/APUSNCURSINRSM.2019.8889044.

[109] R. Stevenson, M. Sazegar, A. Bily, M. Johnson, and N. Kundtz, "Metamaterial surface antenna technology: Commercialization through diffractive metamaterials and liquid crystal display manufacturing," *2016 10th Int. Congr. Adv. Electromagn. Mater. Microwaves Opt. METAMATERIALS 2016*, no. September, pp. 349–351, 2016, doi: 10.1109/MetaMaterials.2016.7746395.

[110] S. C. Pavone, E. Martini, F. Caminita, M. Albani, and S. Maci, "Surface Wave Dispersion for a Tunable Grounded Liquid Crystal Substrate Without and With Metasurface on Top," *IEEE Trans. Antennas Propag.*, vol. 65, no. 7, pp. 3540–3548, Jul. 2017, doi: 10.1109/TAP.2017.2700015.

[111] K. Lu, "Spatial Phase Modulator," *Opt. Eng.*, vol. 29, no. 3, pp. 240–246, 1990.

[112] M. Sharma, N. Hendler, and T. Ellenbogen, "Electrically Switchable Color Tags Based on Active Liquid-Crystal Plasmonic Metasurface Platform," *Adv. Opt. Mater.*, vol. 8, no. 7, p. 1901182, Apr. 2020, doi: 10.1002/adom.201901182.

[113] M. Y. Ismail and A. F. M. Zain, "Phase tunability of reflectarray patch elements using tunable dielectric substrate of nematic liquid crystal," in *2009 IEEE International Workshop on Antenna Technology*, Mar. 2009, no. 1, pp. 1–4, doi: 10.1109/IWAT.2009.4906880.

[114] W. Hu *et al.*, "Liquid-crystal-based reflectarray antenna with electronically switchable monopulse patterns," *Electron. Lett.*, vol. 43, no. 14, p. 744, 2007, doi: 10.1049/el:20071098.

[115] G. Perez-Palomino *et al.*, "Design and Experimental Validation of Liquid Crystal-Based Reconfigurable Reflectarray Elements With Improved Bandwidth in F-Band," *IEEE Trans. Antennas Propag.*, vol. 61, no. 4, pp. 1704–1713, Apr. 2013, doi: 10.1109/TAP.2013.2242833.

[116] W. Hu *et al.*, "Design and Measurement of Reconfigurable Millimeter Wave Reflectarray Cells With Nematic Liquid Crystal," *IEEE Trans. Antennas Propag.*, vol. 56, no. 10, pp. 3112–3117, Oct. 2008, doi: 10.1109/TAP.2008.929460.

[117] W. Rotman, "Wide-angle scanning with microwave double-layer pillboxes," *IRE Trans. Antennas Propag.*, vol. 6, no. 1, pp. 96–105, Jan. 1958, doi: 10.1109/TAP.1958.1144548.

[118] M. Ettorre, R. Sauleau, and L. Le Coq, "Multi-Beam Multi-Layer Leaky-Wave SIW Pillbox Antenna for Millimeter-Wave Applications," *IEEE Trans. Antennas Propag.*, vol. 59, no. 4, pp. 1093–1100, Apr. 2011, doi: 10.1109/TAP.2011.2109695.

[119] P.-S. Kildal, "Artificially soft and hard surfaces in electromagnetics," *IEEE Trans. Antennas Propag.*, vol. 38, no. 10, pp. 1537–1544, 1990, doi: 10.1109/8.59765.

[120] H. C. Moy-Li, D. Sanchez-Escuderos, E. Antonino-Daviu, and M. Ferrando-Bataller,

"Low-Profile Radially Corrugated Horn Antenna," *IEEE Antennas Wirel. Propag. Lett.*, vol. 16, pp. 3180–3183, 2017, doi: 10.1109/LAWP.2017.2767182.

[121] M. R. Naeini and D. Van Der Weide, "3D-printed High-Directivity H-plane Horn Antenna with High Front-To-back Ratio Using Soft and Hard Walls," *IEEE Radio Wirel. Symp. RWS*, vol. 2021-Janua, no. 1, pp. 1–3, 2021, doi: 10.1109/RWS50353.2021.9360394.

[122] J. Hirokawa and M. Zhang, *Handbook of Antenna Technologies*. Singapore: Springer Singapore, 2014.

[123] A. Torres-Garcia, F. Marante, A. Tazon, J. Vassal'lo, J. Teniente, and M. Beruete, "Broadband circular polarized field generation in single layer microstrip patch antennas," in *2016 10th European Conference on Antennas and Propagation (EuCAP)*, Apr. 2016, pp. 1–4, doi: 10.1109/EuCAP.2016.7481915.

[124] A. U. Zaman and P. Kildal, "Wide-Band Slot Antenna Arrays With Single-Layer Corporate-Feed Network in Ridge Gap Waveguide Technology," *IEEE Trans. Antennas Propag.*, vol. 62, no. 6, pp. 2992–3001, 2014.

[125] M. Ferrando-Rocher, A. Valero-Nogueira, J. I. Herranz-Herruzo, and J. Teniente, "60 GHz Single-Layer Slot-Array Antenna Fed by Groove Gap Waveguide," *IEEE Antennas Wirel. Propag. Lett.*, vol. 18, no. 5, pp. 846–850, May 2019, doi: 10.1109/LAWP.2019.2903475.

[126] G. A. Hurd, "IEEE Standard Test Procedures for Antennas," *Electron. Power*, vol. 26, no. 9, p. 749, 1980, doi: 10.1049/ep.1980.0385.

[127] Bee Yen Toh, R. Cahill, and V. F. Fusco, "Understanding and measuring circular polarization," *IEEE Trans. Educ.*, vol. 46, no. 3, pp. 313–318, Aug. 2003, doi: 10.1109/TE.2003.813519.

[128] M. Beruete, U. Beaskoetxea, and T. Akalin, "Flat Corrugated and Bull's-Eye Antennas," in *Aperture Antennas for Millimeter and Sub-Millimeter Wave*

Applications. Signals and Communication Technology, 1st ed., A. Boriskin and R. Sauleau, Eds. Cham, Switzerland: Springer International Publishing, 2018, pp. 111–141.

[129] D. Y. Na, K.-Y. Jung, and Y. B. Park, "Transmission Through an Annular Aperture Surrounded With Corrugations in a PEC Plane," *IEEE Antennas Wirel. Propag. Lett.*, vol. 14, pp. 179–182, 2015, doi: 10.1109/LAWP.2014.2360130.

[130] T. H. Jang, Y. H. Han, J. Kim, and C. S. Park, "60 GHz Wideband Low-Profile Circularly Polarized Patch Antenna With an Asymmetric Inset," *IEEE Antennas Wirel. Propag. Lett.*, vol. 19, no. 1, pp. 44–48, Jan. 2020, doi: 10.1109/LAWP.2019.2952405.

[131] Q. Zhu, K. B. Ng, and C. H. Chan, "Printed circularly polarized open loop antenna array for millimeter-wave applications," in *2017 IEEE International Symposium on Antennas and Propagation & USNC/URSI National Radio Science Meeting*, Jul. 2017, vol. 2017-Janua, no. 2, pp. 2561–2562, doi: 10.1109/APUSNCURSINRSM.2017.8073323.

[132] "CST STUDIO SUITE." https://www.3ds.com/products-services/simulia/products/cst-studio-suite.

[133] E. Rajo-Iglesias and P. S. Kildal, "Groove gap waveguide: A rectangular waveguide between contactless metal plates enabled by parallel-plate cut-off," *EuCAP 2010 - 4th Eur. Conf. Antennas Propag.*, 2010.

[134] "TK-RAM absorbing material to reduce scattered fields." http://www.terahertz.co.uk/index.php?option=com_content&view=article&id=145&Itemid=448 (accessed January. 8, 2022).

[135] O. Quevedo-Teruel *et al.*, "Geodesic Lens Antennas for 5G and Beyond," *IEEE Commun. Mag.*, vol. 60, no. 1, pp. 40–45, Jan. 2022, doi: 10.1109/MCOM.001.2100545.

[136] N. J. G. Fonseca, T. Tyc, and O. Quevedo–Teruel, "A solution to the complement of the generalized Luneburg lens problem," *Commun. Phys.*, vol. 4, no. 1, p. 270, Dec. 2021, doi: 10.1038/s42005-021-00774-2.

[137] Y. Lo, "On the beam deviation factor of a parabolic reflector," *IRE Trans. Antennas Propag.*, vol. 8, no. 3, pp. 347–349, May 1960, doi: 10.1109/TAP.1960.1144854.

[138] A. S. Khan, "Microwave Antennas," in *Microwave Engineering*, CRC Press, 2014, pp. 347–372.

[139] H.-J. Song and T. Nagatsuma, "Present and Future of Terahertz Communications," *IEEE Trans. Terahertz Sci. Technol.*, vol. 1, no. 1, pp. 256–263, Sep. 2011, doi: 10.1109/TTHZ.2011.2159552.

[140] R. S. Elliott, *Antenna Theory & Design*. IEEE, 2003.

[141] J. A. Encinar, M. Arrebola, L. F. De La Fuente, and G. Toso, "A transmit-receive reflectarray antenna for direct broadcast satellite applications," *IEEE Trans. Antennas Propag.*, vol. 59, no. 9, pp. 3255–3264, 2011, doi: 10.1109/TAP.2011.2161449.

[142] N. Koide, *The Liquid Crystal Display Story*. Tokyo: Springer Japan, 2014.

[143] ZEBRA® Elastomeric Connectors, "https://www.fujipoly.com/usa/products/zebra-elastomeric-connectors/." .

[144] Q. Liao, *Fully metallic antennas for millimeter wave applications Fully metallic antennas for millimeter wave applications*. .

[145] U. Leonhardt and T. G. Philbin, "Chapter 2 Transformation Optics and the Geometry of Light," in *Progress in Optics*, vol. 53, no. 08, Elsevier B.V., 2009, pp. 69–152.

[146] F. Doucet, N. J. G. Fonseca, E. Girard, H. Legay, and R. Sauleau, "Analytical Model and Study of Continuous Parallel Plate Waveguide Lens-like Multiple-Beam

Antennas," *IEEE Trans. Antennas Propag.*, vol. 66, no. 9, pp. 4426–4436, Sep. 2018, doi: 10.1109/TAP.2018.2846768.

[147] D. A. B. Miller, "Huygens's wave propagation principle corrected," *Opt. Lett.*, vol. 16, no. 18, p. 1370, Sep. 1991, doi: 10.1364/OL.16.001370.

[148] V. Lapanik, G. Sasnouski, S. Timofeev, E. Shepeleva, G. Evtyushkin, and W. Haase, "New highly anisotropic liquid crystal materials for high-frequency applications," *Liq. Cryst.*, vol. 45, no. 8, pp. 1242–1249, Jun. 2018, doi: 10.1080/02678292.2018.1427810.

[149] G. Sasnouski, V. Lapanik, V. Bezborodov, R. Dabrowski, and J. Dziaduszek, "Synthesis of fluoro substituted quaterphenyl liquid crystals," *Phase Transitions*, vol. 87, no. 8, pp. 783–789, Aug. 2014, doi: 10.1080/01411594.2014.893341.

[150] G. Sasnouski, V. Lapanik, R. Dabrowski, and J. Dziaduszek, "Synthesis of new LC compounds with high optical anisotropy: pentaphenyl derivatives lateral substituted," *Phase Transitions*, vol. 85, no. 4, pp. 309–313, Apr. 2012, doi: 10.1080/01411594.2011.646267.

[151] N. Engheta and R. W. Ziolkowski, *Metamaterials: physics and engineering explorations*. John Wiley & Sons, 2006.

[152] S. A. Kuznetsov, A. G. Paulish, M. Navarro-Cía, and A. V. Arzhannikov, "Selective Pyroelectric Detection of Millimetre Waves Using Ultra-Thin Metasurface Absorbers," *Sci. Rep.*, vol. 6, no. 1, p. 21079, Feb. 2016, doi: 10.1038/srep21079.

[153] D. M. Pozar, *Microwave engineering*. John wiley & sons, 2011.

[154] F. Costa, S. Genovesi, and A. Monorchio, "On the bandwidth of high-impedance frequency selective surfaces," *IEEE Antennas Wirel. Propag. Lett.*, vol. 8, pp. 1341–1344, 2009, doi: 10.1109/LAWP.2009.2038346.

Author's Merits

Journal Papers

1. <u>D. Pérez-Quintana</u>, Christos Bilitos, J. Ruiz-García, D. Gonzalez-Ovejero, M. Beruete, "Fully Metallic Luneburg Metalens Antenna in Gap Waveguide Technology at V-Band," IEEE Trans. Antennas Propag. *Submitted.*

2. <u>D. Pérez-Quintana</u>, E. Aguirre, E. Olariaga, S. A. Kuznetsov, V. Lapanik, V. S. Sutormin, V. Ya. Zyryanov, J. A. Marcotegui and M. Beruete, "Reconfigurable THz Liquid Crystal meta-reflectarray". *In preparation.*

3. <u>D. Perez-Quintana</u>, I. Ederra, and M. Beruete, "Bull's-Eye Antenna with Circular Polarization at Millimeter Waves Based on Ridge Gap Waveguide Technology," IEEE Trans. Antennas Propag., vol. 69, no. 4, pp. 2376–2379, Apr. 2021, doi: 10.1109/TAP.2020.3019565.

4. <u>D. Perez-Quintana</u>, A. E. Torres-Garcia, I. Ederra, and M. Beruete, "Compact Groove Diamond Antenna in Gap Waveguide Technology with Broadband Circular Polarization at Millimeter Waves," IEEE Trans. Antennas Propag., vol. 68, no. 8, pp. 5778–5783, Aug. 2020, doi: 10.1109/TAP.2020.2996364.

International Conferences

1. <u>D. Pérez-Quintana</u>, C. Biurrun-Quel, D. Gonzalez-Ovejero, M. Beruete, "Flat Hyperbolic Lens antenna in Gap Waveguide at 300 GHz," presented at 16 International Congress on Artificial Materials for Novel Wave Phenomena (Metamaterials 2022), Siena, Italy, Sep 12-17, 2022.

2. <u>D. Pérez-Quintana</u>, Q. Chen, M. Beruete, O. Quevedo-Teruel, "Compact Pillbox Reflector Based on Geodesic Lens," presented at 16 International Congress on Artificial Materials for Novel Wave Phenomena (Metamaterials 2022), Siena, Italy, Sep 12-17, 2022.

3. <u>D. Pérez-Quintana</u>, C. Biurrun-Quel, D. Gonzalez-Ovejero, M. Beruete, "Hyperbolic Lens Antenna in Groove Gap Waveguide Technology at Sub-millimeter Waves," presented at 47th International Conference on Infrared, Millimeter and Terahertz Wave (IRMMW-THz 2022), Delft, The Netherlands, Aug 28-2, 2022.

4. <u>D. Perez-Quintana</u>, I. Ederra, and M. Beruete, "Circular Polarization Antennas in Ridge Gap Waveguide at V-Band," presented at The 12th International Conference on Metamaterials, Photonic Crystal and Plasmonics (META 2022), Torremolinos, Spain, Jul 19-22, 2022.

5. <u>D. Pérez-Quintana</u>, Christos Bilitos, J. Ruiz-García, D. Gonzalez-Ovejero, M. Beruete, "Luneburg lens antenna system in Gap Waveguide technology at 60 GHz," presented at The 12th International Conference on Metamaterials, Photonic Crystal and Plasmonics (META 2022), Torremolinos, Spain, Jul 19-22, 2022.

6. <u>D. Perez-Quintana</u>, I. Ederra, and M. Beruete, "Circular Polarization Antennas in Ridge Gap Waveguide at V-Band," presented at 3rd URSI Atlantic Radio Science Meeting (AT-AP-RASC 2022) (**Young Scientist Award**), Gran Canaria, Spain, May 29-3, 2022.

7. <u>D. Pérez-Quintana</u>, Christos Bilitos, J. Ruiz-García, D. Gonzalez-Ovejero, M. Beruete, "Gap Waveguide Flat Luneburg lens antenna at millimeter waves,"

presented at 3rd URSI Atlantic Radio Science Meeting (AT-AP-RASC 2022) Gran Canaria, Spain, May 29-3, 2022.

8. D. Pérez-Quintana, Christos Bilitos, J. Ruiz-García, D. Gonzalez-Ovejero, M. Beruete, "Flat Luneburg Lens Antenna System in Gap Waveguide Technology at V-Band" presented at 16th European Conference on Antennas and Propagation (EuCAP 2022), Madrid, Spain, Mar 27-01, 2022.

9. D. Pérez-Quintana, Christos Bilitos, J. Ruiz-García, D. Gonzalez-Ovejero, M. Beruete, "Flat lens antenna using gap waveguide technology at millimeter waves," presented at 15 International Congress on Artificial Materials for Novel Wave Phenomena (Metamaterials 2021), New York, USA, Sep 20-25, 2021, virtual.

10. D. Perez-Quintana, I. Ederra, and M. Beruete, "Compact Antennas in Ridge Gap Waveguide with Circular Polarization at 60 GHz," presented at XXXIV General Assembly and Scientific Symposium of the International Union of Radio Science (URSI GASS 2021), Rome, Italy, Aug 28-4, 2021 /virtual.

11. D. Perez-Quintana, I. Ederra, and M. Beruete, "Compact Bull's-Eye Antenna in Ridge Gap Waveguide with Circular Polarization at 60 GHz" presented at 15th European Conference on Antennas and Propagation (EuCAP 2021), Virtual Conference, Mar 22-26, 2021 /virtual.

12. D. Perez-Quintana, I. Ederra, and M. Beruete, "Compact Antennas in Ridge Gap Waveguide with Circular Polarization" presented at 14 International Congress on Artificial Materials for Novel Wave Phenomena (Metamaterials 2020), New York, USA, Sep 28-3, 2020, /virtual.

13. S. Freer, R. Martínez, D. Pérez-Quintana, M. Beruete, S. M. Hanham, M. M. Attallah, M. Navarro-Cía. "Metal 3D Printed D-Band Waveguide to Surface Wave Transition," presented at 45th International Conference on Infrared, Millimeter and Terahertz Wave (IRMMW-THz 2020), Buffalo, New York, USA, Nov 8-13, 2020 /virtual.

14. <u>D. Perez-Quintana</u>, I. Ederra, and M. Beruete, "Compact Antennas in Ridge Gap Waveguide with Circular Polarization at 60 GHz," presented at 20th Mediterranean Microwave Symposium, Tetuan, Morocco, May, 2020 /virtual.

15. <u>D. Perez-Quintana</u>, A. Torres-Garcia, I. Ederra, and M. Beruete, "Circular Polarization Antennas using Gap Waveguide Technologies at 60 GHz," presented at V International Conference on Metamaterials and Nanophotonics METANANO 2020 (**Third Poster Award**), Tiflis, Georgia, Sep 14-18, 2020 /virtual.

16. <u>D. Perez-Quintana</u>, A. Torres-Garcia, I. Ederra, and M. Beruete, "A Gap Waveguide Fed Circular Polarization Antennas in the Millimeter Wave Range," presented at 14th European Conference on Antennas and Propagation (EuCAP 2020), Copenhagen, Denmark, Mar 15-20, 2020 /virtual.

17. <u>D. Pérez-Quintana</u>, I. Ederra and M. Beruete, "A Broadband Circular Polarization Diamond Slot Antenna," presented at Antennas and Propagation Conference 2019 (APC-2019), Birmingham, UK, Nov 11-12, 2019.

National Conference

1. <u>D. Pérez-Quintana</u>, C. Biurrun-Quel, D. Gonzalez-Ovejero, M. Beruete, "Hyperbolic Lens Antenna in Groove Gap Waveguide Technology at Sub-millimeter waves". XXXVII Simposio Nacional de la URSI, URSI 2022, Málaga.

2. <u>D. Pérez-Quintana</u>, Christos Bilitos, J. Ruiz-García, D. Gonzalez-Ovejero, M. Beruete, "Fully Metallic Luneburg Lens Antenna in Gap Waveguide Technology at 60 GHz". XXXVII Simposio Nacional de la URSI, URSI 2022, Málaga.

3. <u>D. Pérez-Quintana</u>, Christos Bilitos, J. Ruiz-García, D. Gonzalez-Ovejero, M. Beruete, "Flat Metasurface Antenna using Gap Waveguide Technology at 60 GHz". XXXVI Simposio Nacional de la URSI, URSI 2021, Vigo / Virtual.

4. <u>D. Pérez-Quintana</u>, I. Ederra and M. Beruete, "Circular Polarization Antennas using Gap Waveguide Technologies at millimeter waves". XXXV Simposio Nacional de la URSI, URSI 2020, Málaga (online).

5. <u>D. Pérez-Quintana</u>, I. Ederra and M. Beruete, "Broadband Circular Polarization "Diamond" Antenna implemented in Gap Waveguide Technology for 5G Millimeter-Wave Communications". XXXIV Simposio Nacional de la URSI, URSI 2019, Sevilla.

Other Merits

Courses and Doctoral Schools

1. 42 EUPROMETA Doctoral School on Future Wireless Systems enabled by Advanced and Intelligent Metasurfaces, Metamorphose Virtual Institue, March 08th -12nd 2021, Rome (online), Italy.
2. European School of Antennas and Propagation "Exploiting Symmetries in Artificial Materials for Antennas Applications" September 13rd-16th 2021, Paris, France.
3. European School of Antennas and Propagation "Metalenses for Antenna Applications" April 25th – 29th 2022, Stockholm, Sweden.

Research Stay

Research Stay in the School of Electrical Engineering and Computer Science (EECS) at KTH Royal Institute of Technology. September 1st - December 15th 2022, Stockholm, Sweden.

Session Chair

Sesión Especial: Metamateriales, metasuperficies y otras estructuras periódicas. XXXVII Simposio Nacional de la Unión de Radio, URSI 2022, Málaga.

Paper Reviewer

IET Microwaves, Antennas & Propagation
Invitation to serve as a EuCAP 2023 reviewer